ABSTRACT

Title of Dissertation: MULTISCALE ANALYSIS OF COLLECTIVE CELL MOTION

Shuyao Gu, Doctor of Philosophy, 2025

Dissertation directed by: Professor Wolfgang Losert,
Department of Physics

Collective cell migration plays an important role in a variety of biological processes such as tissue formation, wound healing, cancer progression, and immune response. However, it is still a challenge to quantitatively correlate emergent behavior to individual cell identity, genetic background and environment surrounding the cells. In this thesis, I present a multiscale analysis framework that extracts and interprets motion phenotypes from both in vitro and in vivo systems, integrating computational approaches with biological insight.

I first developed an AI-based label-free tracking method to analyze cell motion in epithelial monolayers, using phase contrast imaging. From these tracks, we calculated motion metrics such as D^2_{min}, which captures local non-affine rearrangements, and affine deformation, which reflects coordinated motion. Using these metrics to examine a panel of breast epithelial and cancer cell lines, we observed that more invasive cells exhibited greater D^2_{min} and less directional affine motion. These metrics can be used to accurately separate the nontumorigenic, tumorigenic and metastatic behaviors.

We then explored how physical cues like nano-ridged substrates affect migration. While topography enhanced speed and directionality, it had limited effect on mixing. Rather, we found that cell identity, in our case, KRas and PTEN mutations, dominates the response, overriding environmental influence and maintaining segregation despite changes in substrate.

To apply this analysis to live tissues, we performed 3D optical flow on intravital imaging data of immune cells in mouse tumors. This method captured collective myeloid motion near tumor lesions and revealed dynamic motion hotspots. We tracked these regions over time and observed that early-stage motion patterns may relate to whether lesions progress or regress, hinting at a predictive role for immune behavior.

Overall, these studies show that collective cell motion is influenced by genetic programs inside the cells and also by signals from the environment. This thesis provides a scalable and label-free method to quantifying motion behavior in systems across scales, offering tools for both basic biology and translational research.

MULTISCALE ANALYSIS OF COLLECTIVE CELL MOTION

by

Shuyao Gu

Dissertation submitted to the Faculty of the Graduate School of the
University of Maryland, College Park, in partial fulfillment
of the requirements for the degree of
Doctor of Philosophy
2025

Advisory Committee:
Professor Wolfgang Losert, Chair
Professor Arpita Upadhyaya
Dr. Roberto Weigert
Professor Maria Mukhina
Professor Kimberly Stroka

© Copyright by
Shuyao Gu
2025

Acknowledgements

First and foremost, I would like to thank my advisor, Dr. Wolfgang Losert, for his continuous support and guidance throughout my PhD. His patient mentorship, scientific creativity, and encouragement to think independently have profoundly shaped the way I approach research.

I am deeply grateful to Dr. Rachel M. Lee, who served as my mentor and role model. Her clear communication, high standards, and thoughtful feedback set an example I aspire to carry forward in my own work. She is always exceptionally prompt, goes the extra mile to help others, and brings a remarkable level of organization to everything she does.

My sincere thanks go to everyone in the Losert Lab for their collaboration and encouragement over the years. The lab's interdisciplinary spirit and openness fostered a supportive environment that made even the most challenging projects achievable. I would like to specifically thank Spandan Pathak for his consistent support and readiness to help, Hoony Kang for sharing his creative ideas and mathematical expertise, Anna Emenheiser for her leadership and responsiveness in lab activities, Sylvester J. Gates III for his biological insight and generosity with his time, Corey Herr for his computational guidance, and Kate O'Neill for her leadership and thoughtful mentorship. I also want to acknowledge the support and camaraderie of many other current and former lab members, including Matt Hourwitz, Philip Alvarez, Zac Benson, Abby Bull, Esteban Wright, Jeneh Perry, and Lin Zhao.

I am indebted to Dr. Stuart Martin and Dr. Michele Vitolo from the University of Maryland School of Medicine in Baltimore for their continuous help and support, for providing the cell lines, and for guiding me into the studies of cancer biology.

Collaborators at NIST, especially Joe Chalfoun and Chenyi Ling, generously shared their expertise in U-Net-based segmentation and provided valuable support throughout the project.

At the National Cancer Institute, I thank Dr. Roberto Weigert and members in the Weigert Lab for valuable insights into imaging and the tumor microenvironment, which contributed directly to this thesis. I am especially grateful to Dr. Roberto Weigert for his scientific insight and continued support throughout the project. I also thank Thomas Madsen, his diligence, clarity, and generosity with his time set a high standard that I strive to follow. The rest of the Weigert Lab also provided warm encouragement and practical help, for which I am deeply appreciative.

I am also thankful for the opportunity to collaborate on the elongate mineral particles project. I learned a great deal from Ann G. Wylie and Andry A. Korchevskiy, whose geology expertise brought essential perspective to understanding the cellular impact of minerals. Abby Bull and Jeneh Perry contributed significantly through their help with biological experiments and thoughtful discussions during the study.

The Fourkas Lab provided all the nano-ridged surfaces used in this study and offered generous and continuous support. Their technical skill and creativity were essential in enabling the investigation of topographical effects on cell behavior.

I've also had the pleasure of working with Kashmyr Dalang and Samuel Rosemore, whose enthusiasm and contributions helped drive several aspects of this

work forward. Kash brought thoughtful questions and a strong work ethic, while Sam's curiosity and sense of responsibility made mentoring him a meaningful experience.

My heartfelt thanks go to my family for their unwavering love, encouragement, and belief in me. Their support carried me through the ups and downs of this journey.

Lastly, I thank my thesis committee: Professor Wolfgang Losert, Professor Arpita Upadhyaya, Dr. Roberto Weigert, Professor Maria Mukhina, and Professor Kimberly Stroka. I'm grateful for their time, thoughtful questions, and guidance throughout my graduate work.

Table of Contents

Acknowledgements ii
Table of Contents v
List of Figures vii
Chapter 1: Introduction 1
1.1 Overview of Collective Behavior in Biology 1
1.2 Examples of Collective Behavior 3
1.2.1 Biological Mechanism of Cell-Cell Interactions 3
1.2.3 Immune Cell Coordination 7
1.2.4 Cancer Invasion and Tumor Microenvironment 11
1.3 Mathematical Metrics of Collective Behavior 15
1.4 The Interaction Between Cell Type and Environment in Collective Behavior 23
1.4.1 Different cell types respond differently to the same microenvironment 24
1.4.2 The same cell type behaves differently in different microenvironments 26
1.5 Thesis Outline 27
Chapter 2: Label-free cell tracking enables collective motion phenotyping in epithelial monolayers 29
2.1 Overview 29
2.2 Background 31
2.3 Analysis and Results 33
2.3.1 AI-based analysis workflow enables label-free single-cell tracking 33
2.3.2 A quantitative metric for cell rearrangements distinguishes tumorigenic and metastatic cell lines 35
2.3.3 Affine motion quantifies changes in collective behavior 39
2.3.4 Quantification of cell rearrangements by D^2_{min} is robust to tracking errors 43
2.4 Discussion 47
2.5 Materials and Methods 49
2.5.1 Cell Migration Datasheet 49
2.5.2 Image and Migration Analysis 51
2.5.3 D^2_{min} and Affine Analysis 51
2.5.4 Quantification and Statistical Analysis 54
Chapter 3: Cell Mixing and Guidance on Ridges 55
3.1 Overview 55
3.2 Background 56
3.3 Analysis and Results 58
3.3.1 Nanotopography Alters Sheet Morphology Without Changing Spatial Mixing 58
3.3.2 KP Cells Elongate on Ridges While 10A Shapes Stay Constant 63
3.3.3 Nanoridges Drive Faster and More Directed Migration 65
3.3.4 Clonal Identity Overrides Topographic Cues in Cell Mixing 68
3.4 Discussion 70
3.4.1 Nanotopography Enhances Migration but Not Mixing 70
3.4.2 Cell Rearrangement and Shape Responses Depend on Cell Type 71
3.4.3 Co-culture Modulates Individual Behavior but Not Identity 72
3.5 Materials and Methods 73

3.5.1 Surfaces with Ridges 73
3.5.2 Time-lapse Microscopy 75
3.5.3 Time-lapse Microscopy 76
3.5.4 Image Analysis and Mixing Analysis 77
3.5.5 Principal Component Analysis (PCA) 78
Chapter 4: 3D Collective dynamics of immune cells in live animals 80
4.1 Overview 80
4.2 Background 82
4.2.1 Head and Neck Cancer 82
4.2.2 3D Intravital Imaging 83
4.2.3 Importance of Myeloid Cells in Cancer 85
4.2.4 Rationale and Hypothesis 86
4.3 Analysis and Results 88
4.3.1 Overview of Imaging and Optical Flow Extraction 88
4.3.2 3D Optical Flow Captures Cell Motion in Live Tissues 93
4.3.3 Spatiotemporal Dynamics of Myeloid Cell Motion in Tumor Microenvironment 102
4.3.4 Motion Behavior May Relate to Lesion Fate 104
4.4 Discussion 108
4.5 Materials and Methods 110
4.5.1 Animal models and carcinogens 110
4.5.2 Imaging Setup and Preprocessing 111
4.5.3 3D Optical flow analysis 112
4.5.4 Quantification and Data Analysis 113
Chapter 5: Discussion and Future Directions 116
5.1 Summary of Key Findings 116
5.2 Limitation and Technical Challenges 117
5.3 Future Directions 118
Appendix A: Excitable Systems: A new perspective on the cellular impact of Elongate Mineral Particles 120
A.1 Overview 120
A.2 background 121
A.3 Results 123
A.4 Discussion 133
A.5 Materials and Methods 136
Appendix B: 3D Optical Flow Calculation 140
B.1 Temporal Smoothing 140
B.2 3D Optical Flow Formulation 140
Bibliography 142

List of Figures

Figure 1.1 Collective epithelial migration guided by electric fields during wound healing

Figure 1.2 Immune cell swarming behavior in vivo

Figure 1.3 Collective cancer invasion

Figure 1.4 Multicellular interactions in the tumor microenvironment

Figure 1.5 D^2_{min} captures the degree of collective versus individual motion

Figure 1.6 Radial distribution functions (RDFs) reveal spatial organization in mixed cell populations

Figure 1.7 Cell-type-specific migration on asymmetric sawtooth nanotopography

Figure 2.1 Graphical abstract

Figure 2.2 AI-based segmentation and tracking workflow captures collective migration behavior

Figure 2.3 Cell rearrangements distinguish tumorigenic and metastatic cell lines

Figure 2.4 The affine component of motion describes collective behavior

Figure 2.5 MDA-MB-231 cells exhibit increased overall motion

Figure 2.6 Manual assessment of tracking accuracy

Figure 2.7 D^2_{min} is robust to potential tracking errors

Figure 2.8 Examples of affine parameters

Figure 3.1 Nanoridges modulate the morphology of epithelial cell mixtures

Figure 3.2 Nanoridges has minimal impact on cell mixing

Figure 3.3 Nanoridges induce cell-type specific shape changes

Figure 3.4 Nanoridges guide collective cell motion

Figure 3.5 D^2_{min} reveals spatial variation in local cell rearrangement

Figure 4.1 Overview of the 4NQO-induced tongue carcinogenesis model

Figure 4.2 Transgenic Mouse Models and the time course of lesion development

Figure 4.3 Early-stage myeloid cell motion can be used to predict the lesion outcomes

Figure 4.4 3D optical flow captures myeloid cell dynamics

Figure 4.5 Comparison of myeloid cell motion across epithelial and subepithelial tissue layers

Figure 4.6 Detection and tracking of high-speed myeloid clusters from 3D optical flow (z-projected views)

Figure 4.7 Radial motion analysis of myeloid cell dynamics around lesions

Figure 4.8 Comparison of myeloid cell median speed in lesion-associated versus non-lesion regions across all animals

Figure 4.9 Median myeloid cell motion speed in cluster regions that led to lesions vs non-lesions

Figure A1 Macrophages and epithelial cells have different esotactic responses

Figure A2 Epithelial cells exhibit little to no response to all EMPs

Figure A3 EMPs trigger esotatic response in macrophages

Figure A4 Narrow Asbestiform EMPs dominate cytoskeletal activity in macrophages

Figure A5 Sample crocidolite segmentation

Chapter 1: Introduction

1.1 Overview of Collective Behavior in Biology

Understanding how coordinated patterns emerge in systems composed of many interacting units is a central question in physics. Emergent collective behavior, such as the alignment of spins in magnetic materials or the spontaneous flow of active matter, occurs when local interactions among constituents lead to long-range order. Such systems are usually far from thermodynamic equilibrium. They need constant input of energy, which breaks detailed balance and produces complex dynamics [1-3].

In recent years, biological systems have become an important place to study these ideas, especially at the cellular scale. Cells are active agents. They consume energy, produce forces, migrate, and talk to their neighbors. When many cells are observed together, their collective behavior shows similar features as physical active matter systems. Examples include phase separation, flocking, and dynamic pattern formation [4, 5].

In tissues, cells often move together as sheets, clusters, or streams. This type of motion is important for embryonic development [6, 7], tissue repair [8, 9], and diseases such as cancer invasion [10, 11]. Immune cells, like neutrophils and macrophages, also move collectively during inflammation, wound healing, and tumor surveillance [12-14] .

Collective motion does not require global coordination. Instead, it comes from local interactions like adhesion, mechanical contact, and chemical signals. These mechanisms allow cells align polarity, synchronize activity, and respond to their

neighbors [15-17]. Because of these local rules, tissues can show velocity alignment [18, 19], density fluctuations [20], clustering [21], and transitions between jamming and unjamming in epithelial tissues [22, 23].

From a physics perspective, cell collectives are good examples of nonequilibrium active matter. Energy is injected by each cell and lost through mechanical interactions. This makes it possible to use statistical mechanics, hydrodynamics, and continuum models to describe tissues [1, 24, 25]. Many of the tools developed in soft matter physics, such as correlation functions, fluctuation spectra, and rheological models, have been adapted to describe the mechanics and dynamics of living systems [26, 27].

To study how order appears in these collectives, researchers often use order parameters. For example, in motile monolayers, velocity alignment is used to define a polarization order parameter, like flocking models [21, 28]. Spatial correlation functions can quantify how far coordination extends across a tissue [29]. Deformation metrics such as D2min, originally developed to study amorphous solids, capture local plastic rearrangements within dense cell populations [30, 31].

New advances in microscopy, image processing, and computational modeling now make it possible to track thousands of cells in 2D and 3D. These methods allow high-throughput analysis of motion and connect physical measurements to biological function [32, 33].

In this thesis, I apply tools from physics, such as motion quantification, image-based active dynamics, and statistical analysis of coordination, to study collective behavior in several biological systems. These include epithelial monolayers, mixtures

of cells on nanostructured surfaces, and immune cells in the tumor microenvironment. Across these systems, I ask how collective behavior comes about, how the environment changes it, and how physics-based metrics can quantify it.

1.2 Examples of Collective Behavior

1.2.1 Biological Mechanism of Cell-Cell Interactions

Collective cell behaviors come from basic mechanisms of cell–cell interaction. These mechanisms combine physical, chemical, and mechanical cues. One important factor is adhesion molecules. Cadherins form adherens junctions that connect the actin cytoskeletons of neighboring cells. These junctions help keep epithelial sheets together, but they can also change dynamically during migration [34]. Integrins connect cells to the extracellular matrix through focal adhesions. They send signals in both directions and in this way control polarity, survival, and motility [35].

Aside from adhesion, cells also communicate with each other by chemical signaling. In autocrine signaling, a cell releases a signal and then responds to it itself; in paracrine signaling, the signal affects nearby cells [36, 37]. These signals often include cytokines, which are small proteins that help cells talk to each other and control growth, survival, and immune functions; a small group of cytokines are called chemokines, and their main role is to guide the movement of cells to the right place [38]. These diffusible signals give cells directional guidance. They also regulate how cells grow and divide, and they can change differentiation in both healthy tissues and in disease [38, 39].

Mechanical interactions are another important part. Cells pull on the substrate to generate traction forces, and they pass tension through junctions. Because of this, cells can line up with one another and move together as a group. The stiffness of tissue and the properties of the extracellular matrix also influence this process. Cells can sense these mechanical conditions and respond through mechanotransduction pathways [40, 41].

Adhesion, chemical signaling, and mechanical forces all work together. They build the basic foundation for collective behavior. In the next subsections, I describe how these mechanisms appear in biological contexts, such as epithelial sheet migration, immune cell coordination, and cancer invasion.

1.2.2 Epithelial Sheet Migration

Epithelial sheets are one of the most studied models of collective behavior. Epithelial cells form dense monolayers in tissues such as skin, airway, and intestine. These layers act as barriers that protect tissues, and at the same time they help regulate homeostasis. When injury happens, the cells migrate together to close the wound. During this process, they keep their cell–cell junctions and coordinate movement over space and time. This type of migration is called epithelial sheet migration. It is a good example of how local interactions between cells can add up to group-level functions [6].

Epithelial sheet migration is different from single-cell migration because tissue integrity is preserved. Cells are connected through cadherin-based junctions and send forces through their cytoskeletons and to the substrate underneath. These mechanical

and biochemical links allow cells to move in a coordinated way. At the wound edge, leader cells sense the environment and generate traction forces that are transmitted backward through the sheet [8, 9]. In this way, long-range coordination of motion is achieved without the need for global control.

Work from our collaborator Min Zhao's group showed that epithelial sheets can respond to applied electric fields, a behavior called electrotaxis. In wound healing assays in vitro, they demonstrated that electric fields give directional cues that align migration in large epithelial sheets. This means that collective motion can integrate not only mechanical but also bioelectrical signals [42, 43]. Time-lapse imaging also revealed that if the electric field direction is reversed, the migration direction of the sheet reverses as well (Figure 1.1) [42]. These results highlight how epithelial monolayers can sense and respond to physical fields across the whole sheet, supporting the idea that they function as a collective sensing system.

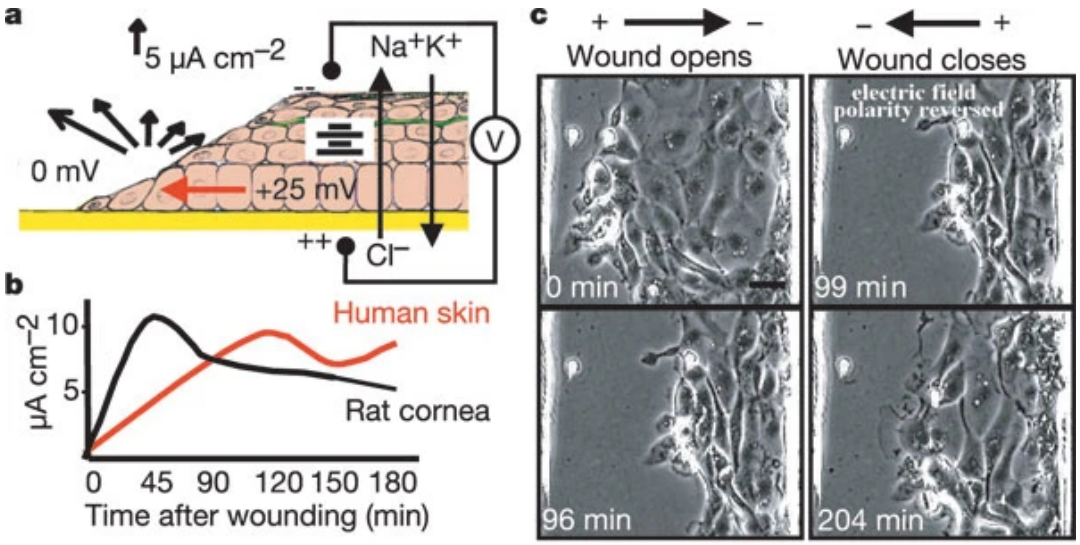


Figure 1.1. Collective epithelial migration guided by electric fields during wound healing. (a) Schematic shows that epithelial injury collapses transepithelial potential difference (V), induces lateral electric fields directed toward the wound center. (b) Measured wound currents increase over time in both rat cornea and human skin. (c) Time-lapse images of corneal epithelial cells migrating toward the cathode under a 150 mV/mm electric field show directed sheet migration; after reversing the field polarity, cells reverse direction. Adapted from Zhao et al., Nature 2006.

Aside from electric fields, epithelial collective migration is also affected by geometry, stiffness, and confinement of the substrate. For example, on micropatterned substrates, monolayers confined to narrow stripes show streaming or oscillatory flows, while on open surfaces they move as coherent fronts [17]. These physical constraints change how cells organize and interact. They show the close link between collective migration and the structure of the environment.

The motion of epithelial sheets has been quantitatively analyzed using techniques from soft matter physics and active matter theory. Measurements such as velocity correlation length, mean square displacement, and order parameters for alignment have been used to describe the extent of coordination within a migrating sheet [18, 19]. In high-density tissues, unjamming transitions can appear. In such cases, cells switch from a solid-like state to a more fluid-like one. This allows rearrangements and increases motility [22, 23].

Because epithelial cells are well-polarized, highly interactive, and easily imaged, they provide an ideal system for investigating the physical principles of collective motion. The balance between adhesion, contractility, and polarity cues governs the emergent behavior of the group. These features make epithelial monolayers a valuable model not only for understanding tissue-level functions like wound healing and morphogenesis, but also for developing and testing physics-based metrics of coordination and collective flow.

In this thesis, I draw on this foundational work to inform the analysis of more complex systems, including genetically altered epithelial collectives and cell mixtures under varying environmental conditions. By comparing baseline epithelial behavior to perturbed systems, we can better understand how coordination arises, how it is disrupted, and how it may be harnessed in pathological contexts.

1.2.3 Immune Cell Coordination

The immune system provides another rich area to study collective cell behavior. Unlike epithelial cells, immune cells usually do not stick strongly to each other. They move fast, and they are very sensitive to signals from the environment. Even though each immune cell has its own motility, many immune functions still depend on group behavior. For example, wound surveillance and tumor response both need coordinated action of many cells together. The way immune cells organize and move as collectives plays an important role in both immunity and disease progression [12, 13].

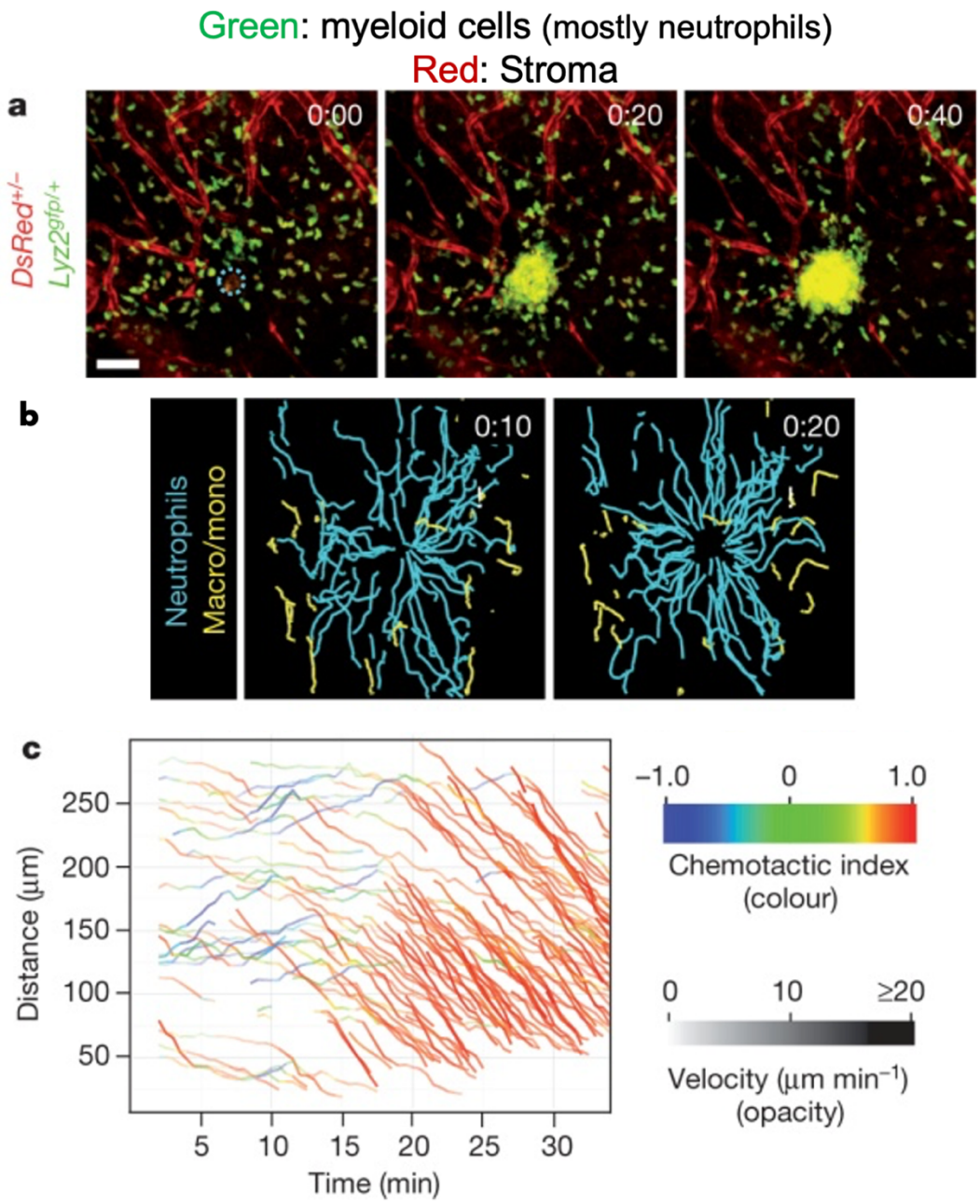


Figure 1.2: Immune cell swarming behavior in vivo. (a) Time-lapse intravital imaging in DsRed$^{+/-}$ LysM-eGFP^{+}/+ mice shows rapid neutrophil recruitment (green) toward a injury site (blue dotted circle) in the dermis. Stroma is labeled in red. Most green cells represent myeloid cells, predominantly neutrophils due to high LysM-eGFP expression. (b) Tracked trajectories of neutrophils (cyan) and

monocytes/macrophages (yellow) during swarming illustrate the more directed and centralized movement of neutrophils compared to the slower, more dispersed behavior of monocytes/macrophages. (c) Distance time plots of neutrophils migrating toward the injury site, with color representing chemotactic index (directionality) and opacity indicating velocity. Adapted from Lämmermann *et al.*, Nature 2013.

One prominent example is neutrophil swarming, where neutrophils quickly accumulate at sites of injury or infection. In response to local damage or necrotic cells, early arriving neutrophils release chemotactic signals such as leukotriene B4 that recruit additional waves of neutrophils [14, 44]. This results in a dense, multicellular cluster of neutrophils that forms dynamically and resolves once the injury is cleared. This behavior showed hallmark features of collective systems: local sensing and emergent spatial organization. Figure 1.2 illustrates this behavior in vivo, showing time-lapse imaging of neutrophil swarming, the spatial organization of multiple myeloid cell types, and quantification of chemotactic behavior during swarm formation [45]. It also enables a fast and robust response without the need for central coordination.

Other immune cells, such as dendritic cells, monocytes, and macrophages, also show forms of collective organization. For instance, in inflamed tissues, myeloid cells often align along vascular or structural tracks, moving in a coordinated manner to reach target zones. Studies using intravital microscopy have revealed that these dynamics are not random, but instead guided by both long-range gradients and local interactions with tissue structures such as collagen fibers or dying cells [12, 44].

From a physics perspective, collective immune dynamics can be seen as interacting particle systems in dynamic environments. Immune cells generate force, respond to cues, and often migrate in complex, porous tissues. Their motion can be described using active matter frameworks or agent-based models that incorporate chemotaxis, volume exclusion, and persistence [5, 46]. Quantitative measurements such as cell speed, turning angles, radial dispersion, and clustering indices can be used to characterize their spatial organization and degree of coordination over time [47, 48]. Importantly, immune coordination is not always beneficial. It can also lead to dysregulated inflammation, tissue damage, or immune evasion in disease settings. For example, overactive neutrophil swarms can cause damage in sterile inflammation, while certain tumors may exploit coordinated macrophage networks to suppress immune attack or promote angiogenesis [49]. Hence understanding immune collectives not only offers insight into host defense but also opens paths for immunotherapy and inflammation control.

In this thesis, I explore collective immune dynamics in the tumor microenvironment using high-resolution live imaging. I focus particularly on myeloid cell migration patterns in and around developing lesions, asking whether specific features of coordination, for example, localized motion and spatial asymmetry, relate to lesion progression or regression. These studies integrate motion quantification with spatial context to better understand how immune system operates.

1.2.4 Cancer Invasion and Tumor Microenvironment

Collective behavior is not only important in healthy tissues but also plays a key role in cancer. Although cancer is often thought of as uncontrolled cell growth, many tumors show organized group behaviors too, especially in invasion and metastasis. In many types of cancer, tumor cells do not move alone. Instead, they migrate together in groups, a process known as collective invasion. In this mode, cancer cells remain connected and coordinate their movement as they invade surrounding tissues [11, 50].

Collective invasion has several advantages for tumor cells. During migration, they keep their polarity and direction, which helps them move efficiently. Cells at the front of the group (called “leader cells”) often guide the direction of movement and create paths in the surrounding matrix. Cells in the back (called “followers”) help maintain cohesion and push forward. Together, these cells generate and transmit forces that help the whole group move through complex tissue structures [16, 51, 52]. Figure 1.3 shows a clinical case of collective cancer invasion, where tumor cells migrate as multicellular units while maintaining intercellular junctions and coordinated polarity [11]. Leader cells at the front generate traction forces and remodel the extracellular matrix, while follower cells maintain adhesion and transmit force throughout the group. This mode of migration enables effective tissue navigation and is commonly observed in epithelial cancers.

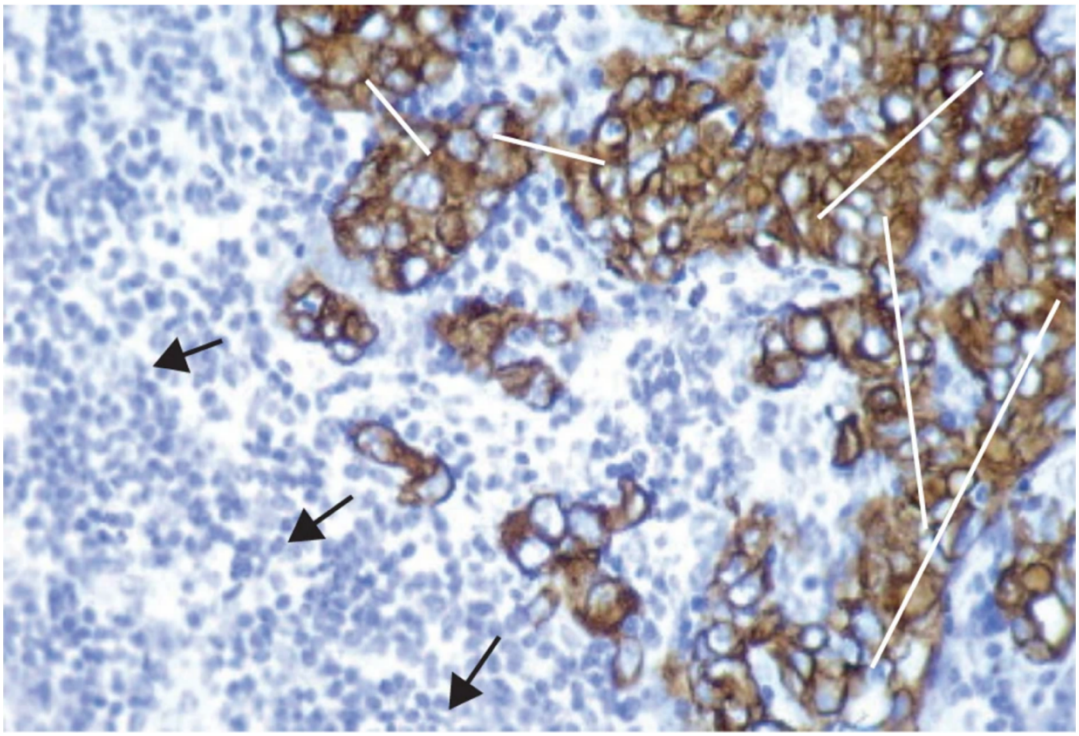


Figure 1.3: Collective cancer invasion: Histological section of a human carcinoma shows epithelial cancer cells (brown, cytokeratin-positive) invading the surrounding stroma as collective multicellular groups. Within the primary tumor mass, cells remain interconnected, while smaller clusters at the invasive front penetrate the surrounding tissue. Arrows indicate the direction of invasion. Adapted from Friedl et al., Nature Cell Biology 2012.

The tumor microenvironment (TME) also plays a key role in regulating cancer cell behavior. The TME includes extracellular matrix (ECM), stromal cells, immune cells, and blood vessels [53]. These components create a heterogeneous and changing environment that influences how tumor cells grow, move, and interact with their surroundings. For example, aligned collagen fibers or stiff ECM can guide the direction of collective invasion. In some cases, the TME can even promote more coordinated

behavior at the tumor edge [10, 54]. Figure 1.4 summarizes how the TME evolves across different stages of tumor progression, from initiation to metastasis, and highlights the cellular players involved at each step [53].

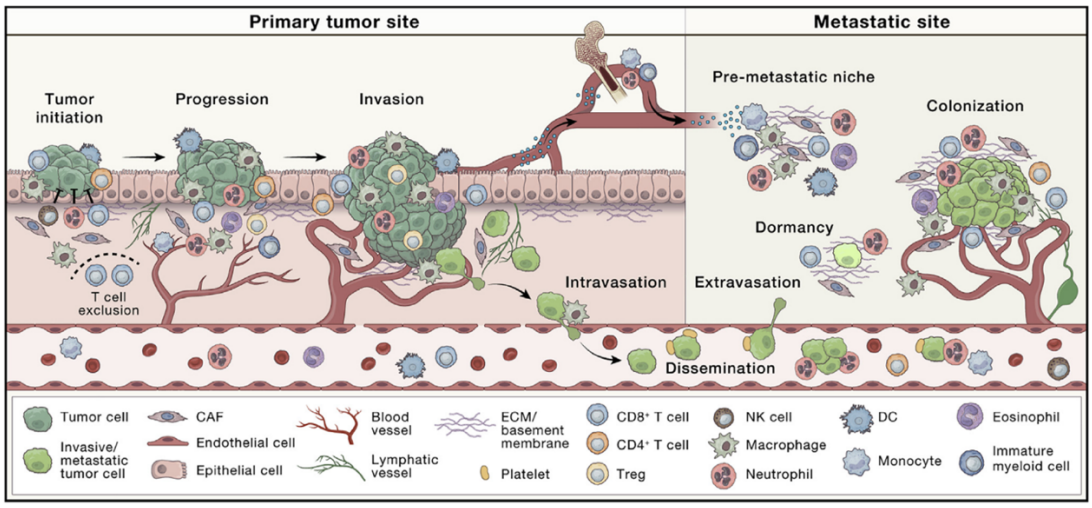


Figure 1.4: Multicellular interactions in the tumor microenvironment: The evolving tumor microenvironment (TME) during cancer progression is shown in the illustration. TME includes diverse cellular components such as cancer-associated fibroblasts (CAFs), endothelial cells, immune populations, and the extracellular matrix (ECM). At the primary tumor site, TME interactions influence tumor initiation, progression, invasion, and intravasation. Disseminated tumor cells travel through the circulation and encounter distinct microenvironments at metastatic sites, where they may enter dormancy, extravasate, and ultimately colonize new tissue. The TME plays both constraining and promoting roles throughout these stages, affecting immune evasion, matrix remodeling, and niche preparation. Adapted from de Visser et al., Cancer Cell 2023.

Genetic mutations also change how tumor cells interact and move. Mutations in genes like KRas, PTEN, or regulators of the cytoskeleton can affect adhesion, contractility, or cell polarity. These changes may increase or decrease collective behavior, depending on the environment [55]. For example, in breast cancer models, some mutations disrupt organized migration, while others make sheets of cells move more strongly as a group [56].

In this thesis, I study how breast epithelial cells with cancer-related mutations change their collective migration behavior. I use the MCF10A cell line and its tumor-related mutations, including KRas activation, PTEN deletion, and KRas/PTEN double mutation, to compare how different genotypes affect group coordination, cell mixing, and clustering. These experiments are performed on both flat and nanoridges substrates to understand how the environment interacts with genotype (Chapter 3). In Chapter 4, I extend this approach to head and neck cancer, where I analyze how myeloid immune cells move in live tissues using optical flow. This allows me to compare collective behavior across cancer cell types and immune cells in different biological contexts.

Together, these studies show that both cancer mutations and the microenvironment shape how cells behave as a group. By using physics-based methods to analyze cell motion, I aim to better understand how tumors grow and spread and how collective behavior may reflect disease state or treatment response.

1.3 Mathematical Metrics of Collective Behavior

To study collective behaviors in biological systems, we need tools that can describe how cells interact and move as a group. These collective dynamics are not always obvious by just looking at individual cells. Instead, they must be measured using quantitative and statistical tools. Many concepts are used to describe collective motion in physics, such as alignment, clustering, and deformation, and can also be applied to cell systems. This allows us to treat tissues and cell populations as physical systems with measurable properties.

A core feature of collective motion is the speed of each cell or voxel, which provides a measure of how actively different regions are moving:

$$v = \frac{|\vec{r}(t + \Delta t) - \vec{r}(t)|}{\Delta t}$$

where $\vec{r}(t)$ is the position vector at time t, and Δt is the time interval between frames. In this thesis, I compute speed using both cell tracking (Chapter 2, 3) and 3D optical flow (Chapter 4, Appendix B). Tracking based speed measures provide resolution per cell, which I use to compare different genotypes and spatial regions in co-culture systems. Optical flow, on the other hand, enables dense motion estimation in tissues where segmentation of individual cells is not easily achievable. This approach allows me to quantify local motion in crowded environments, such as immune cell near lesion sites. Speed measurements help quantify regional differences in motion, identify hotspots of activity, and serve as the basis for speed-weighted metrics. For example, in Chapter 3, I show that KP cells migrate faster than MCF10A cells across both flat and

ridged surfaces. In Chapter 4, speed measurements are used to detect motion hotspots near lesion cites and track their evolution over time.

Directionality is another important property. I analyze angular distributions of motion vectors to capture directional bias. In Chapter 3, this reveals ridge guided alignment of epithelial cells, particularly in the leading edge of migrating fronts. In Chapter 4, I analyze radial bias in immune cell motion around lesions, characterizing how immune cells distribute their motion inward or outward relative to the lesion center. Radial motion bias quantifies how strongly and in what direction local motion is oriented relative to a reference point, typically the center of a lesion. We define it as the cosine of the angle between the 2D velocity vector $\vec{v}$ and the radial vector $\vec{r}_{radial} = \vec{r}_c - \vec{r}$, where $\vec{r}_c$ is the lesion center and $\vec{r}$ is the voxel position:

$$Radial\ Motion\ Bias = \cos\theta = \frac{\vec{v} \cdot \vec{r}_{radial}}{|\vec{v}| \cdot |\vec{r}_{radial}|}$$

A positive value indicates inward motion toward the lesion, while a negative value reflects outward motion away from it. This metric helps capture local coordination relative to lesion structure and may relate to immune infiltration or tissue remodeling.

One concept used in physics is the local order parameter, a number that describes how align the motion vectors are within a spatial neighborhood [21]. If most cells move in the same direction, the order parameter is high. If they move randomly, the order parameter is low. This idea is used in many flocking models and active matter systems in physics [21, 28]. In Chapter 4, I compute a local order parameter within optical flow hotspots to assess motion coherence. Mathematically, it is calculated as the norm of the average unit vectors:

$$\Phi = \left| \frac{1}{N} \sum_{i}^{N} \hat{v}_i \right|$$

where $\hat{v}_i$ is the unit velocity vector of the i^{th} voxel or cell, and N is the number of elements in the neighborhood. A value near 1 indicates strong alignment, while a value near 0 indicates random or divergent motion.

To assess whether different cell populations mix or segregate, I use a contact-based mixing index. The mixing index is defined as:

$$Mixing\ Index = \frac{1}{k} \sum_{j \in \mathcal{N}_i} \delta(s_i \neq s_j)$$

where $\mathcal{N}_i$ is the set of k nearest neighbors of cell i, s_i is the cell type label, and $\delta(s_i \neq s_j)$ is 1 if the neighbor j is of a different cell type, and 0 otherwise. This metric captures the average fraction of heterotypic neighbors per cell and is especially useful in systems with multiple cell types or genetic backgrounds, such as mixtures of normal and cancer cells. In Chapter 3, I use the mixing index to compare how KP and MCF10A cells spatially intermix on flat versus ridged substrates. The analysis shows that nanoridges have minimal impact on cell mixing, with both healthy and metastatic cells exhibiting similar levels of heterotypic contact under the two conditions. Speed-based versions of the metric further highlight differences in activity between the two populations.

When studying dense tissues or monolayers, it is also important to measure local deformation, which tells how cells rearrange relative to their neighbors over time. One metric for this is D^2_{min}, originally developed in the context of plasticity in amorphous solids [30]. In those systems, D^2_{min} captures how particles locally

reorganize under external stress. Although not originally developed for soft matter physics, we translate this idea to biological cell sheets, which can be considered an active material. Unlike passive granular particles, cells are self-propelled and consistently exchange energy with their surroundings through cytoskeletal activity and adhesion forces. In this setting, D^2_{min} provides a way to quantify the local rearrangements driven not only by external confinement but also the internal activity of the cells themselves. So, applying D^2_{min} to epithelial monolayers bridges a metric from granular physics to active matter, revealing how individual cell activity translate into collective deformation and rearrangement patterns at the tissue scale.

D^2_{min} quantifies how much a cell's motion deviates from an affine (uniform) deformation of its local neighborhood:

$$D^2_{i,min} = \frac{1}{N} min\left\{\sum_{j=1}^{N}\left[\overrightarrow{d_{ij}}(t_1) - E_i\,\overrightarrow{d_{ij}}(t_0)\right]^2\right\}$$

In this equation, $D^2_{i,min}$ is the D^2_{min} value for cell i at time $t_1 = t_0 + \Delta t$; N is the number of neighboring cells for cell i; $\overrightarrow{d_{ij}}(t_1)$ and $\overrightarrow{d_{ij}}(t_0)$ are the relative spacing between cell i and neighboring cell j at times t_1 and t_0 , respectively. and E_i is the strain tensor for the neighbor cell group around cell i. A low D^2_{min} value indicates collective, coordinated flow, while a high value reflects local rearrangement or chaotic motion. In this thesis, I apply D^2_{min} in Chapter 2 to compare cell dynamics across cells with different metastatic potentials. Specifically, I show that metastatic cells have higher D^2_{min} values than healthy cells (Figure 1.5), suggesting that cancer-associated mutations lead to more individual and uncoordinated motion, even in a dense

monolayer. I then extend this analysis in later chapters to study cell mixing, spatial organization, and coordination under different genetic and environmental conditions.

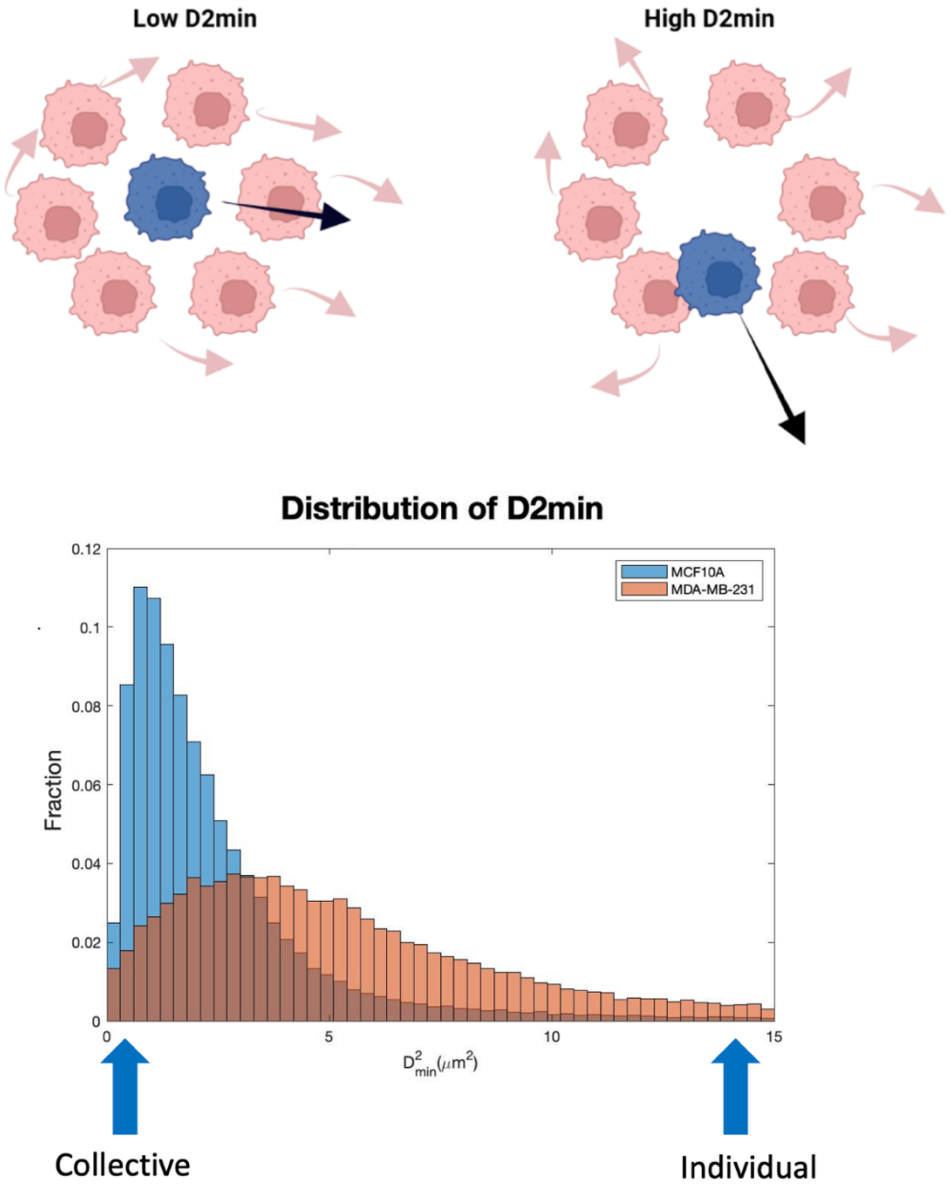


Figure 1.5 D^2_{min} captures the degree of collective versus individual motion. Top: schematic illustration of low and high D^2_{min} behavior. Low values reflect locally affine (coordinated) motion, while high values indicate non-affine, disordered motion where the cell's movement deviates from its neighbors.

Bottom: distribution of D^2_{min} values for healthy MCF10A (blue) and metastatic MDA-MB-231 (orange) cell lines. MCF10A cells show a sharp peak at low D^2_{min}, consistent with collective motion. MDA-MB-231 cells show a broader distribution with a higher fraction of large values, indicating more individualistic behavior.

In Chapter 4, I develop a hotspot tracking approach to capture regions of high myeloid activity. These hotspots are defined by thresholding motion magnitude after smoothing, then grouped and tracked over time. The order parameter is also used within hotspots to assess whether motion is coherent or disordered.

While not included in figures in the following chapters, I also explored complementary tools that offer additional insight. For example, I tested the radial distribution function (RDF) $g(r)$ in Chapter 3 to evaluate spatial clustering, though this was not emphasized in the final analysis. RDF is defined as:

$$g(r) = \frac{1}{2\pi r \Delta r \rho N} \sum_{i=1}^{N} n_i(r, \Delta r)$$

where $n_i(r, \Delta r)$ is the number of neighboring cells located within the annular shell from r to $r + \Delta r$ around cell i, N is the number of reference cells, ρ is the average cell density, and $2\pi r \Delta r$ is the area of the shell used for normalization in 2D. This metric allows us to determine whether cells are more or less clustered than expected by chance. A value of $g(r) > 1$ indicates local clustering, $g(r) < 1$ suggests exclusion zones or regular spacing, and $g(r) = 1$ corresponds to a random distribution. As shown in Figure 1.6, in a co-culture of 10A and KP cells, RDFs were computed for both the overall population and cell-type-specific interactions. The sharp peak in the 0→0 curve

(type 0 looking at other type 0 cells) reveals enhanced homotypic clustering at short distances, while heterotypic curves (e.g., 0→1, 1→0) are comparatively flatter. These results support the partial segregation patterns also reflected in the mixing index analysis.

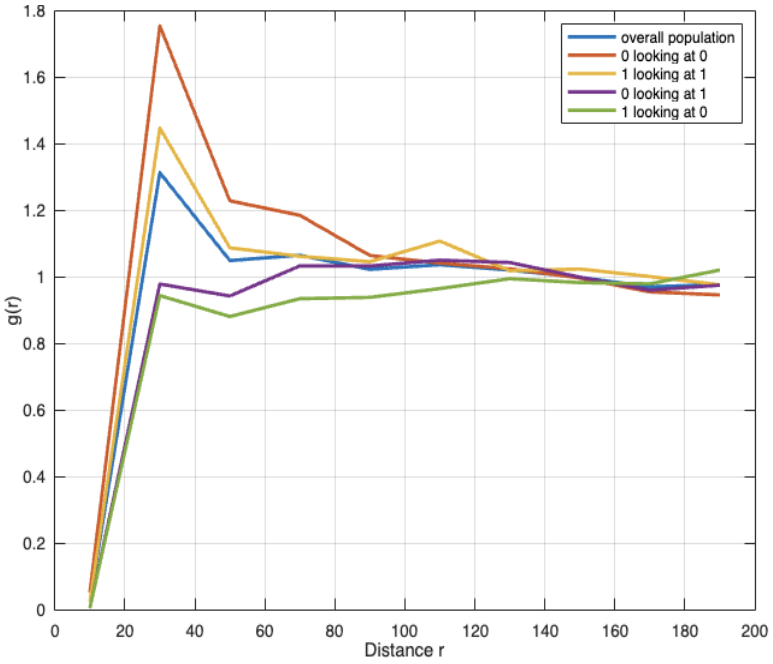


Figure 1.6 Radial distribution functions (RDFs) reveal spatial organization in mixed cell populations. In a co-culture of healthy and metastatic cells, RDFs were computed for all cells (blue), as well as for specific cell-type interactions: type 0 looking at type 0 (orange), type 1 at 1 (purple), type 0 at 1 (yellow), and type 1 at 0 (green). Peaks at short distances indicate clustering, while values near g(r) suggest random distribution. The sharper peak in the "0 looking at 0" curve suggests stronger homotypic clustering among type 0 cells, consistent with partial segregation.

In this thesis, I apply physics-based tools to extract meaningful features from complex biological motion. These methods allow me to go beyond qualitative observation and quantify deformation, coordination, and rearrangement across systems. By applying the metrics described in Table 1, I demonstrate how physical quantitative analysis can reveal organizing principles in diverse biological systems.

Metric	Definition / Equation	Chapters	Potential Biological Relevance
Speed	$v = \frac{\lvert\vec{r}(t+\Delta t) - \vec{r}(t)\rvert}{\Delta t}$	2, 3, 4	Indicates motility levels; elevated in active or migratory cells.
Radial Motion Bias	$Radial\ Motion\ Bias = \cos\theta = \frac{\vec{v} \cdot \vec{r}_{radial}}{\lvert\vec{v}\rvert \cdot \lvert\vec{r}_{radial}\rvert}$	3, 4	Reflects inward vs. outward motion relative to lesion centers.
D^2_{min}	$D^2_{i,min} = \frac{1}{N}\ min\left\{\sum_{j=1}^{N}\left[\overrightarrow{d_{ij}}(t_1) - E_i\overrightarrow{d_{ij}}(t_0)\right]^2\right\}$	2, 3	Detects local rearrangements; linked to tissue remodeling or disordered motion.
Mixing Index	$Mixing\ Index = \frac{1}{k}\sum_{j\in N_i}\delta(s_i \neq s_j)$	3	Quantifies intermixing between distinct cell types.
Hotspot Tracking	Thresholding and labeling of high-magnitude regions in smoothed optical flow	4	Identifies regions of concentrated collective motion, highlight sites of elevated immune activities.
Order Parameter	$\Phi = \lvert\frac{1}{N}\sum_{i}^{N}\hat{v}_i\rvert$	4	Measures directional alignment; high values suggest coordinated migration.
Radial Distribution Function (RDF)	$g(r) = \frac{1}{2\pi r\Delta r\rho N}\sum_{i=1}^{N} n_i(r,\Delta r)$	—	Captures spatial clustering or spacing patterns among cells

Table 1: Summary of collective motion metrics used in this thesis. Each metric captures a distinct feature of collective cell behavior, ranging from individual motion intensity (speed), orientation (angular bias), and deformation (D^2_{min}), to group-level properties like cell mixing, hotspot detection, and local alignment (order parameter). Some exploratory analyses, such as radial distribution function (RDF), provide additional insight into spatial organization. Metrics are annotated with their definitions, the chapters in which they are applied, and notes on interpretation or usage context.

These metrics capture complementary aspects of collective dynamics, from local motion strength and directionality to spatial organization and mechanical heterogeneity. Their consistent use across Chapters 2, 3, 4 provides a framework for comparing diverse cell systems and uncovering how genetic or environmental factors alter collective behavior.

1.4 The Interaction Between Cell Type and Environment in Collective Behavior

Although collective behavior arises from local cell-cell interactions, it is highly sensitive to the surrounding microenvironment. In biological systems, this includes both biochemical signals and physical cues such as substrate stiffness, surface geometry, confinement, and ECM. These environmental factors shape how cells interact, migrate, and self-organize, where that even identical cells may behave very differently in different physical contexts. To fully understand collective behavior, it is essential to consider the dynamic interplay between intrinsic cellular properties and external physical cues. While many studies focus on how environmental cues influence cell behavior, it is equally important to recognize that cells of different types can respond to the same environment in fundamentally distinct ways. In the following sections, we explore two complementary perspectives: first, how different cell types behave differently under identical conditions (Section 1.4.1), and second, how a single cell type can alter its behavior across distinct environments (Section 1.4.2).

1.4.1 Different cell types respond differently to the same microenvironment

Genetically distinct or functionally specialized cells can react differently to the same physical conditions. This is especially important in mixed systems where one population may align, coordinate, or migrate efficiently in a given environment, while another becomes disorganized or unresponsive. In my study different cells' response to elongate mineral particles (EMP) [57], I demonstrated this principle by comparing the behavior of epithelial and immune cells exposed to the same rigid, asbestos-like fibers. Although both cell types encountered the same substrate geometry, their cytoskeletal responses are different: macrophages show heightened cytoskeleton activities at the EMP sites compared to epithelial cells. This suggests that cell type plays a critical role in determining how environmental structure influences collective behavior.

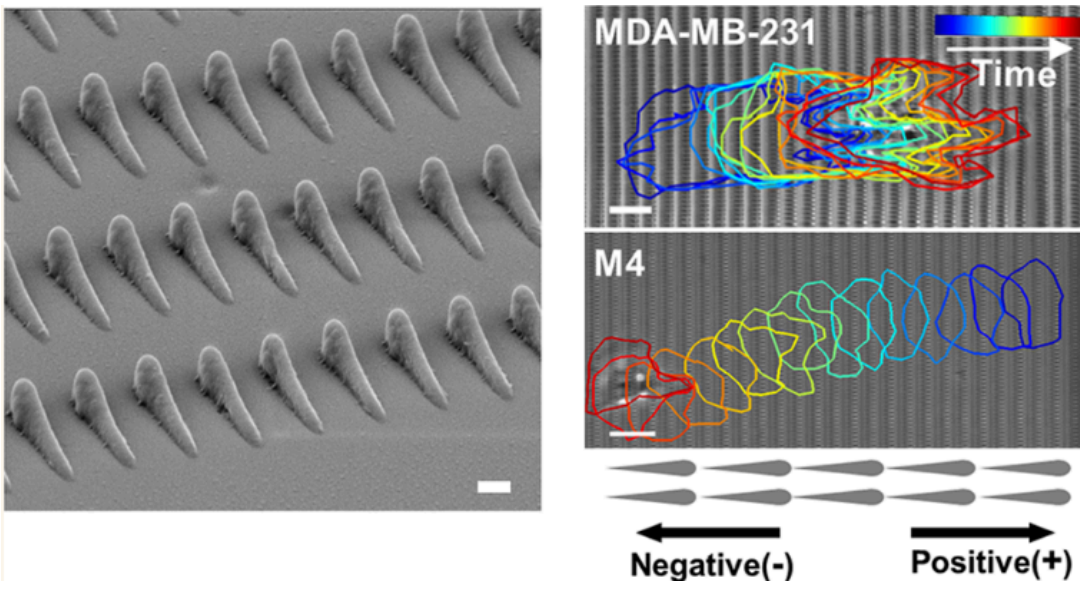


Figure 1.7: Cell-type-specific migration on asymmetric sawtooth nanotopography. Breast cancer cells show distinct migratory responses to the same asymmetric sawtooth substrate. Scanning electron micrograph (left) shows the details of the nanoscale surface. Time-lapse overlays of cell tracks (right) reveal that MDA-MB-231 cells migrate slowly in the positive direction, while M4 cells move persistently in the negative direction defined by sawtooth asymmetry. These divergent behaviors highlight how intrinsic cytoskeletal and adhesion dynamics shape cell interpretation of shared physical environments. Adapted from Chen et al., ACS Nano 2019.

A similar principle has been observed in breast cancer cells migrating on identical asymmetric sawtooth nanotopographies. As shown in Figure 1.7 [58], MDA-MB-231 and M4 cell lines were exposed to the same nanoscale substrate, but migrated in opposite directions. Chen et al. demonstrated that this divergence might be related to differences in how actin polymerization dynamics and cytoskeletal organization interact with substrate asymmetry. Although stiffness was not measured, it is plausible that difference in cortical mechanics also contribute to how each cell type interprets the asymmetric geometry. These findings highlight that even under identical external environments, intrinsic cytoskeletal and mechanical properties can dictate the direction and mode of collective migration [58].

In Chapter 2 and 3, I further explore this idea using engineered epithelial cell lines with defined cancer mutations. Even when cultured under identical substrate and media conditions, healthy MCF10A cells and metastatic KRAS/PTEN mutant cells show different levels of coordination and spatial organization. These differences are

further amplified by topographical cues such as ridge patterns, reinforcing the idea that genotype interacts with environmental structure to shape collective outcomes.

1.4.2 The same cell type behaves differently in different microenvironments

Even genetically identical cells can behave very differently when their physical context is changed. For example, cells cultured on soft substrates often migrate more slowly or randomly, while the same cells on stiff substrates exhibit faster and more persistent motion [40, 59]. Similarly, surface features such as grooves or confinement geometries can promote alignment, clustering or elongation behaviors that are not observed on flat surfaces [17, 60]. In other words, collective dynamical characteristics are not fixed traits of cells, they are emergent properties that adapts to external conditions.

In the same EMP study (Appendix A) [57], I investigated how rigid minerals of different diameters affect cytoskeletal organization in epithelial and immune cells. We found that fiber geometry strongly influenced cytoskeletal signaling, with thinner fibers inducing greater actin and accumulation. Notably, this response varied by cell type: epithelial and immune cells showed different levels and patterns of cytoskeletal activation in response to the same physical structures. These results support the idea that cell-type-specific mechanical responses to microenvironmental features can shape the potential for coordinated or collective behavior, even in the absence of direct motion measurements.

Overall, these examples emphasize that collective behavior cannot be interpreted without considering the physical landscape in which it occurs. In this thesis, I combine genotype-controlled systems and well-defined physical environments to study how collective phenotypes vary with both internal and external parameters. By comparing behaviors across epithelial cell lines, immune populations, and lesion environments, I aim to uncover general principles for how structure and context guide group dynamics.

1.5 Thesis Outline

This thesis aims to develop and apply quantitative, physics-based analysis tools to study collective behaviors across scales. I focus on how physical metrics of cell motion, deformation, and coordination can reveal emergent patterns in genetically and phenotypically diverse cell populations. In particular, I explore how genotype and microenvironment shape the migration and organization of epithelial and immune cells, with applications to cancer progression and immune response.

In Chapter 2, I investigate the collective migration of breast epithelial monolayers composed of healthy MCF10A cells and cells carrying oncogenic mutations (KRas activation, PTEN deletion, and the double mutant). I analyze how these mutations alter population-level behavior using metrics from soft matter physics. Motion metrics such as speed, D^2_{min}, and local coordination are used to compare dynamics across genotypes. I show that the cancer-mutant cell lines exhibit more chaotic and uncoordinated behavior, highlighting how genetic alterations influence emergent physical properties of the migrating sheet.

Chapter 3 extends this work to study mixtures of healthy and mutant cells. I quantify spatial mixing, clustering, and coordination across genetically distinct populations, and examine how these behaviors are modulated by substrate topography. Ridge-patterned surfaces introduce a physical cue that interacts with genotype, producing different degrees of mixing compared to flat substrates. I develop and apply statistical tools to quantify how physical structure affects the degree of mixing, local alignment, and rearrangement within cell collectives.

In Chapter 4, I turn to an in vivo system to study immune cell behavior in the tumor microenvironment. Using a 4NQO-induced model of head and neck squamous cell carcinoma, Weigert lab image the migration of myeloid cells in live mice over time using two-photon microscopy. I apply a 3D optical flow algorithm to capture voxel-level motion fields in the region of lesion. By quantifying motion magnitude, directionality, and spatial organization, I identify collective features in the immune response and examine whether early motion patterns correlate with lesion progression or regression. This chapter bridges physics-based analysis with cancer immunology to explore how immune collectives behave in dynamic tissue contexts.

In the Appendix A, I include an additional study focused on how elongate mineral particles (EMPs), such as asbestos fibers, impact cytoskeletal organization in different cell types. I show that thinner fibers induce stronger actin responses, and that epithelial and immune cells differ in how they respond to the same physical obstacle. Although migration was not directly measured in that study, the findings demonstrate how environmental structure selectively activates intracellular machinery, supporting the broader idea that microenvironment shapes collective potential.

Chapter 2: Label-free cell tracking enables collective motion phenotyping in epithelial monolayers

This chapter is adapted from the manuscript by Gu, Lee, Benson, Ling, Vitolo, Martin, Chalfoun, and Losert, originally published in *iScience* on June 27, 2022. Shuyao Gu served as the lead graduate researcher on this study, developed and performed the analysis, and wrote a first draft of the manuscript. Her main contribution lies in creating a label-free analysis pipeline that integrates deep-learning based segmentation with tracking and the D^2_{min} metric, enabling the capture of dynamical differences directly from phase contrast images, which was not previously possible.

2.1 Overview

Collective cell migration is an umbrella term for a rich variety of cell behaviors, whose distinct character is important for biological function, notably for cancer metastasis. One essential feature of collective behavior is the motion of cells relative to their immediate neighbors. We introduce an AI-based pipeline to segment and track cell nuclei from phase-contrast images. Nuclei segmentation is based on a U-Net convolutional neural network trained on images with nucleus staining. Tracking, based on the Crocker-Grier algorithm, quantifies nuclei movement and allows for robust downstream analysis of collective motion. Because the AI algorithm required no new training data, our approach promises to be applicable to and yield new insights for vast libraries of existing collective motion images. In a systematic analysis of a cell line

panel with oncogenic mutations, we find that the collective rearrangement metric, D^2_{min}, which reflects non-affine motion, shows promise as an indicator of metastatic potential.

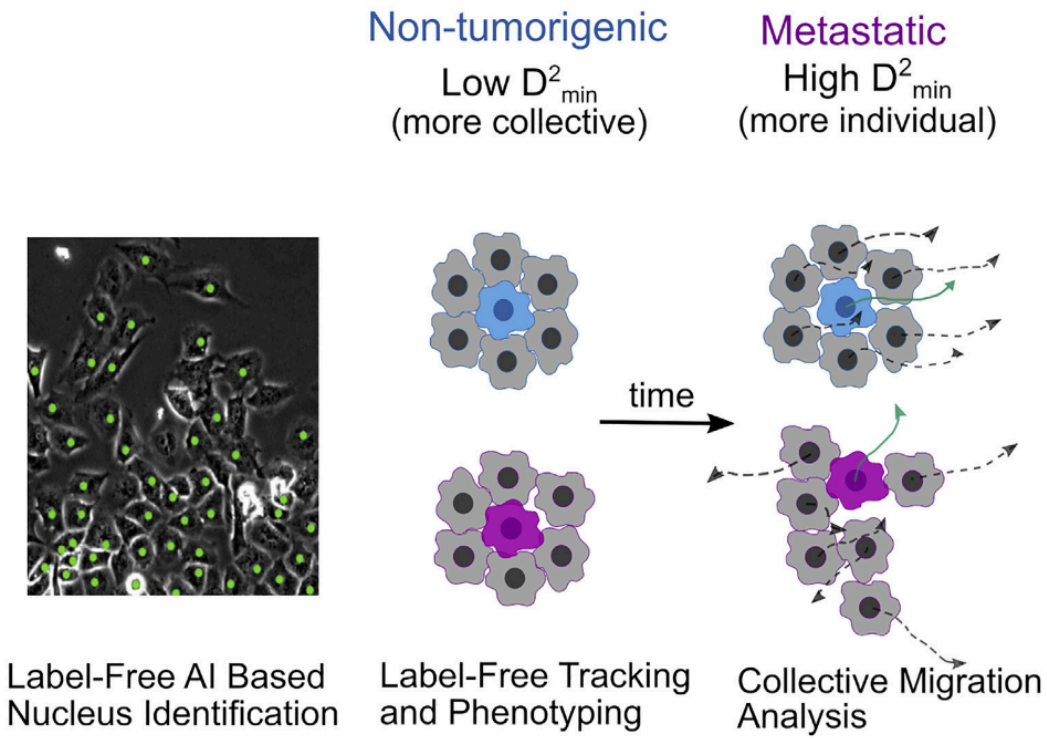


Figure 2.1: Graphical abstract. This study combines label-free AI-based nucleus identification with cell tracking and quantitative migration analysis to compare collective behaviors between non-tumorigenic and metastatic epithelial cells. Using D^2_{min} as a metric for local non-affine motion, we find that non-tumorigenic cells exhibit lower D^2_{min} and more coordinated movement, whereas metastatic cells show higher D^2_{min} and more individualistic behavior.

2.2 Background

Breast cancer is one of the most common cancers in women. Many breast-cancer-related deaths result from metastasis, a complex, multistep process in which cancer cells migrate away from the primary tumor and eventually grow in other organs [61-63]. During the met-astatic process, clusters of primary tumor cells can leave the original site, circulate in the bloodstream, and seed secondary tumor growth at distant sites. There is growing evidence that tumor cells that collectively migrate and enter the bloodstream as clusters (defined as any group larger than one cell) are 50-100 times more likely than individual cells to lead to metastasis [64-66]. Characterization of collective motion is generally accomplished in one of two ways: particle image velocimetry (PIV) applied to phase contrast movies, which ignores individual cellular characteristics, or tracking applied to fluorescent labels, which tend to affect cell behavior. Here, we introduce a new artificial intelligence (AI) -based approach to track the motion of individual cells from phase contrast movies. This AI-enabled cell tracking allows us to characterize a shifting balance between individual motion and collective motility of mammary epithelial cells as they become more transformed, tumorigenic, and metastatic.

We use a commonly studied breast epithelial cell line (MCF10A), a highly metastatic cell line (MDA-MB-231), and a genetically defined model system for cancer and metastasis. The genetically defined model system is based on the MCF10A cell line and introduces phosphatase and tensin homolog deletion ($PTEN^{-/-}$) and/or overexpression of activated KRas (G12V), two common oncogenic mutations that have downstream impacts on the cytoskeleton. PTEN loss is found in 24% of breast cancers

[67] and has been associated with poorer prognoses in many solid tumors [68]; KRas is a frequent driver of tumors across different types of human cancers [20, 69]. This model cell system relates our results to in vivo outcomes, since the cell lines have been characterized in terms of tumorigenicity [70] and metastatic behavior [71].

In a previous study, we imaged the motion of groups of cells from these cell lines in a well-defined in vitro assay [72] and characterized the motion using PIV. We found that deletion of PTEN caused cells to move more collectively, while KRas activation had the opposing effect [56]. However, when both mutations were present, the phenotype induced by KRas dominated and the KRas and KRas/PTEN$^{-/-}$ cell lines displayed similar dynamics [56, 71], even though they have significantly different in vivo outcomes. One might think that malignancy would lead to higher cell motility; however, these model cell lines and others with characterized in vivo behavior do not show a clear correlation between cell speed and malignancy [72, 73]. One limitation of PIV is that it characterizes motion based on the movement of all features in an image. Thus, PIV captures overall movement visible in an image, including the motion of the many organelles visible in a typical phase contrast image, which may obscure the full motion of each cell's nucleus. However, the cell nucleus serves as the main reference point of a cell, steering cell motion [74] and defining orientation when compared to the microtubule-organizing center [75].

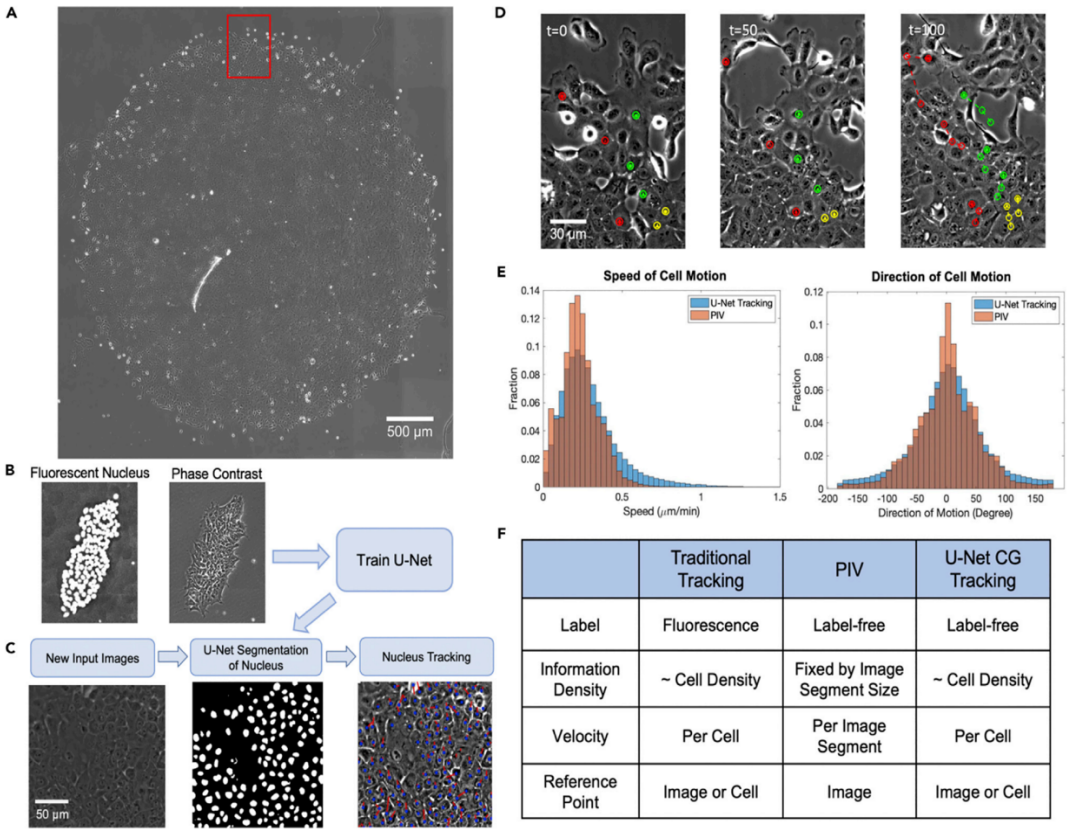
In this study, we introduce an AI-enabled (U-Net) cell nucleus segmentation tool for epithelial cells [76] that allows us to track cell nuclei and study their dynamics. The AI model was trained on stem cell images with Lamin B1 stain for automated nucleus detection [76] and did not require further training to perform nucleus

segmentation on the studied epithelial cell sheets. Additionally, our AI-enabled single-cell tracking allows us to characterize motion of cells relative to their neighbors. In particular, we borrowed a metric from soft matter physics, D^2_{min} [30, 56, 77], to describe the extent of similarity of motion between the cell of interest and its closest neighbors. This ability to assess how closely a cell follows its neighbors yields a phenotype of cell rearrangements during collective migration capable of differentiating the metastatic KRas/PTEN$^{-/-}$ from the non-metastatic cell lines. AI-enabled tracking and quantification of collective rearrangements thus provide new tools for quantifying metastatic potential and could be used to improve patient diagnosis or to develop novel therapeutic targets.

2.3 Analysis and Results

2.3.1 AI-based analysis workflow enables label-free single-cell tracking

To study the collective dynamics of migrating epithelial monolayers, we developed an analysis pipeline that extracts single-cell positions from phase contrast images using a U-Net-based deep learning model. This approach eliminates the need for fluorescent nuclear labeling. The U-Net model was originally trained on phase contrast images of stem cell colonies with matched nuclear ground truth and was robust to common imaging noise and intensity variations. Despite being trained on a specific dataset, the model generalizes well to epithelial lines such as MCF10A, accurately identifying nuclear positions across a wide range of conditions (Figure 2.2 A–C).



	Traditional Tracking	PIV	U-Net CG Tracking
Label	Fluorescence	Label-free	Label-free
Information Density	~ Cell Density	Fixed by Image Segment Size	~ Cell Density
Velocity	Per Cell	Per Image Segment	Per Cell
Reference Point	Image or Cell	Image	Image or Cell

Figure 2.2: AI-based segmentation and tracking workflow captures collective migration behavior. (A) A tiled image of a migrating cell sheet. The red box indicates the size of the field of view captured over time. (B) An example of human iPSC clonal line images used as the training set for U-Net. (C) Computational workflow: an input image is segmented using U-Net, and then the centroids of the segmented cell nuclei are tracked using the Crocker-Grier algorithm. (D) Tracks of 8 cells from t = 0 to frame 100 (3 min per frame; frames t = 0, 50, and 100 shown). (E) Comparisons of tracking results with PIV results. (F) Table comparing benefits of traditional tracking, PIV, and U-Net Crocker-Grier tracking.

Segmented nuclei were tracked over time using a center-based tracking algorithm (Crocker-Grier), enabling hundreds of cells to be followed across time-lapse image sequences (Figure 2.2D). We validated this tracking approach by comparing nuclear dynamics to those measured using particle image velocimetry (PIV) on the same datasets. The U-Net tracking produced distributions of speed and directionality that largely matched PIV-based measurements, with high Bhattacharyya coefficients for both speed (0.971) and direction (0.991), indicating strong agreement between the two methods (Figure 2.2E).

Our U-Net-based method offers a label-free alternative to fluorescent nuclear tracking, avoiding potential phototoxic effects while maintaining robust performance. Compared to PIV, it additionally provides individual cell-level data, enabling high-resolution analysis of collective behavior (Figure 2.2F).

2.3.2 A quantitative metric for cell rearrangements distinguishes tumorigenic and metastatic cell lines

With the ability to follow individual cells in a sheet, we can compute how cells move relative to their neighbors. One measure of collective rearrangements, D^2_{min} (Equation 1), has been used in models of elastoplastic deformation of amorphous solids or granular materials [78] to describe the motion of particles relative to their neighbors. Analyzing a cluster of N particles, D^2_{min} characterizes departures from the local affine deformation by fitting overall motion of the cluster over a time Δt to an affine deformation and reporting the residue.

$$D^2_{i,\,\min} = \frac{1}{N}\min\left\{\sum_{j=1}^{N}\left[\vec{d}_{ij}(t_1) - E_i\,\vec{d}_{ij}(t_0)\right]^2\right\} \qquad \text{(Equation 1)}$$

In Equation (1), $D^2_{i,min}$ is the D^2_{min} value for cell i at time $t_1 = t_0 + \Delta t$; N is the number of neighboring cells for cell i; $\overrightarrow{d_{iJ}}(t_1)$and $\overrightarrow{d_{iJ}}(t_0)$are the relative spacing between cell i and neighboring cell j at times t_1 and t_0, respectively. and E_i is the strain tensor for the neighbor cell group around cell *i*. We chose $N = 6$ under the assumption that epithelial cells have on average six neighbors in a confluent sheet. D^2_{min} [30, 79] (Equation 1) is a least-squared calculation in which the final relative spacing between cells, $d_{ij}(t_1)$, is predicted via a linear transformation, E_i, of the initial relative spacing $d_{ij}(t_0)$, (Figure 2.3A). The resulting difference is called non-affine (non-linear) motion, whereas the $E_i d_{ij}(t_0)$ is the affine motion. E_i is fit to minimize the difference between the affine motion and the actual motion. The affine component, which reflects collective motion, is essentially how well the displacements of the neighboring cells can predict the motion of the central cell. A lower D^2_{min} value indicates the cell motion is more affine, meaning the cell more closely follows its neighbors' motion and is moving more collectively. A higher value of D^2_{min} thus implies a more individualistic or non-affine motion.

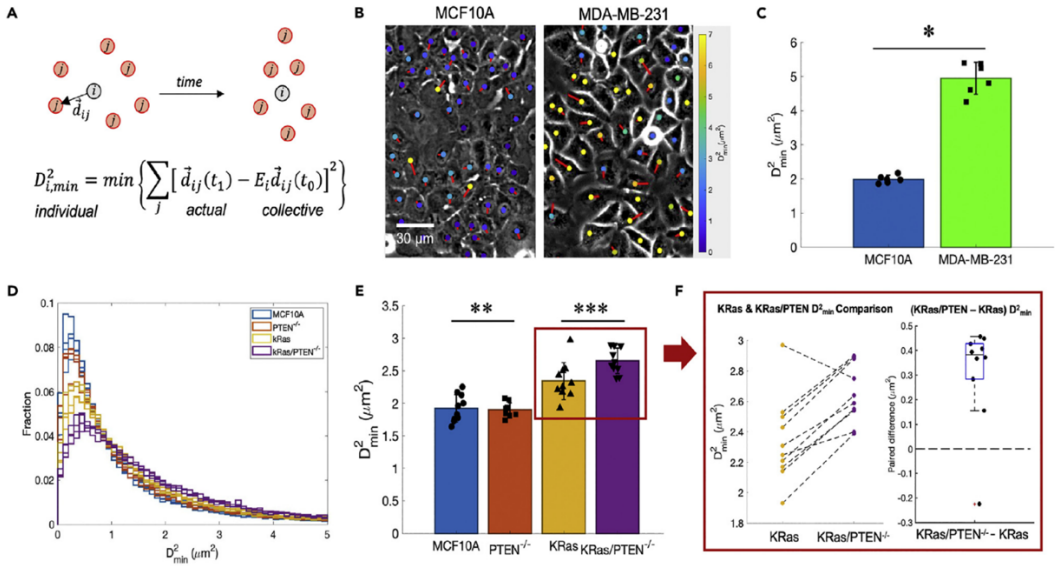


Figure 2.3: Cell rearrangements distinguish tumorigenic and metastatic cell lines. (A) A schematic of how D^2_{min} is calculated. (B) Sheets of migrating cells labeled by their motion and rearrangements. Colorful dots represent D^2_{min} values for individual cells, with their values indicated by the color bar. Red arrows show the direction of cell motion. (C) Comparison of average D^2_{min} values for MCF10A and MDA-MB-231 cells over 6 independent experiments. (D) Comparison of D^2_{min} distribution of MCF10A mutants in one set of experiments (4 technical replicates of each mutant). (E) Average D^2_{min} for each mutant over 10 independent experiments. (F) Pairwise comparison of KRas and KRas/PTEN$^{-/-}$ D^2_{min}. (left) Dashed lines connect experiments performed on the same 12 well plate. (right) The central line indicates the median value of the paired difference, while the top and bottom edges of the box indicate the 75th and 25th percentiles. Error bars in c, e represent the standard deviation across independent replicates. Data are represented as mean ± SD. "*" = $p < 0.001$, "" = $p = 0.78$, "***" = p = 0.01. Two-sample t-test.**

Using our proposed U-Net-based segmentation and tracking workflow, we calculate D^2_{min} for both MCF10A (non-tumorigenic) and MDA-MB-231 (metastatic) breast cells. This reveals strong differences in their rearrangement behavior. Figure 2B shows single frames from a time-lapse series in which cell nuclei are marked using colorful dots according to their respective D^2_{min} value. The non-tumorigenic MCF10A cells behave more collectively (lower D^2_{min} values) compared to the metastatic MDA-MB-231 cells (Figure 2.3C).

We also applied our U-Net cell tracking workflow, without additional training of the AI algorithm, on a genetically defined cancer progression model system based on the MCF10A cells [70]. In this model system, cells with PTEN deleted ($PTEN^{-/-}$) have previously been found to remain dormant *in vivo*. KRas-activated cells also usually stay dormant *in vivo*; however, sometimes the KRas cells can form primary tumors (poorly tumorigenic) [56, 70]. The double mutant ($KRas/PTEN^{-/-}$) is aggressively tumorigenic [70] and metastatic [71]. Figure 2.3D showcases the D^2_{min} distribution from four technical replicates for each cell line from one experiment. The D^2_{min} distribution for each cell line is consistent across technical replicates and the combined experiment shows the overall trend that the original MCF10A and $PTEN^{-/-}$ mutants have smaller D^2_{min} values, which means that their motion is more collective, and cells tend to follow their neighbors' motion. The overall results from 10 independent experiments (Figure 2.3E) confirm the poorly tumorigenic KRas and metastatic $KRas/PTEN^{-/-}$ mutants have higher D^2_{min} than the non-tumorigenic MCF10A and dormant $PTEN^{-/-}$ mutants. To further differentiate the KRas and

KRas/PTEN$^{-/-}$ mutants, a pairwise comparison was performed (Figure 2.3F). A blocked experimental design allows us to pairwise compare the D^2_{min} value within each experiment, depicted by dashed line connecting the raw values (Figure 2.3F, left), and by directly subtracting the KRas D^2_{min} value from the KRas/PTEN$^{-/-}$ D^2_{min} value (Figure 2.3F, right). The results show that most experiments yield the metastatic KRas/PTEN$^{-/-}$ having higher D^2_{min} than the poorly tumorigenic KRas mutant. Therefore, the KRas/PTEN$^{-/-}$ mutant motion is more individual (non-affine) than the KRas mutant, and D^2_{min} can distinguish the poorly tumorigenic KRas and metastatic KRas/PTEN$^{-/-}$ cell lines.

2.3.3 Affine motion quantifies changes in collective behavior

To further study the collective component of cell motion, we extract affine dilation and deformation components from the minimized linear transformation matrix E_i (Equation 1) [30]. We decompose the 2D matrix E_i into a product of two matrices: a pure rotation matrix $R(\theta)$ and a symmetric strain tensor F. The average of the eigenvalues of the strain tensor F corresponds to affine dilation, while the difference is the affine deformation. Physically, the two eigenvalues describe the contraction or expansion in the direction of their respective eigenvectors. Affine dilation represents the collective contraction or expansion of the group of 6 neighbors. Affine deformation describes whether the cells' neighbors are compressed or stretched. Schematics shown in Figure 2.4A illustrate examples of affine dilation and deformation in a 6-neighbor system.

We know from analysis of the nuclear tracks that the metastatic MDA-MB-231 cells have a larger average motion than the non-tumorigenic MCF10A cells (Figure 2.5). Affine calculations reveal that the MDA-MB-231 cells also display larger deformations and dilations (Figure 2.4B). Thus, the larger average total motion observed in the MDA-MB-231 cells has a collective component. The MCF10A mutants have similar affine dilation and deformation (Figure 2.4C). Combining data from all 10 experiments (Figure 2.4D), the magnitude of affine/collective motion among MCF10A mutants is similar.

Next, we compare the contribution of the two components of motion, affine (collective) and non-affine (individual), to the cell sheet's direction of motion. Angular distributions of both components (Figure 2.4E) show that the non-affine motion is roughly uniformly distributed in all directions, while the directions of affine motion favor the directional cue provided by empty space in the experimental system (roughly 90 degrees in the figures). This shows that the collective migration of cell sheets is mostly led by affine motion, where individual cells more closely follow their neighbors' motion. The non-tumorigenic MCF10A and dormant $PTEN^{-/-}$ cell lines show much more directional affine motion than the poorly tumorigenic and metastatic cell lines.

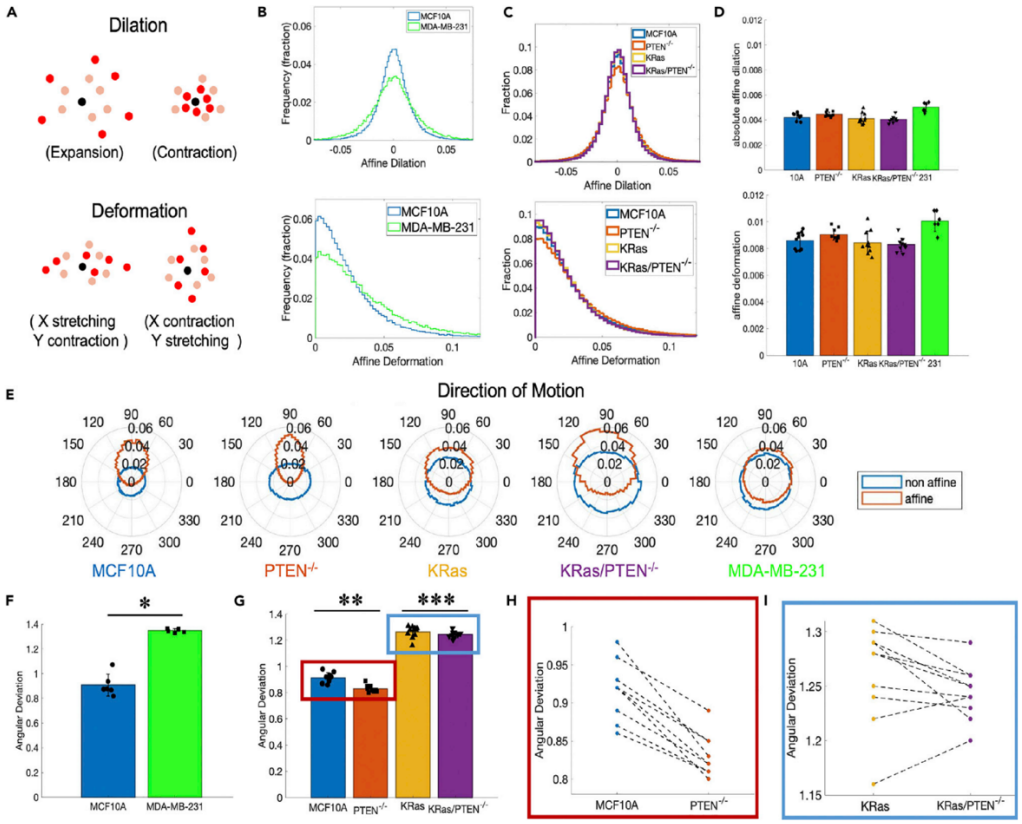


Figure 2.4: The affine component of motion describes collective behavior. (A) Schematics of affine dilation (top) and affine deformation (bottom), with pink dots indicating the original positions of nuclei and red dots representing their positions at a later time. (B) Representative distributions of affine deformation and dilation comparing the MCF10A and MDA-MB-231 cells. (C) Representative distributions of affine deformation and dilation comparison for the MCF10A mutants. (D) The absolute value of affine dilation and average affine deformation for MCF10A mutants (10 independent experiments) and 231 cells (6 independent experiments). (E) The direction of affine and non-affine motion for representative experiments for the MCF10A mutants and MDA-MB-231. (F) MCF10A and MDA-MB-231 affine angular deviation. (G) MCF10A mutants' affine angular

deviation. (H) Pairwise comparison of MCF10A and PTEN$^{-/-}$. (I) Pairwise comparison of KRas and KRas/PTEN$^{-/-}$. Error bars represent the standard deviation across independent replicates. Data are represented as mean ± SD. "*" = $p < 0.001$, "" = $p < 0.001$, "***" = $p = 0.32$. Two-sample t test.**

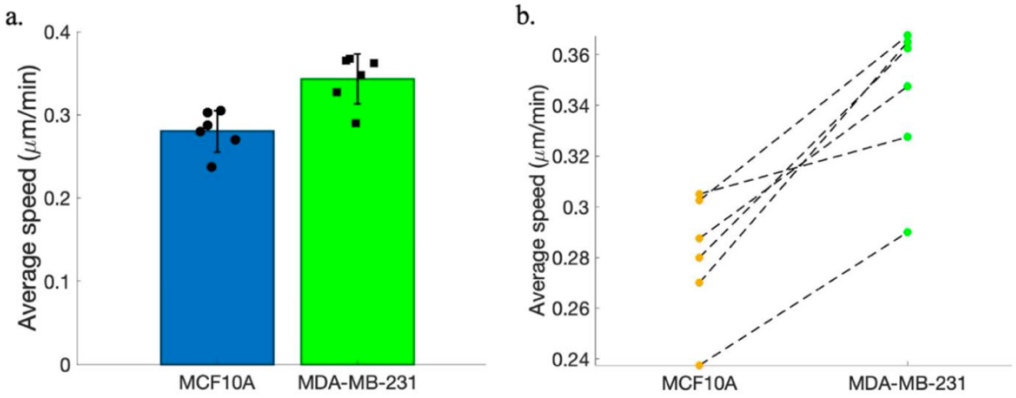


Figure 2.5: MDA-MB-231 cells exhibit increased overall motion. (a) The average speed of MCF10A and MDA-MB-231 cells (6 independent experiments). Error bars represent the standard deviation across independent replicates. (b) Pairwise comparison of MCF10A and MDA-MB-231.

We calculate angular deviation for both affine and non-affine motion among all cell lines to quantify the spread of these distributions. Angular deviation values range from 0 to $\sqrt{2}$, with 0 meaning all cells are moving in one direction and higher values indicating a more dispersed set of migration directions. The non-affine motion of all cell lines has an angular deviation near $\sqrt{2}$, which confirms the observation that non-affine motion has no directional preference (Figure 2.4E). Meanwhile, the angular deviation differs for the affine (collective) motion across the different cell lines. The

affine motion of the MCF10A cells is much more directional than the metastatic MDA-MB-231 cells (Figure 2.4F). Among the MCF10A model system, KRas and KRas/PTEN$^{-/-}$ have significantly higher affine motion angular deviations compared to MCF10A and PTEN$^{-/-}$, indicating the collective motions of the poorly tumorigenic (KRas) and metastatic (KRas/PTEN$^{-/-}$) cell lines are less directional (Figure 2.4G). A pairwise comparison to MCF10A shows that PTEN$^{-/-}$ cells have the lowest angular deviation (Figure 2.4H), indicating that PTEN deletion leads to more directional movement consistent with prior PIV analysis [72]. We note that pairwise comparison of KRas and KRas/PTEN$^{-/-}$ mutants shows that PTEN deletion does not have a similar effect of increasing directionality of collective motion in KRas mutants (Figure 2.4I).

2.3.4 Quantification of cell rearrangements by D^2_{min} is robust to tracking errors

To test the robustness of our findings, 20% of the cells were randomly removed in each frame to simulate a cell segmentation error situation, which might occur with non-ideal imaging or segmentation parameters. The U-Net applied here was trained on a different cell line, without any retraining. We manually segmented a set of images and found a segmentation accuracy of at least 80% with respect to detecting all cell nuclei in the sample (Figure 2.6). As such, the removal of 20% of the tracked cells is a good simulation to test the measurement robustness of our pipeline to expected segmentation errors. Figure 2.7A shows the original data, with each cell nucleus (segmented by U-Net) labeled in yellow and a frame where 20% of the identified nuclei

are labeled for removal (red). Our D^2_{min} analysis is still able to distinguish between the KRas and KRas/PTEN$^{-/-}$ cell lines, as shown in Figures 2.7B and 2.7C. With the removal of 20% of cells, the D^2_{min} of these four cell lines maintain the same overall trends, including KRas/PTEN$^{-/-}$ consistently exhibiting higher D^2_{min} than the cell line mutated in KRas alone. The average neighbor distance (Figure 2.7D) slightly increases and is accompanied by a slightly smaller D^2_{min} for all cell lines with 20% cell removal. In other words, the decrease of cell density from artificially removing cells leads to lower D^2_{min}. So, the larger neighbor distance seen in KRas/PTEN$^{-/-}$ cells cannot explain the higher D^2_{min} found in these cells. This means that high D^2_{min} for KRas/PTEN$^{-/-}$ reflects individualistic motion. Neighbor distances, or cell density might be impacted by tracking accuracy; however, Figures 2.7A and 2.7B show that the D^2_{min} metric can distinguish poorly tumorigenic from metastatic cell lines even when tracking accuracy is artificially lowered.

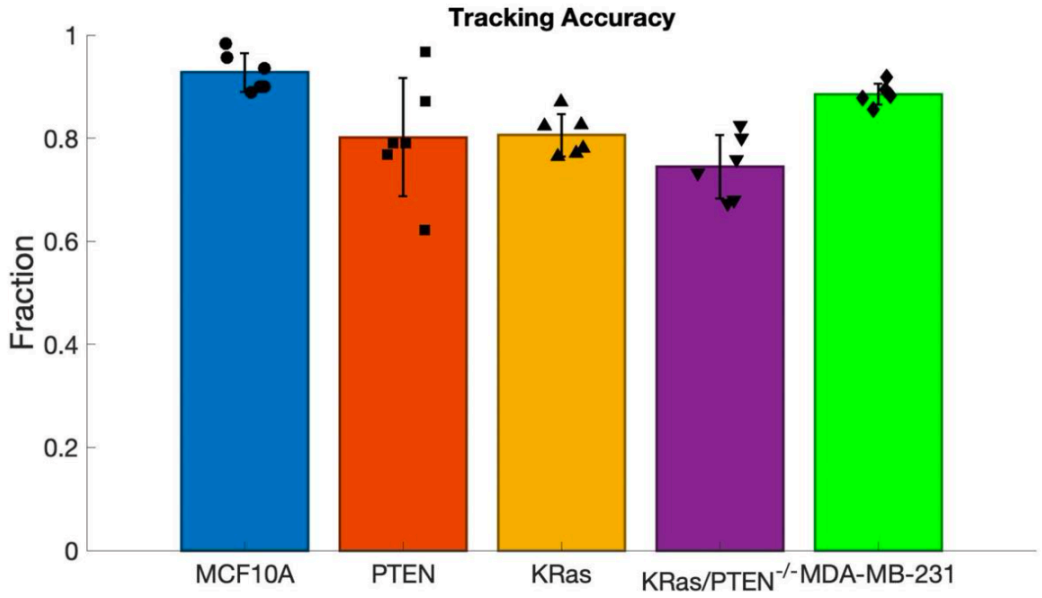


Figure 2.6: Manual assessment of tracking accuracy. We define accuracy of tracking per frame to be the number of cells found by the tracking minus any double counted cells, divided by the total cell number. The number of cells in each frame were manually counted using the Fiji Cell Counter plugin (https://imagej.net/plugins/cell-counter). We calculated the tracking accuracy on 3 independent experiments for each MCF10A mutants and MDA-MB-231 cells by manually assessing frame 20 (1hour) and frame 220 (11 hour) in the image sequence. Error bars represent the standard deviation.

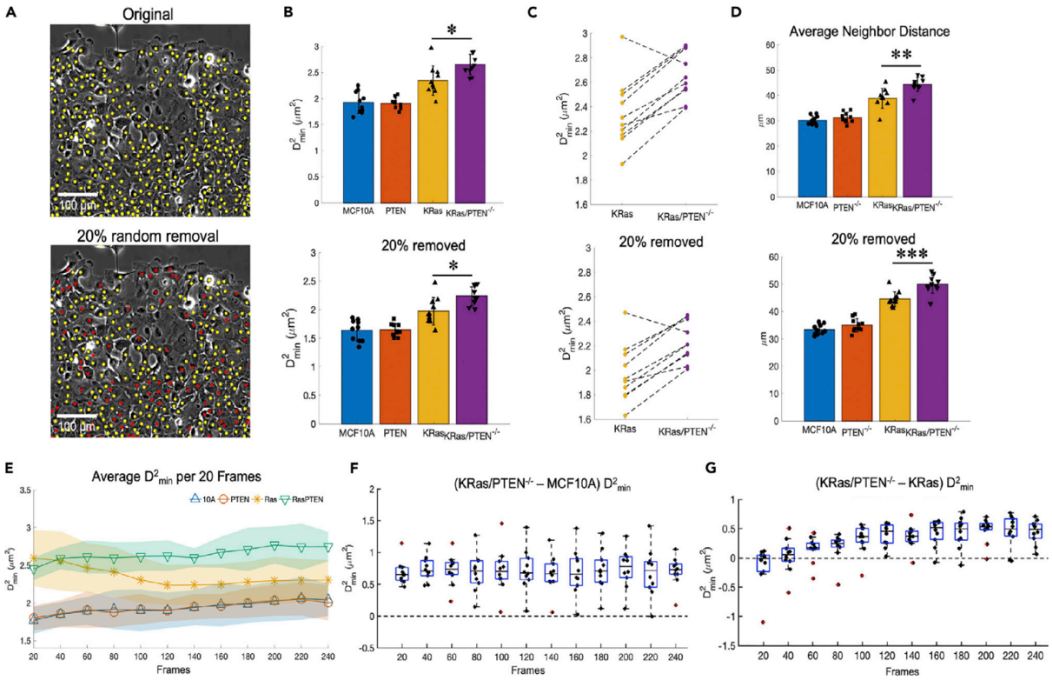


Figure 2.7 D^2_{min} is robust to potential tracking errors. (A) Top: a sheet of MCF10A cells, with all U-Net-segmented nuclei labeled in yellow; bottom: the same sheet of MCF10A cells, with 20% of nuclei randomly removed from tracking (indicated in red). (B) Top: average D^2_{min} for 10 independent experiments from U-Net-

segmented nuclei; bottom: average D^2_{min} with 20% of nuclei randomly removed in each frame. (C) Pairwise D^2_{min} comparison of KRas and KRas/PTEN$^{-/-}$. (D) Average neighbor distance. (E) Average D^2_{min} per 20 frames (60 min) for the MCF10A mutants over time (shaded regions represent the standard deviation across independent replicates). (F) Average D^2_{min} difference between KRas/PTEN$^{-/-}$ and original MCF10A per 20 frames (60 min) over time. (G) Average D^2_{min} difference between KRas/PTEN$^{-/-}$ and KRas per 20 frames (60 min) over time. For boxplots, the central line indicates the median value, while the top and bottom edges of the box indicate the 75th and 25th percentiles. Error bars in B, D represent the standard deviation across independent replicates. Data are represented as mean ± SD. "*" = $p = 0.01$, "" = $p = 0.02$, "***" = $p < 0.001$. Two-sample t test.**

Next, we investigate the change in motion with time over the 12 h timescale of our experiments. We segmented the data into 20-frame pieces and found the average D^2_{min} over each time segment, as shown in Figure 2.7E. The shaded regions in the plot are the standard deviations for D^2_{min} values over 10 experiments. The poorly tumorigenic KRas and metastatic KRas/PTEN$^{-/-}$ have consistently higher D^2_{min} compared to the non-tumorigenic MCF10A and dormant PTEN$^{-/-}$ cells at all timepoints. The KRas cells' D^2_{min} value decreases over the first 120 frames and then stabilizes; the KRas/PTEN$^{-/-}$ mutant D^2_{min} values slightly increase over time. These two time-related behaviors lead to the KRas/ PTEN$^{-/-}$ cells having a higher time-averaged D^2_{min} value, as shown in Figures 2.3E and 2.3F. Over the 12 h of imaging (240 frames), the metastatic KRas/PTEN$^{-/-}$ consistently has higher D^2_{min} than the non-tumorigenic MCF10A (Figure

2.7F), indicating that D^2_{min} is a robust comparison between non-tumorigenic and metastatic cells. Comparing the KRas/PTEN$^{-/-}$ and KRas cells (Figure 2.7G), we find that their motion is initially similar, but differences emerge 120 frames (6 h) after the start of imaging, or 30 h after cell plating. At later times, 20 frames (60 min) of imaging are sufficient for D^2_{min} to distinguish the KRas/ PTEN$^{-/-}$ and KRas cell lines.

2.4 Discussion

We present an AI-enabled label-free nuclear tracking method capable of identifying the motion of cell nuclei and use this information to quantify the collective behavior of panels of cell lines. We study the MCF10A epithelial cell line and its variants with cancer-related mutations, specifically contrasting KRas activation alone and in conjunction with PTEN deletion. These two oncogenic mutations yield different outcomes in vivo but their associated motion characteristics have been indistinguishable when analyzed with prior methods [71, 72].

Our nuclear segmentation is done by an AI model previously trained on a human iPSC clonal line [76]. The parameters of the tracking algorithm maintain a temporary memory of cells that disappear in a frame or two due to imaging or segmentation issues and remove tracks that are too short, improving successful cell tracking and reducing noise. With these quality-control features, we can segment and track on average 80% of the nuclei in an image for MCF10A and MDA-MB-231 cell lines without further training on U-Net (Figure 2.6).

The successful application of the AI model on these two cell lines suggests that our AI model and tracking algorithm are versatile and can be applied to other epithelial cell lines without an extra training set. Moreover, random removal of 20% of the nuclei yielded consistent D^2_{min} results (Figure 2.7), suggesting that we are tracking a large enough fraction of cells for robust calculations not prone to change with tracking errors. Being versatile and robust to errors, we can use our workflow to track and analyze the collective motion for a variety of different types of cells.

Based on measuring the individual motion of cells, D^2_{min} is capable of clearly distinguishing nontumorigenic and tumorigenic cells and is also able to distinguish the poorly tumorigenic KRas and the metastatic KRas/PTEN$^{-/-}$ cells (Figure 2.3F). The D^2_{min} calculation (Equation 1), provides multiple metrics for understanding collective migration behavior. In addition to D^2_{min}, which measures the balance of collective vs individual behavior, the calculation quantifies ‘‘affine’’ motion characteristics, namely, the magnitudes and preferred directions of dilations and deformations. Both our previous PIV and current U-Net tracking results show that PTEN deletion makes cells more collective and more directional (Figure 2.4), while KRas activation makes cells less collective (Figures 2.3 and 2.7). However, D^2_{min} highlights the differences between the poorly tumorigenic KRas and metastatic KRas/PTEN$^{-/-}$ cell lines (Figure 2.3), regardless of the similarities in their collective behavior (Figure 2.4). The metastatic cell line (KRas/PTEN$^{-/-}$) has the most individual motion, which leads to more local rearrangements in the sheet, impacting the overall collective migration of the cell sheet. This individual motion may be the result of a loss in cell adhesion in tumor progression [80], favoring tumor invasion and metastasis. Our analysis of

collective and individual motions has the potential to be applied to distinguish non-tumorigenic, tumorigenic, and metastatic cells for easier and faster diagnosis.

In summary, we introduce an AI-enabled label-free nucleus tracking workflow for phase-contrast imaging that can follow the motion of cells without the need for new AI training data. The comprehensive assessment of cell motion is critical in enabling us to characterize collective motion using D^2_{min}, which provides a local metric of collective motion that shows differences between metastatic and non-metastatic cell lines. Our results indicate that AI-enabled collective motion measurements may provide a new perspective on the identification and diagnosis of metastatic risk.

2.5 Materials and Methods

2.5.1 Cell Migration Datasheet

No cell culture or imaging experiments were conducted for this study. The images of cell migration used in this work are a freely available dataset in the Image Data Resource [56]. This previously published dataset was collected on the MCF10A human breast epithelial cell line, MCF10A PTEN$^{-/-}$, MCF10A KRas(G12V), MCF10A KRas(G12V)/PTEN$^{-/-}$ [70], and the MDA-MB231 breast cancer cell line. MCF10A cells were maintained in DMEM/F12 medium supplemented with 5% horse serum, 10 mg/mL insulin, 0.5 mg/mL hydrocortisone, and 100 ng/mL cholera toxin. For comparisons between the MCF10A, MCF10A PTEN$^{-/-}$, MCF10A KRas(G12V), and MCF10A KRas(G12V)/PTEN$^{-/-}$ cells, the media was additionally supplemented with

0.5 mg/mL puromycin to select for LifeAct-GFP. MDA-MB231 cells were maintained in DMEM supplemented with 10% FBS.

For this published dataset, cells were plated in 12 well glass-bottom plates using a complete block design, which allows for pairwise comparisons between cell sheets imaged on the same plate. Each well was coated with 3.25 mg/cm2 collagen IV by placing the plate on ice and leaving 500 mL of collagen IV solution (3.25 mg/cm^2 collagen IV in 0.05 M HCl) on each well for 1 h before rinsing twice with water. A 5 mL drop of 1.5 3 106 cells/mL was plated in the center of each well, allowed to adhere for approximately 45 min at 37 C, and then rinsed to remove non-adherent cells. This created a circular cell sheet, which was then allowed to adhere overnight before imaging, followed by a medium change 1 h before the start of imaging. An initial snapshot of the entire cell sheet was recorded by tiling multiple positions before focusing on ROIs for time lapse imaging. Cells were then imaged every 3 min for 12 h using a 103 phase-contrast objective (Nikon CFl Plan Fluor, NA 0.3) on a PerkinElmer Ultra-View VoX spinning-disk confocal with a Tokai Hit incubator chamber (37C and 5% CO2) and a motorized stage for acquiring multiple positions over time. Images were acquired using a Hamamatsu C10600-10B ORCA-R2 camera (12 bit images 1024 pixels 3 1344 pixels, 0.582 mm/pixel) using PerkinElmer's Volocity software (version 6.4.0). The initial analysis of these images is described in [56] and the image files are available in the Image Data Resource under DOI [https://doi.org/10.17867/10000163a][56].

2.5.2 Image and Migration Analysis

Cell nuclear segmentation from phase contrast images was performed by a pre-trained U-Net model [76], which generated labeled binary images of inferred connected objects representing nuclei. We used a custom MATLAB code to filter out connected objects that are significantly smaller than the average physiological nucleus size; this step filters out imaging and segmentation noise. The centroid of each nucleus was found using the *regionprops* function in MATLAB. The Crocker-Grier algorithm [77], as implemented by Blair & Dufresne for MATLAB, performs nuclear tracking on the centroids and outputs the tracks of each nucleus for each frame. A custom MATLAB neighbor-finding code [72] was used to find the closest 6 neighbors for each cell nucleus in each frame. This output was then used to calculate D^2_{min} and the affine components of motion as described in the section below.

Angular deviation, s, was calculated as $s = \sqrt{(2(1 - R))}$, where each tracking vector was transformed into a unit vector in the two-dimensional plane: $r_i = (\cos\theta_i, \sin\theta_i)$, and R is the length of the vector average of the direction vectors:

$R = || (1/N) \Sigma_i r_i ||$.

2.5.3 D^2_{min} and Affine Analysis

$$D^2_{i,\,min} = \frac{1}{6}\min\left\{\sum_{j=1}^{6}\left[\vec{d}_{ij}(t_1) - E_i\,\vec{d}_{ij}(t_0)\right]^2\right\} \qquad \text{(Equation 1)}$$

D^2_{min} is calculated using Equation (1) by minimizing the difference between the final relative position of a cell and its neighbors, $\bar{d}_{ij}(t_1)$, and the affine component, which is a linear transformation of the initial relative position, $E_i\ \bar{d}_{ij}(t_0)$. The 2 × 2 linear transformation matrix E that is fit in the D^2_{min} equation was decomposed to further describe the affine components of motion. We rewrite the matrix as a product of a pure rotation R(θ) and a symmetric deformation matrix F: E = R(θ)F which we can expand as shown in Equation (2). The angle of rotation, θ, can then be found by substituting the elements of E into Equation (3).

$$E = \begin{bmatrix} \cos(\theta) & \sin(\theta) \\ -\sin(\theta) & \cos(\theta) \end{bmatrix} \begin{bmatrix} f_1 & 0 \\ 0 & f_2 \end{bmatrix} = \begin{bmatrix} \cos(\theta)f_1 & \sin(\theta)f_2 \\ -\sin(\theta)f_1 & \cos(\theta)f_2 \end{bmatrix} = \begin{bmatrix} e_1 & e_2 \\ e_3 & e_4 \end{bmatrix} \quad \text{(Equation 2)}$$

$$\theta = tan^{-1}\left(\frac{e_2 - e_3}{e_1 + e_4}\right) = tan^{-1}\left(\frac{\sin(\theta)f_2 - (-\sin(\theta)f_1)}{\cos(\theta)f_1 + \cos(\theta)f_2}\right) = tan^{-1}\left(\frac{\sin(\theta)(f_1 + f_2)}{\cos(\theta)(f_1 + f_2)}\right) = tan^{-1}\left(\frac{\sin(\theta)}{\cos(\theta)}\right) \quad \text{(Equation 3)}$$

The deformation matrix F can then be found using $F = R^{-1}(\theta)E$. We further define a strain tensor ε = F - I. The subtraction of the identity matrix from F ensures that its eigenvalues would be 0 if no deformation, positive if stretching, and negative if compressing. The affine deformation is calculated as the difference between the two eigenvalues of matrix F, and affine dilation is the average of the eigenvalues. Examples of θ, R(θ), F, ϵ, are given in Figure 2.8.

For instances of skipped frames, we keep a memory of disappearing cells in the tracking algorithm, however, metrics like velocity and D^2_{min} are calculated for frames of the track where the previous and later frames are not missing data.

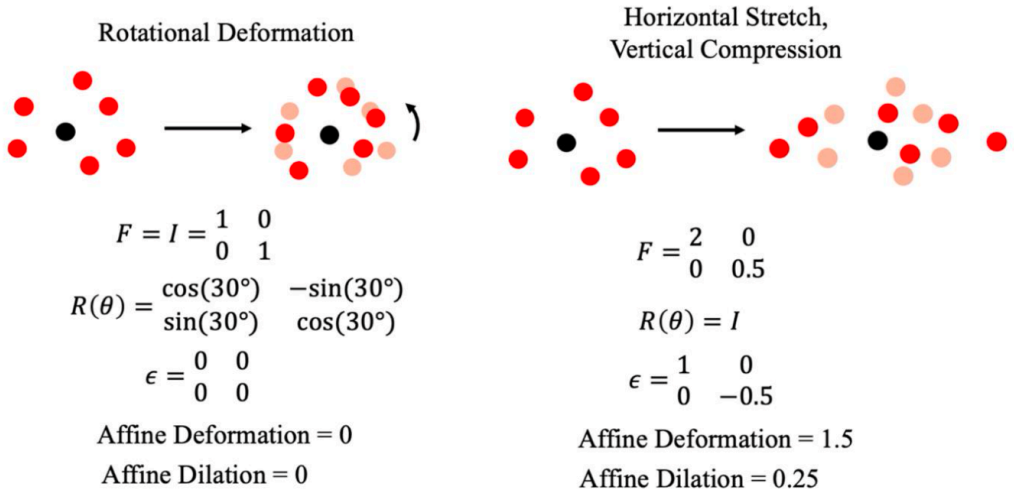


Figure 2.8 Examples of affine parameters. Two examples are given to showcase the before and after of local cell groups and their corresponding θ, R(θ), F, ϵ, affine deformation and dilation.

The D^2_{min} calculation is done in the reference frame of an individual cell. Therefore, to extract the affine and non-affine motion components of the lab frame motion, we performed a change of reference frame. For example, we calculated the D^2_{min} value for a cell with 6 neighbors from a time t_1 to t_2. Then the expected difference in motion between cell i and neighbors j at t_2 is $E_i \bar{d}_{ij}(t_1)$, where $\bar{d}_{ij}(t_1)$ is the difference motion at time t_1: $\bar{d}_{ij}(t_1) = r_i(t_1) - r_j(t_1)$. Thus, the expected (affine) neighbor position in the lab frame at time t_2 is given by Equation 4.

$$r_{j,affine}(t_2) = E_i \vec{d}_{ij}(t_1) + \vec{d}_{ij}(t_1) + r_i(t_2) = E_i \vec{d}_{ij}(t_1) + r_j(t_1) + (r_i(t_2) - r_i(t_1)) \quad \text{(Equation 4)}$$

Equation (4) is the neighbor location in the lab frame plus the cell displacement over time plus the expected motion difference between cell and neighbors. We then can

find the difference between the expected and actual positions for neighbors in the lab frame. Then, taking the average of over 6 neighbors, we get the non-affine motion of the cell compared to its neighbors. To get the affine component of the motion, we simply subtract the calculated non-affine motion from the actual (total) motion.

2.5.4 Quantification and Statistical Analysis

For each metric, means shown in the respective figures were calculated from N = 10 independent experiments for the MCF10A genetically defined model system and N = 6 for comparisons to the MDA-MB-231 cells. Error bars represent the standard deviation across independent replicates unless otherwise noted. In boxplot figures, the central line indicates the median value, while the top and bottom edges of the box indicate the 75th and 25th percentiles. Outliers on the boxplots (red plus symbols) were defined as values greater than 1.5 times the interquartile range (IQR indicated by the boxplot whiskers). Statistical signification test presented as asterisks are calculated using two-sample t test. All the calculations are done using MATLAB.

Chapter 3: Cell Mixing and Guidance on Ridges

This chapter is adapted from the manuscript of Gu, Rosemore, Dalang, Zhao, Lockhart, Fourkas, and Losert in preparation. Shuyao Gu is the lead junior researcher on this study and performed all the experiments, led and developed the analysis, and wrote the first draft of the manuscript.

3.1 Overview

Although every cell in a tissue has its own distinct characteristics, large genetic differences can lead to cell-type-specific migration and sorting. These behaviors are relevant to cancer metastasis, which begins when a subset of tumor cells segregate from the surrounding tissue. Here, we investigate how surface nanotopography influences the organization and dynamics of epithelial monolayers composed of a mixture of healthy (MCF10A) and metastatic (KP) breast epithelial cells. We show that nanoridges enhance the speed and directional alignment of collective migration, particularly at the leading edge of a cell sheet. Both cell types move faster and more directionally on ridges, and the motility differences observed between monocultures of the two cell lines are suppressed in co-culture. KP cells show greater elongation on ridges than do MCF10A cells. Spatial mixing between the two cell types is limited on flat surfaces and is not significantly altered by nanoridges. These results indicate that physical cues that can shape collective motion may still have a minimal influence on the spatial organization within dense, adherent tissues, in which intrinsic cell–cell interactions dominate.

3.2 Background

Advances in proteomics have enabled the detailed study of the spatial heterogeneity of protein expression in tissues [81, 82]. In tumors such spatial heterogeneity is particularly pronounced, and is correlated with disease progression, treatment resistance, and metastatic potential [83]. Genomic studies have revealed that tumor clones are spatially segregated within both primary and metastatic sites [84, 85]. This spatial heterogeneity has been linked to worse outcomes in, for instance, prostate cancer [85].

Collective invasion is a common migration mode in epithelial cancers, such as breast cancer and melanoma. After escaping the primary tumor microenvironment, cancer cells migrate as cohesive groups, guided by physical cues such as aligned collagen fibers, which correlate with a poor prognosis [86-88]. Similar guidance has been observed along muscle fibers and axons in melanoma models [89].

The mechanism behind clonal segregation is not understood completely. The differential adhesion hypothesis (DAH) posits that sorting is driven by differences in cell–cell adhesion [90], but recent work has shown that segregation of epithelial and mesenchymal breast cancer cells does not always follow the predictions of the DAH [91]. Thus, factors beyond adhesion, including the mechanical microenvironment, may contribute to sorting.

These observations suggest two key hypotheses. First, distinct cell types may respond differently to the same physical microenvironment; indeed, this concept is supported by studies showing that cells of different oncogenic backgrounds adopt unique migratory behaviors on identical substrates [58, 92, 93]. Second, within a single

cell type, migration is highly plastic, and is modulated by the local physical context, such as substrate alignment or nanotopography.

Here, we test how intrinsic oncogenic identity and extrinsic nanoscale cues combine to regulate collective migration and spatial organization in breast epithelial systems. We examine how nanoscale surface topography affects the collective migration and spatial arrangement of healthy and metastatic breast epithelial cells, both in monoculture and in co-culture. Our model cell lines were MCF10A (10A) and a metastatic MCF10A KRas(G12V)/PTEN$^{-/-}$ derivative (KP), and we employed both flat and nanoridged substrates. Prior work using droplet-based assays suggests that collective motion becomes more disordered with increasing oncogenic mutations [31, 56]. We used live-cell imaging over 18 h and applied an automated analysis pipeline combining Cellpose-based segmentation [94], trajectory tracking, and shape quantification. We find that although nanoridges significantly enhance the collective migration speed and directional alignment of both cell lines, particularly at the leading edge of a cell sheet, nanoridges do not measurably alter the spatial mixing between KP and 10A cells. Principal component analysis (PCA) of cell shapes further reveals that KP cells are more mechanically responsive than MCF10A cells, showing increased elongation on nanoridges. These findings allow us to decouple the effects of cell–cell adhesion from those of physical guidance and provide insights into how physical cues and cell identity shape collective behavior in cancer.

3.3 Analysis and Results

3.3.1 Nanotopography Alters Sheet Morphology Without Changing Spatial Mixing

Our experiments and analysis focus on the spatial arrangement and dynamics of migrating monolayers of epithelial cells carrying different cancer-related mutations. In each experiment, we mixed two cell types, one of which was labeled with a fluorescent dye to distinguish between the populations (Fig. 3.1a). We used healthy 10A epithelial cells and their metastatic KP counterparts with PTEN deletion and KRas activation.

To study how the collective dynamics of cell mixtures interact with esotaxis cues, we plated the cells on biocompatible nanoridged substrates (Fig. 3.1b). The nanoridges served as guidance cues. Monolayers of the mixed cultures were time-lapse imaged using both phase-contrast and fluorescence microscopy to track the behavior of both cell types (Fig. 3.1c).

A number of methods have been developed to analyze the dynamics of cell monolayers. Particle-image velocimetry, for instance, provides insights into collective motion, and deep learning-based tools such as customized UNet models enable the tracking of individual cells [31]. However, the presence of nanoridges requires a more adaptable segmentation approach. We adopted Cellpose [94], a generalist algorithm with a human-in-the-loop feature, to train and apply a robust, AI-based segmentation model. After segmentation, we computed cell centroids and tracked individual cells [77] to analyze motion and interactions. The fluorescent labels allowed us to distinguish

between the two cell types and to track each type individually in the mixed cultures. This capability enabled the downstream analysis of both collective motion and spatial organization.

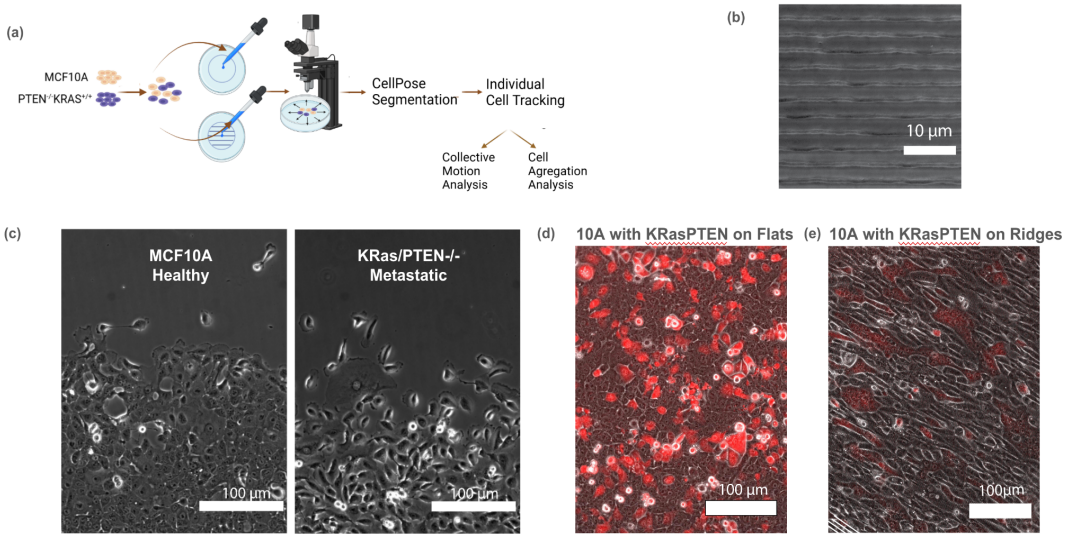


Figure 3.1: Nanoridges modulate the morphology of epithelial cell mixtures. (a) Schematic of the experimental workflow. Time-lapse images of mixed cultures of MCF10A (10A, healthy) and KRas/PTEN$^{-/-}$ (KP, metastatic) epithelial cells were analyzed using CellPose segmentation and individual cell tracking. Quantitative analyses included collective motion and local aggregation metrics. (b) A representative scanning electron micrograph (SEM) of the nanoridged substrate. (c) Representative phase-contrast images of monocultures of 10A and KP cells. (d–e) Representative images of mixed cultures on (d) flat and (e) nanoridged substrates. In (d), the KP cells are labeled in red and 10A cells are not labeled. In (e), 10A cells are labeled in red and the KP cells are not labeled.

Figure 3.1d shows a representative example of combined phase-contrast and fluorescence images of a mixed monolayer on a flat substrate. The KP cells are

fluorescently labeled and the 10A cells are unlabeled. We observed that cells tended to remain near neighbors of the same type and to form small clusters, with the cluster size depending on the cell type.

Figure 3.1e shows a representative image of mixed monolayer on nanoridges. In this case the 10A cells are fluorescently labeled and the KP cells are unlabeled. In comparison to the cell morphology on flat surfaces, cells on nanoridges became elongated along the ridge direction. The mixing behavior also changed in the nanoridges. The KP cells tended to have more same-type neighbors than on flat surfaces, whereas the 10A cells showed reduced local clustering.

To study cell mixing, we developed an analysis workflow that combine phase-contrast segmentation, cell-identity labeling, and centroid tracking (Fig. 3.2a). Phase-contrast images were first segmented using Cellpose [94]. From each segmented cell area, we extracted and tracked the cell centroid position using the Crocker–Grier algorithm [77], a classical particle-tracking method that is used widely for dense monolayers. In parallel, we used the corresponding fluorescence images to classify each cell by type. Because only one of the two cell types was labeled with a fluorescent dye in each experiment, we computed the mean fluorescence intensity within each cell mask and applied a threshold to distinguish labeled versus unlabeled cells. These classifications were assigned to full-length tracks, enabling us to reconstruct trajectories of both healthy and metastatic cells with known identity. Figure 3.2b shows examples of segmented fluorescence images overlaid with centroids, confirming the accuracy of our segmentation and labeling approaches on both flat and ridged substrates.

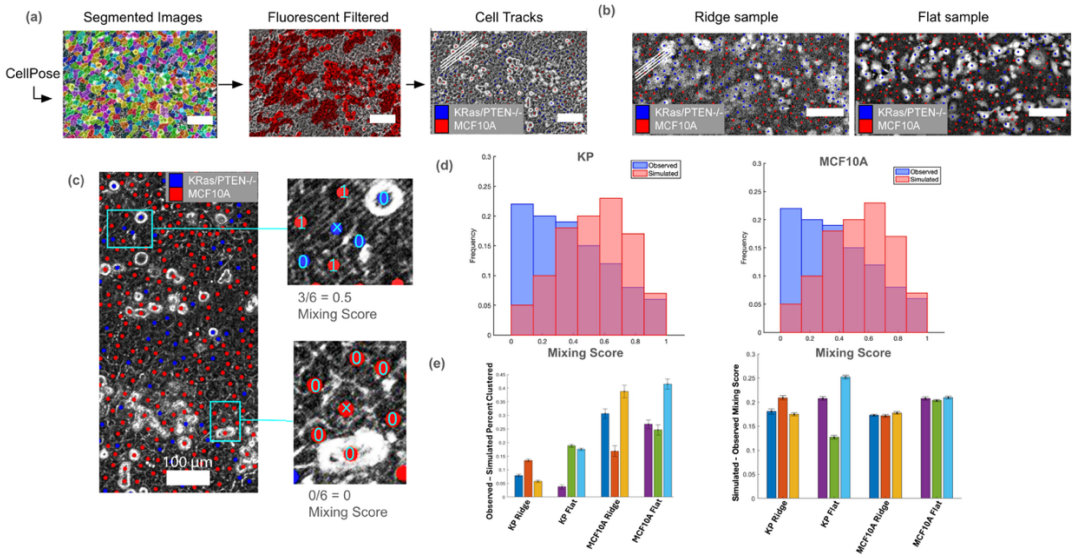


Figure 3.2: Nanoridges has minimal impact on cell mixing (a) Representative images from the analysis workflow. Individual cells are segmented using CellPose, cell types are distinguished via fluorescent labeling, and tracks are generated to follow individual cells. (b) Representative fluorescence images of mixed cultures on ridged and flat substrates, with KP cell centroids shown in blue and 10A cell centroids shown in red. (c) Representative example of computing the local mixing score. For each cell, the fraction of neighbors of the opposite type is calculated and normalized by the expected random mixing level. The zoom-ins show two representative cells with mixing scores of (top) 0.5 and (bottom) 0. The scores are based on the six nearest neighbors. (d) Histograms of mixing scores for KP and 10A cells on ridged and flat surfaces, compared to the distribution expected for ideal mixing. (e) Quantification of deviations from perfect mixing. The bar graphs show the absolute difference between the observed and ideal (left) clustering and (right) mixing scores for each condition.

To quantify cell mixing, we evaluated the identities of the neighbors surrounding each cell. For every cell at each timepoint, we identified the nearest neighbors by dilating the centroid location with a fixed-radius circular mask that was tuned to approximate the typical cell spacing. All segmented cells with areas that overlapped with this mask were considered to be neighbors. With the aid of fluorescence-based cell-type assignments, we then computed the mixing score, which is defined as the fraction of neighbors that are of the opposite type (Fig. 3.2c). A mixing score of 0 indicates that all neighbors are of the same type, and a mixing score of 1 means that all neighbors are of the opposite type. In a perfectly mixed population with equal proportions of both cell types, the expected average mixing score would be approximately 0.5, with the exact value depending on the sizes and shapes of the two types of cells.

Because the cell-type ratio can vary from frame to frame, we generated a baseline expectation by simulating ideal mixing. For each frame, we randomly assigned cell types based on the observed proportions and spatial positions, and recomputed the mixing scores using the same method. This ideal distribution served as a ground truth for local mixing. We compared the distributions of mixing scores for the real and ideal cases to assess deviations from ideal mixing (Fig. 3.2d). In the example shown, both KP and 10A cells exhibit a bias toward lower mixing scores relative to the ideal case, suggesting that cells tend to be surrounded by neighbors of the same type more often than expected by chance. This situation reflects a degree of local segregation or clustering within the monolayers, even though the cells have shared migration directions and speeds. To quantify clustering further, we calculated the fraction of cells

with zero opposite-type neighbors, i.e. those that are fully surrounded by cells of the same type, and compared this fraction between observed and ideal cases (Fig. 3.2e, left). In all cases, we found that the monolayers contained more fully clustered cells than expected under ideal mixing. The 10A cells exhibited higher levels of clustering than did the KP cells on both types of substrates. Although there are some differences in clustering between the flat and ridge surfaces, the effect of nanotopography on clustering is modest.

We also examined the difference in average mixing scores between observed and ideal data (Fig. 3.2e, right). Consistent with the clustering results, both KP and 10A cells show lower average mixing values in the experimentally than in the ideal. This observation further supports the conclusion that cells tend to be surrounded by same-type neighbors more often than expected by chance. The difference in mixing scores is comparable on ridges and flat substrates, with some variability between experiments, suggesting that nanoridges do not alter the overall degree of local cell mixing substantially.

3.3.2 KP Cells Elongate on Ridges While 10A Shapes Stay Constant

We further explored how nanoridges alter cell shapes within mixed populations. We extracted the 2D boundaries of individual cells and converted boundary into a 1D radial distance array, measuring the distance from the centroid to the boundary along the cell's major axis (Fig. 3.3a). These 1D shape profiles were then analyzed using PCA to identify the dominant shape-variation modes.

The first five principal components (PCs), each representing a distinct morphological feature, are ranked in Fig. 3b. The first mode (PC1), cell elongation,

accounts for the majority of the variance (~80%), as illustrated by the example in Fig. 3.3c (inset). Subsequent modes, such as PC2 and PC3, which contribute 5.2% and 4.9% to the variance respectively, describe morphologies characterized by three peaks and three valleys; these shapes are associated with turning events. Collectively, the first three PCs account for over 90% of the total shape variance, allowing us to reduce dimensionality while preserving key shape differences.

We next projected all of the cells studied onto these shape modes and compared the resulting distributions of coefficients for these modes (Fig. 3.3c). For PC1, the distribution for KP cells on nanoridges is skewed substantially to the right as compared to the distribution on a flat surface, indicating that nanoridges cause a substantial elongation of the cells. The PC1 distribution for 10A cells on both flat and nanoridged substrates is similar to that of KP cells on a flat substrate. Thus, nanoridges enhance elongation in the metastatic KP cells, but not in 10A cells. No consistent differences were observed in higher-order modes, such as PC3 or PC5, indicating that nanoridges predominantly influence elongation as opposed to more complex shape deformations.

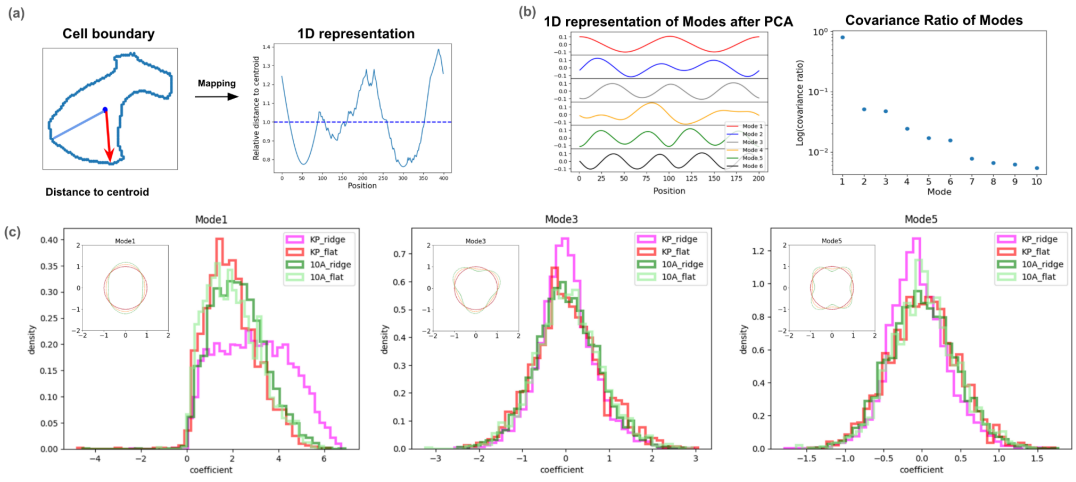


Figure 3.3: Nanoridges induce cell-type-specific shape changes: (a) Schematic of our shape-encoding procedure. Each cell boundary is converted into a 1D array by sampling the boundary at uniform angles and expressing the distance to the cell centroid in terms of its normalized difference from the mean distance. (b) 1D shape representations extracted from PCA. Left: 1D representations of the most dominant PCA modes. Right: The covariance ratio for the ten most dominant modes, plotted on a logarithmic scale. (c) Distributions of projection coefficients for selected modes 1, 3, and 5 for KP and 10A cells on flat and nanoridged substrates. The insets show each mode added to a circular base shape, visualized at constant coefficients (red = 0, orange = 0.5, green = 1). These shape modes highlight cell-type and substrate-specific trends in shape deformation.

3.3.3 Nanoridges Drive Faster and More Directed Migration

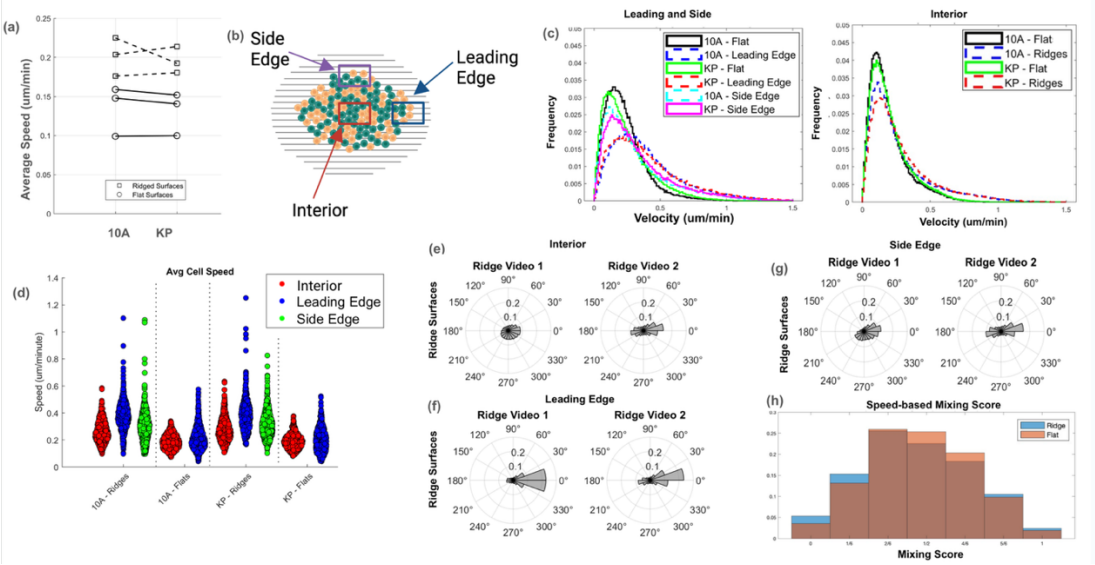


Figure 3.4: Nanoridges guide collective cell motion. (a) Average velocity of 10A and KP cell mixtures on flat and ridged surfaces, averaged across experiments

(n=5 for flats, n=10 for ridges). (b) Schematic illustrating regions labeled as leading edge, side edge, and interior. (c) Velocity distributions of cells across conditions, separated by position (left: leading/side edge; right: interior). (d) Violin plots showing per-cell average speed distributions across regions and conditions. (e–g) Angular histograms of cell motion direction for interior (e), leading edge (f), and side edge (g) cells in ridge experiments, showing alignment along the ridge axis. (h) Histogram of speed-based mixing scores (per cell per timepoint), comparing ridge (blue) and flat (orange) surfaces. The score reflects local dynamic heterogeneity: a value of 0 indicates all six neighbors have similar speeds, while 1 indicates all neighbors differ in speed. Ridge samples show broader distributions, suggesting more dynamic local environments.

We also examined how nanoridges influence collective cell dynamics within mixed sheets. Although 10A and KP cells have distinct migration speeds in monocultures, their velocities converge upon mixing in the same monolayer (Fig. 3.4a). In all of the experiments reported here, nanoridges increased the overall migration speed of the cell mixtures relative to that on flat surfaces, suggesting that the speed increase is primarily driven by nanotopographical cues rather than by the intrinsic differences between 10A and KP cells.

To investigate whether the local cell density influences the migration speed, we compared the velocity distributions in boundary and interior regions of the monolayers. At the boundaries, where cells encounter less physical confinement, both 10A and KP cells moved faster on nanoridges than on flat surfaces. The velocity distributions on

ridged surfaces exhibited longer tails, reflecting more frequent high-speed events (Fig. 3.4c, left). In contrast, the interior regions exhibited reduced velocities overall, which is consistent with the higher cell density and spatial restriction (Fig. 3.4c, right). The speed difference between ridged and flat surfaces is also attenuated in the interior of cell sheets. Direct comparison of average velocities confirms that cells in the interior of sheets consistently migrate more slowly than those at the edges of the sheets, and that ridged substrates promote higher speeds regardless of location (Fig. 3.4d).

Beyond enhancing speed, nanoridges also provide directional guidance. At the leading edge, where the sheet boundary is perpendicular to the ridge orientation, cells preferentially migrated into free space along the ridge axis. Angular histograms of cell trajectories reveal strong alignment with the nanoridges, with a prominent peak near 0°, indicating directed motion into the open area (Fig. 3.4f). In contrast, trajectories on flat substrates were more broadly distributed, and lacked a consistent orientation cue. Similar, though weaker, guidance was also observed in the cell interior (Fig. 3.4e), where trajectories on ridged surfaces showed modest alignment along 0° and 180° compared to the flatter distribution on flat substrates. Even in the side regions, cells on ridges tended toward aligned motion (Fig. 3.4g), although the effect was more variable.

Finally, we quantified local dynamic heterogeneity using a speed-based mixing score, which captures how different each cell's speed is from those of its immediate neighbors. A score of 0 indicates full local homogeneity, whereas a score of 1 represents maximal local speed variation. Cells on ridged substrates exhibited broader mixing-score distributions than did those on flat surfaces (Fig. 3.4h), indicating the local environment during cell migration is heterogeneous and dynamic.

3.3.4 Clonal Identity Overrides Topographic Cues in Cell Mixing

To assess local cell rearrangement within the migrating sheets, we computed D^2_{min} values for individual cells based on their motion relative to neighboring cells, using the same method as described in [31]. This metric captures how much a cell's movement deviates from that of a neighboring group, with higher values indicating more localized rearrangements (Fig. 3.5a). We compared D^2_{min} values for three regions within the sheets: the leading edge, the side, and the interior.

As shown in Fig. 3.5b, the D^2_{min} values were generally higher at the sheet edges than in the interior, suggesting that there is increased local motion and rearrangement near the boundaries. This trend was observed for both cell lines and substrate conditions. However, within each region, the differences between flat and ridged surfaces were minimal. This fact is also reflected in the cumulative distributions of D^2_{min} values, for which the plots for ridged and flat substrates nearly overlap (Figs. 3.5c–d), particularly in the interior. These results suggest that although nanoridges influence overall speed and directional guidance (Fig. 3.4), nanoridges do not strongly affect the local rearrangement of individual cells in a sheet.

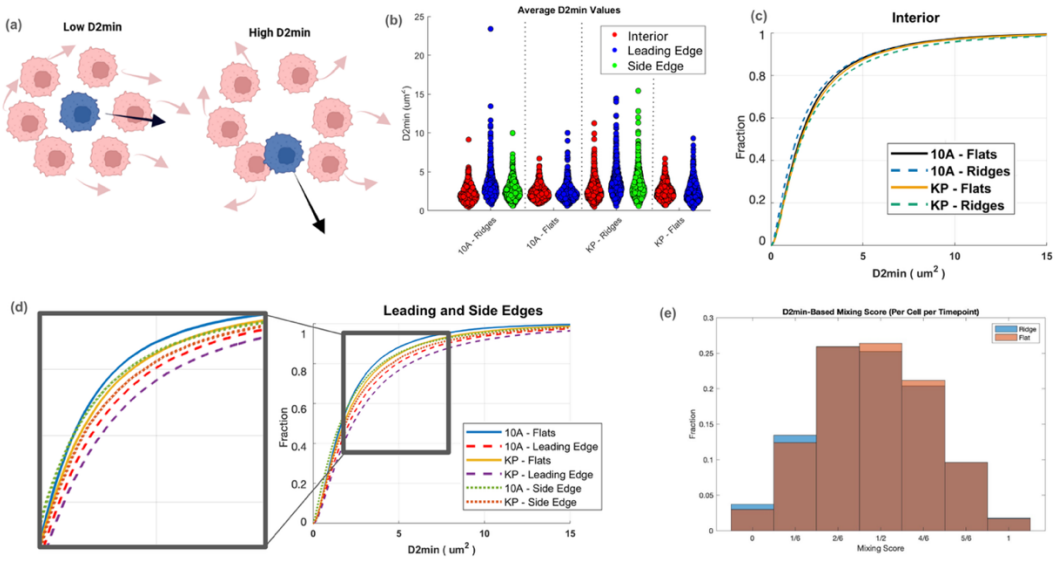


Figure 3.5: D^2_{min} reveals the spatial variation in local cell rearrangements. (a) Schematic illustrating low versus high D^2_{min} values. Low values indicate collective local motion, whereas high values reflect local rearrangement. (b) Swarm plots showing the average D^2_{min} values for individual cells across three spatial regions: leading edge (blue), side edge (green), and interior (red), across mixtures of 10A and KP cells on both flat and ridged substrates. (c) Cumulative distribution plots of D^2_{min} in the interior show similar distributions across all conditions, suggesting minimal effect of substrate or cell type within the mixture. (d) Cumulative distributions for cells at the leading and side edges reveal slightly broader distributions compared to interior, indicating more local rearrangement near the sheet boundaries. No significant substrate-induced differences were observed. (e) Histogram of D^2_{min} based mixing scores (per cell per timepoint) comparing flat and ridge surfaces. Both conditions show similar distributions, indicating that local rearrangement does not significantly affect mixing across substrates.

To explore whether local rearrangement is associated with mixing behavior, we computed a D^2_{min} based mixing score by comparing D^2_{min} similarity for neighboring cells. The resulting distributions (Fig. 3.5e) showed substantial overlap for both cell lines , with no clear separation between ridged and flat substrates. This observation indicates that the degree of local rearrangement is not a strong predictor of neighbor-type mixing and is not significantly influenced by nanoridges.

3.4 Discussion

3.4.1 Nanotopography Enhances Migration but Not Mixing

In this study, we developed a co-culture model that enables the analysis, with single-cell resolution, of how physical topography influences the spatial organization and collective dynamics of healthy (10A) and metastatic (KP) breast epithelial cells. Using AI-based Cellpose segmentation and automated tracking, we extracted cell positions, velocities, and shapes within dense monolayers cultured on flat and nanoridged substrates.

Nanoridges significantly altered the collective migration of the sheets. Ridged substrates enhanced the migration speed compared to that on flat surfaces, especially at the leading edge, and biased the movement direction along the ridge axis (Fig. 3.4). This directional guidance was evident for both cell types and was most prominent in regions where cells had more room to migrate, such as at the leading edge of a cell sheet. In contrast, the cell speed in the interior of a cell sheet was more constrained by density and showed a weaker response to the nanoridges. These results suggest that

nanoridges reinforce directional migration in regions with lower crowding but have limited influence in denser areas of the sheet.

We then explored whether nanoridges modulate how the two cell types mix. We computed mixing indices based on both neighbor identity and speed similarity. In all experiments performed, the cells remained more clustered with their own kind than expected from an ideally mixed control on both ridged and flat surfaces (Figs. 3.3, 3.4h, and 3.5e). There was no significant substrate-induced difference in mixing-score distributions, suggesting that surface cues explored here do not overcome the cell-type-dependent adhesive preferences in these dense sheets.

3.4.2 Cell Rearrangement and Shape Responses Depend on Cell Type

To probe the local deformation and rearrangement within the cell sheets, we measured D^2_{min}, a metric that quantifies non-affine motion of individual cells relative to that of their neighbors. D^2_{min} values were consistently higher at the sheet edges than in the interior, reflecting increased local rearrangement in less crowded regions (Fig. 3.5b–d). However, within each region, the D^2_{min} distributions were largely overlapping for cells on ridged and flat surfaces. These observations support the idea that cell-type-specific interactions dominate local rearrangement patterns, and that nanoridges do not significantly enhance mixing even when local motion is enhanced.

We also analyzed how nanoridges affected cell shape. Principal component analysis of cell boundaries revealed that KP cells became more elongated on ridged surfaces compared to flat ones, while 10A cells maintained similar shapes across both conditions (Figure 3.2). This suggests that metastatic cells are more mechanically

responsive to external cues, while healthy epithelial cells are less sensitive to changes in topography. Several mechanisms could underlie this difference. One hypothesis is that tumor cells are mechanically softer, allowing them to deform more readily under topographic constraints. This is consistent with previous studies showing that cancer cells often have reduced cortical stiffness compared to healthy counterparts, a property that facilitates invasion and elongation under mechanical stress [95, 96]. A second hypothesis is that KRas activation and PTEN loss alter cytoskeletal dynamics, promoting actin remodeling and polarity cues that favor elongated morphologies [97, 98]. Lastly, reduced cadherin-related adhesion in tumor cells may decrease lateral constraints, enabling cells to stretch along the axis of migration [99]. These hypotheses could be directly tested by combining mechanical measurements, cytoskeletal imaging or pharmacological perturbations, and adhesion alteration to determine which mechanisms drive the elongation phenotype of KP cells.

3.4.3 Co-culture Modulates Individual Behavior but Not Identity

Interestingly, in co-culture, differences in motility observed in monoculture were reduced. Previous studies have shown that KP cells exhibit more erratic motion and lower directionality than 10A cells when cultured alone [31], but these differences were diminished in the mixed sheets. Both clones responded similarly to ridge-induced guidance, suggesting that dense intercellular coupling can suppress intrinsic motility differences and align cell behavior within the tissue context.

In summary, nanoridges influence the migration dynamics of cell sheets by enhancing speed and directionality, particularly at the leading edge. However, the

impact of nanoridges on spatial organization is limited, as mixing between healthy and metastatic cells remains low and unaffected by topography. D^2_{min} measurements confirm that local rearrangement is more pronounced at edges but not substantially modulated by surface cues. Overall, these results support the idea that although physical cues can shape collective motion, intrinsic cell–cell interactions play a dominant role in maintaining spatial segregation between cell types. This work highlights the importance of considering both environmental guidance and cellular identity when studying collective migration in mixed tissues.

This study establishes a model for probing how physical topography influences collective behavior in mixed epithelial cell sheets. Although nanoridged surfaces enhanced migration speed and directional guidance, nanoridges did not affect the degree of mixing between healthy and metastatic cells. Both 10A and KP cels responded similarly to nanoridges in co-culture, and the stronger elongation observed in the metastatic cells suggests a higher mechanical sensitivity. Overall, these findings highlight that althpogh physical cues modulate collective motion, cell-type-specific adhesion governs spatial organization within epithelial mixtures.

3.5 Materials and Methods

3.5.1 Surfaces with Ridges

Nanopatterned surfaces were prepared as described previously [100]. Briefly, the base structure was fabricated using Multiphoton Absorption Polymerization. To create the original surface, a droplet of resin, composed of 49 wt% tris (2-hydroxyethyl)

isocyanurate triacrylate (SR368, Sartomer), 49 wt% dipentaerythritol pentaacrylate (SR399, Sartomer), and 2 wt% Lucirin TPO-L (Ciba), was applied to an acrylate functionalized surface. Nanoridges were patterned using a Ti:sapphire laser (800 nm, 200 fs pulses), and unpolymerized resin was removed with N, N-dimethylformamide and ethanol.

To create a mold, hard PDMS was spin-coated onto the patterned master and cured at 60 °C. A 5 mm-thick support layer of soft PDMS (Sylgard 184, 10:1 base to curing agent) was then poured onto the hard PDMS and cured at 60°C for 1 hour. After curing, the composite mold consisting of a rigid surface layer supported by soft PDMS was peeled off. This mold was used to replicate the nanoridge structures by placing a droplet of resin between an acrylate-functionalized coverslip and the composite mold, followed by UV curing for 5 minutes before demolding.

Replicated ridge surfaces were soaked in 100% ethanol for 1 hour to remove any residual non-adherent PCL. Bottom glasses in 6-well glass-bottom plates were carefully removed and replaced with coverslips carrying the ridge structures, which were glued into place. After the glue dried, 2 mL of distilled water was added to each well for a 1-hour soak, which helped remove residual chemicals and served to test the glue seal. Following this, water was aspirated, and wells were allowed to dry. Each well was then coated with 3.25 μg/cm² collagen IV to facilitate cell adhesion. Coating was performed by adding 500 μL of collagen IV solution prepared in dilute hydrochloric acid (HCl) to each well and incubating the plate on ice for 1 hour. After incubation, wells were rinsed twice with distilled water to remove residual acid and unbound collagen.

Two ridge spacings were available for this study: 1.6 μm and 3.2 μm, with ridge diameters of approximately 700nm. We selected the 3.2 μm spacing for this work because prior work demonstrated that this geometry more effectively promotes epithelial cell migration.

3.5.2 Time-lapse Microscopy

MCF10A human breast epithelial cell line (ATCC), MCF10A PTEN$^{-/-}$ [101], MCF10A KRas(G12V) [70], and MCF10A KRas(G12V)/PTEN$^{-/-}$ [70] were gifts from the laboratory of Stuart S. Martin at the University of Maryland School of Medicine, Baltimore. All four cell lines were cultured in DMEM/F12 medium with 5% horse serum (both ThermoFisher Scientific), 10 μg/ml insulin (ThermoFisher Scientific), 20 ng/ml EGF (Peprotech, Rocky Hill, NJ), 0.5 μg/ml hydrocortisone, and 100 ng/ml cholera toxin (both Sigma, St. Louis, MO) supplemented. The laboratory of Stuart S. Martin transduced all the MCF10A cells used in this study with a LifeAct-GFP expressing lentivirus. The MCF10A medium was supplemented with 0.5 μg/ml puromycin (AG Scientific, San Diego, CA) for LifeAct GFP selection. All the cells were incubated in a humidified atmosphere at 37°C and 5% CO2 and passaged every 3-4 days.

For mixing experiments, each cell lines were labeled with 5 μM Cell Tracker Orange or Cell Tracker Red (both from ThermoFisher Scientific) to help identify different types after mixing. Two cell lines labeled with different dyes were mixed in a 1:1 ratio, and a 5 μL droplet of the mixed suspension (1.5×10^6 cells/mL) was plated in the center of each well. Cells were allowed to adhere for 1 hour to the collaged IV-

coated surfaces, while 10 μL droplets of dPBS were added to the edges of each well to prevent evaporation in the 37°C incubator. After rinsing off unattached cells twice, confluent epithelial sheets were achieved. On flat-bottom wells, circular monolayers developed, whereas on ridge-patterned substrates, cell sheets adopted an elliptical shape with their major axes aligned to the ridges. After adhesion, 2 mL of MCF10A medium was added to each well, and the sheets were incubated at 37°C overnight prior to imaging.

3.5.3 Time-lapse Microscopy

Cells were imaged every 3 minutes for 18 hours using a 10× phase-contrast objective (Nikon CFl Plan Fluor, NA 0.3) on a PerkinElmer Ultra-View VoX spinning-disk confocal microscope. The setup included a Tokai Hit incubator chamber set to 37°C and 5% CO_2 and a motorized stage for acquiring multiple positions over time. Images were acquired using a Hamamatsu C10600-10B ORCA-R2 camera (12-bit images 1024 pixels × 1344 pixels, 0.582 μm/pixel) using PerkinElmer's Volocity software (version 6.4.0). Cell sheet dynamics were recorded in both confocal fluorescence and bright-field modes.

Although all the cell lines expressed green LifeAct-GFP, their fluorescence signals were too weak to be visualized under the 10x objective. The same limitation applied to CellTracker Green. In contrast, CellTracker Orange produced a strong red signal in fluorescence images. For each well, multiple regions of interest were imaged, specifically at the edge and center of the cell sheet, to capture the spatial diversity in migration dynamics.

3.5.4 Image Analysis and Mixing Analysis

Time-lapse images were first processed in Fiji using the Contrast-Limited Adaptive Histogram Equalization (CLAHE) function to improve the contreast of images, then segmented frame by frame using the Cellpose segmentation model [94]. Separate Cellpose models were trained for images acquired on ridge and flat surfaces. For the ridge condition, the model was trained using over 2000 manually selected ROIs of individual cells until segmentation accuracy exceeded 80%. The same model was then applied to flat-surface images and also achieved over 80% accuracy.

Cell division events were treated as the termination of a track for the mother cell and the initiation of new tracks for the daughter cells. This choice reflects the fact that after mitosis, daughter cells often spread with altered morphology and directionality, making them effectively new agents in the system. By treating post-mitotic cells as new entries, we ensured consistency in motion statistics.

Segmented masks were passed to a custom MATLAB pipeline for single-cell tracking and fluorescence-based filtering. Fluorescence filtering was performed using an absolute intensity threshold, determined by the dimmest clearly identifiable fluorescent cell in each video, to account for background variation. Additional filters were applied to remove false positives based on minimum cell area, minimum average speed, and maximum displacement.

After filtering cell tracks based on fluorescence, we quantified local mixing by calculating the fraction of a cell's immediate neighbors (within a fixed radius, 5 μm for our data) that had the opposite fluorescence label. To establish a reference for fully mixed conditions, we simulated randomized mixtures by assigning cell types according

to the observed proportions while keeping spatial positions unchanged. The resulting mixing scores from the experimental data were then directly compared to the simulated ground truth to evaluate deviations from ideal mixing behavior.

3.5.5 Principal Component Analysis (PCA)

While individual cell morphologies are unique, it is possible to summarize shared shape characteristics using dimensionality reduction. Prior studies have used PCA to capture shape variance across cells and demonstrated that cell profiles can be well represented by just a few principal modes derived from various shape representations, such as outlines, binary masks, and distance maps [102]. Among these, three PCA-based representations, PCA(Outline), PCA(Fourier of the Outline), and PCA(Distance) were found to perform well in both shape reconstruction and distinguishing different cell types. Importantly, these methods are robust to the exact number of PCA components used.

Here, the PCA (Distance) method is highlighted because it offers a simple 1D representation instead of a 2D array of points in pixel coordinates. Suppose cell outlines are extracted from binary image masks, with each cell outline represented by a collection of points $(x_i, y_i)_n$ in pixel coordinates, where i refers to the i-th point and n denotes the n-th cell in the dataset. In this work, we focus on the PCA(Distance) method, which converts each 2D cell outline into a 1D vector of distances from the centroid, enabling more compact and standardized input for PCA.

To begin, cell outlines were extracted from binary masks, and each outline was represented as a sequence of (x_i, y_i) points for the n^{th} cell. To ensure consistency, we

reoriented each outline by fitting an ellipse and aligning its major axis with the x-axis. All outlines were then resampled to contain the same number of equally spaced points. The centroid of each cell was computed as: $(\bar{x}, \bar{y}) = (1/N) \sum x_i, (1/N) \sum y_i$. For each point on the outline, the Euclidean distance to the centroid was calculated as: $m_i = ||(x_i - \bar{x}, y_i - \bar{y})||$.

To make shape profiles comparable across cells, the distances were normalized by subtracting and dividing by the mean distance for each cell, yielding a normalized shape vector of fixed length. These vectors were stacked to form an $N \times d$ matrix M, where N is the number of outline points per cell and d is the number of cells.

PCA was performed by singular value decomposition (SVD): $M = U\Sigma V^T$

Here, $U \in \mathbb{R}^{nxn}$ contains the principal directions (orthonormal basis vectors), Σ is a diagonal matrix of singular values, and $V \in \mathbb{R}^{dxd}$ contains the projection coefficients of each cell profile onto the principal components.

This decomposition allows us to reduce high-dimensional shape profiles into a few principal modes, capturing the major axes of morphological variation across cells [103].

Chapter 4: 3D Collective dynamics of immune cells in live animals

This Chapter is based on collaboration with Dr. Thomas Daugbjerg Madsen and Dr. Roberto Weigert from the Center for Cancer Research (CCR) at the National Cancer Institute (NCI). Dr. Madsen led the project and collected all the experimental data in this chapter. Figures 4.1 and 4.2 were provided by Dr. Roberto Weigert and Dr. Thomas Madsen.

The goal of this chapter is to develop and apply a 3D optical flow method to quantify myeloid cell motion as a prognostic tool of lesion fate in a live mouse model of head and neck cancer. Prior studies suggest that early immune activity near lesions might help predict whether a lesion will progress, regress, or remain stable. Using longitudinal two-photon imaging of the 3 by 6 millimeter tongue region, we extract dense 3D motion fields across both short timescales (minutes) and long timescales (24 weeks). From the data, we compute motion metrics including speed, directionality, and clustering of high speed regions. This chapter describes the development of the optical flow pipeline, outlines how motion features are quantified, and examines whether early myeloid dynamics are predictive of lesion progression.

4.1 Overview

Understanding the dynamic behavior of immune cells is crucial for studying the mechanisms of tissue repair, inflammation, and cancer progression. Myeloid cells, including macrophages and monocytes, play diverse roles in these processes. They

contribute to antigen presentation, cytokine secretion, tissue repair, and immune suppression [104, 105]. In lesion areas, these cells often display heterogeneous behaviors, and their movement patterns can reflect the tissue's biological response to damage, infection, or tumor development [106].

To quantify these spatiotemporal behaviors, we developed a computational framework based on 3D optical flow analysis to study the in vivo motion of myeloid cells. Using time-lapse 3D intravital microscopy, we imaged fluorescently labeled myeloid cells in live mouse tongues over time. Traditional cell tracking methods often rely on segmentation and object detection, which can be challenging in dense or morphologically complex tissues. In contrast, optical flow computes dense displacement fields between volumetric frames, providing continuous motion estimates at every voxel [107, 108].

We applied this method to analyze myeloid cell activity within and around lesion areas, which were annotated based on structural features. From the computed optical flow fields, we could then extract motion metrics, including speed and directionality. These metrics revealed dynamic differences across various regions, enabling us to quantify the distinct modes of motion and identify zones of high motility. To explore the functional implications of these motion patterns, we then examined how they correlated with lesion fate, such as progression or regression over time.

This study presents a segmentation-independent approach for quantifying the motion of immune cells in live animals. It enhances our ability to analyze cell behavior in complex environments and provides new insights into the roles of myeloid cells during tumor progression.

4.2 Background

4.2.1 Head and Neck Cancer

Head and neck cancer (HNC) includes cancers in the larynx, throat, lips, mouth, nose, salivary glands, and related structures [109]. Most cases are classified as head and neck squamous cell carcinomas (HNSCC), which originate from the epithelial lining of the upper aerodigestive tract [110]. Globally, HNSCC accounts for more than 600,000 new cases and 350,000 deaths annually, making it a significant public health concern [111].

Major risk factors for HNSCC include tobacco use, alcohol consumption, and infection with high-risk human papillomavirus (HPV), particularly HPV-16 [112]. HPV-positive and HPV-negative HNSCCs differ markedly in their molecular profiles, tumor microenvironments, and clinical outcomes [20, 112]. While HPV-positive tumors often arise in the oropharynx and are more responsive to therapy, HPV-negative tumors, typically linked to tobacco and alcohol, tend to exhibit more aggressive behavior and poorer prognosis [110, 112].

Though there are continuous advances in surgical techniques, radiation therapy, and chemotherapeutic regimens, long-term survival for patients with advanced HNSCC remains limited [113]. In recent years, immunotherapy, particularly immune checkpoint blockade, has emerged as a promising treatment strategy [113, 114]. However, only a subset of patients benefits from these therapies, and this treatment has its limitations [115].

A growing body of research has highlighted the importance of the tumor microenvironment (TME) in modulating disease progression and therapeutic response [39, 116]. The TME in HNSCC is often characterized by immune suppression, dysfunctional antigen presentation, and infiltration by myeloid-derived suppressor cells, tumor-associated macrophages, and regulatory T cells [117]. Understanding the spatial and dynamic behavior of these immune populations, especially in response to therapy or within evolving lesion sites, is critical for developing more effective treatment strategies and predictive biomarkers [118].

4.2.2 3D Intravital Imaging

Intravital microscopy (IVM) is a powerful technique that allows researchers to visualize live cells and tissues in their natural environment. Compared to fixed or in vitro samples, IVM enables dynamic imaging over time, allowing for the direct observation of processes such as immune cell movement, tumor invasion, and cell–cell interactions in living animals [119, 120]. This type of imaging is beneficial for understanding complex biological behaviors that cannot be fully captured in static systems.

With recent advances in multiphoton microscopy, genetically encoded fluorescent reporters, and surgical techniques, it is now possible to perform long-term, high-resolution imaging of internal organs in live mice [121, 122]. Among these approaches, 3D time-lapse (or 4D) imaging provides volumetric data at multiple time points, allowing researchers to study how cells behave and move in three-dimensional space over time [119, 120].

Dr. Roberto Weigert's team at the National Cancer Institute (NCI), NIH, is one of the leading groups in this field. His lab has developed several surgical procedures and imaging protocols to enable stable and repeatable imaging of internal organs, such as the salivary gland, pancreas, and tumors in live animals [121]. By minimizing tissue movement and maintaining animal health, they can image deep tissues for several hours with minimal photodamage [119, 121].

In addition to improving imaging quality, the Weigert lab has also focused on applying these methods to study cancer biology. For example, we have used transgenic mice expressing fluorescently labeled myeloid cells and tumor cells to observe their interactions in real time [119, 123]. These experiments revealed how immune cells respond to tumors, migrate through tissues, and interact with the extracellular matrix [119, 123]. This kind of direct observation has drastically advanced our understanding of the tumor microenvironment.

Furthermore, the group has emphasized the combination of imaging with quantitative analysis. We extract motion and spatial features from the image data to study cell behaviors more systematically. This approach turns imaging into not just a visual tool, but also a way to generate measurable data that can help answer biological questions more precisely.

Building on this foundation, our project uses similar 3D intravital imaging techniques to observe myeloid cell dynamics in lesion-associated tumor regions. We combine this imaging approach with 3D optical flow analysis, aiming to quantify motion patterns of immune cells and link them to lesion progression or resolution.

4.2.3 Importance of Myeloid Cells in Cancer

Myeloid cells are crucial components of the tumor microenvironment, playing multiple roles in cancer development and immune regulation [116]. These cells include monocytes, macrophages, dendritic cells, neutrophils, and myeloid-derived suppressor cells (MDSCs), which can either aid in fighting tumors or support tumor growth, depending on the signals they receive from the environment [105].

Among these populations, tumor-associated macrophages (TAMs) are often the most common immune cells found in solid tumors, including head and neck squamous cell carcinoma (HNSCC) [124]. Most TAMs originate from monocytes that are recruited into tumors and subsequently differentiate in response to local signals, such as cytokines and growth factors [106]. Once inside the tumor, TAMs are divided into diverse activation states based on the microenvironment. In many cases, TAMs are pushed into an immunosuppressive state, where they promote blood vessel formation, support tumor invasion and metastasis, and block anti-tumor T cell activity [118, 124, 125].

In addition to TAMs, myeloid-derived suppressor cells (MDSCs) are another group of immunosuppressive myeloid cells that increase during cancer progression. They inhibit T cell function through several mechanisms, including the production of arginase, nitric oxide, and reactive oxygen species [117]. High levels of MDSCs are associated with poor prognosis and resistance to immunotherapy [126].

Dendritic cells, which usually activate T cells, often become dysfunctional in tumors. In some cases, they lose the ability to present antigens or become tolerant to tumor signals, reducing their ability to stimulate an immune response [127]. Tumor-

associated neutrophils (TAMs) can also alter their behavior in response to the environment, and many studies have demonstrated that they contribute to tumor growth and suppress immunity in later stages [128].

Recent work has shown that the behavior of myeloid cells is not fixed. These cells can change their function and location depending on the tumor stage, therapy, or tissue conditions [129]. For example, macrophages in certain positions or with high mobility are linked to tumor recurrence after treatment, while others that are trapped in fibrotic tissue may contribute to immune exclusion [130, 131].

Due to their diverse roles, myeloid cells are now recognized as both biomarkers and therapeutic targets in cancer. Some strategies aim to block their recruitment or survival, while others try to change their function from pro-tumor to anti-tumor [132]. At the same time, new imaging tools such as intravital microscopy help us observe how these cells move and interact with tumors in real time [123].

Overall, studying the location and behavior of myeloid cells in living tissues can help us better understand how tumors grow and how to design more effective treatments.

4.2.4 Rationale and Hypothesis

Although many studies have focused on the molecular pathways that drive tumor growth, there are still two key questions in our understanding of how tumors start and progress: (1) how healthy cells begin to change at the very early stages of tumor initiation, and (2) how a benign lesion turns into a malignant tumor.

One fundamental aspect of these questions is the immune response. Immune cells are known to both block and favor cancer progression. This depends on the possibility of having different cell populations or cells that have been reprogrammed.

Here we propose that such differences in immune cell state may translate into differences in their motility or their collective behavior.

To address these questions, our lab has developed a unique live animal imaging approach using a carcinogen-induced tongue cancer model in mice. This model allows us to follow the tumor development process as seen in human head and neck cancer, including both morphological and molecular features [123]. It allows us to follow the same lesion over multiple weeks in the same animal and capture transitions throughout different stages, including normal tissue, hyperplasia (an initial expansion of the epithelial layer), dysplasia (abnormal cell structure and organization but are not cancer), and carcinoma (uncontrolled growth and spread of cancerous cells) (Figure 4.1).

Additionally, we use mice that express fluorescent membrane reporters, combined with label-free imaging methods. This setup enables us to visualize multiple components of the tumor microenvironment in live animals, including cancer cells, nearby epithelium, vasculature, immune cells, extracellular matrix, and cytoskeletal dynamics [121, 133-135]. These tools provide detailed spatial and temporal information across different scales, from tissue structure to single-cell behavior.

In this project, we apply 3D optical flow analysis to quantify the motion of myeloid cells around developing lesions over a prolonged imaging period (up to 24 weeks). Optical flow does not require single-cell tracking; instead, it provides a voxel-

level map of how cells collectively move in space and time. This is particularly useful in dense tissues, where cells are difficult to separate.

By applying optical flow to the same region of the tongue over multiple weeks, we are able to analyze how immune cell motion may be related to lesion fate. Our primary hypothesis is that the motion of myeloid cells, including their characteristics of motion, may be a predictor of the immune response and tumor development.

4.3 Analysis and Results

4.3.1 Overview of Imaging and Optical Flow Extraction

To study how myeloid cells behave near lesions over time, we used a longitudinal intravital two-photon imaging setup that allows repeated imaging of the same region in live mice over a period of up to 24 weeks. The experimental workflow is outlined in Figure 4.1, which summarizes the 4NQO-induced carcinogenesis protocol and the timeline of image acquisition. This protocol was developed in the Weigert Lab at NCI/NIH, and Dr. Weigert provided the figure with permission.

We utilized a 4-nitroquinoline 1-oxide (4NQO) carcinogenesis model to induce lesions in the tongue, which progress through various stages, ranging from early hyperplasia to carcinoma. This model closely resembles the pathological features of human head and neck squamous cell carcinoma (HNSCC), making it suitable for studying lesion progression in vivo [123]. To visualize immune cell activities during this process, we used transgenic mice expressing membrane-bound GFP under the LysM promoter (LysM-mGFP), which labels myeloid cells, and a ubiquitous mTomato

membrane marker to outline all cells (Figure 4.2). Additionally, second-harmonic generation (SHG) imaging was used to visualize the extracellular matrix (ECM) without staining. This combination of signals allowed us to monitor myeloid cell behavior, tissue morphology, and ECM remodeling over time.

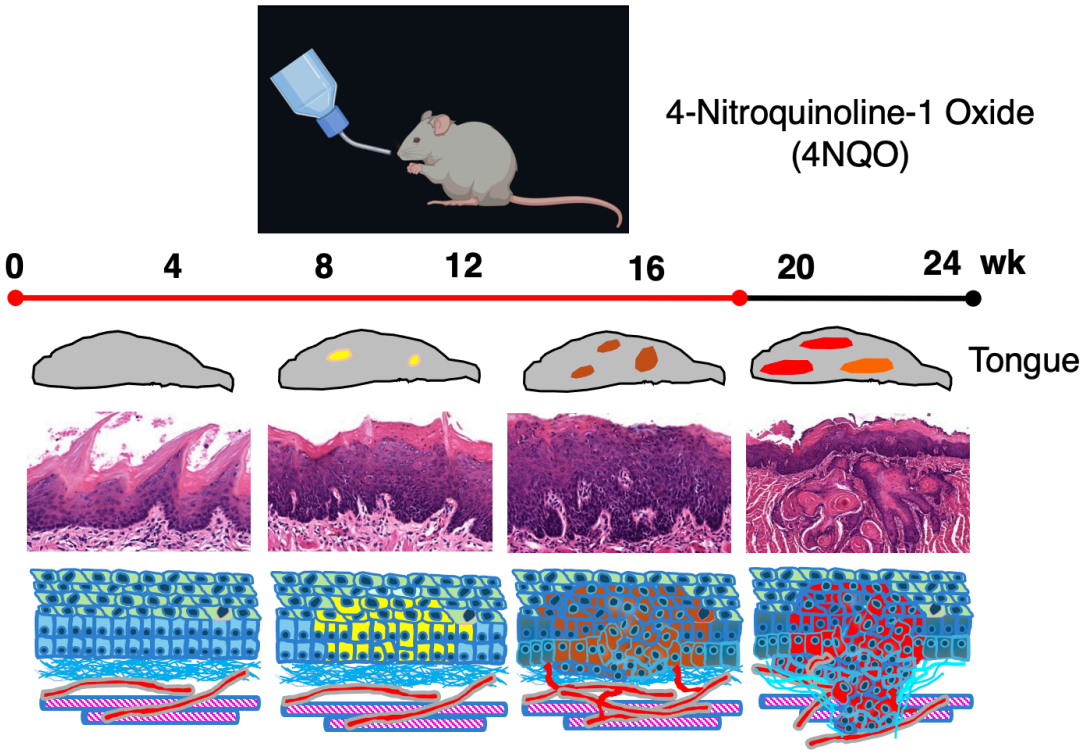


Figure 4.1: Overview of the 4NQO-induced tongue carcinogenesis model. Mice were treated with 4-nitroquinoline-1-oxide (4NQO) through drinking water to induce lesions in the tongue epithelium. The disease progresses through different stages, from hyperplasia and dysplasia to carcinoma, over a 24-week period. Representative H&E histology and schematic illustrations show the morphological and cellular changes over time. Dr. Weigert provides this figure.

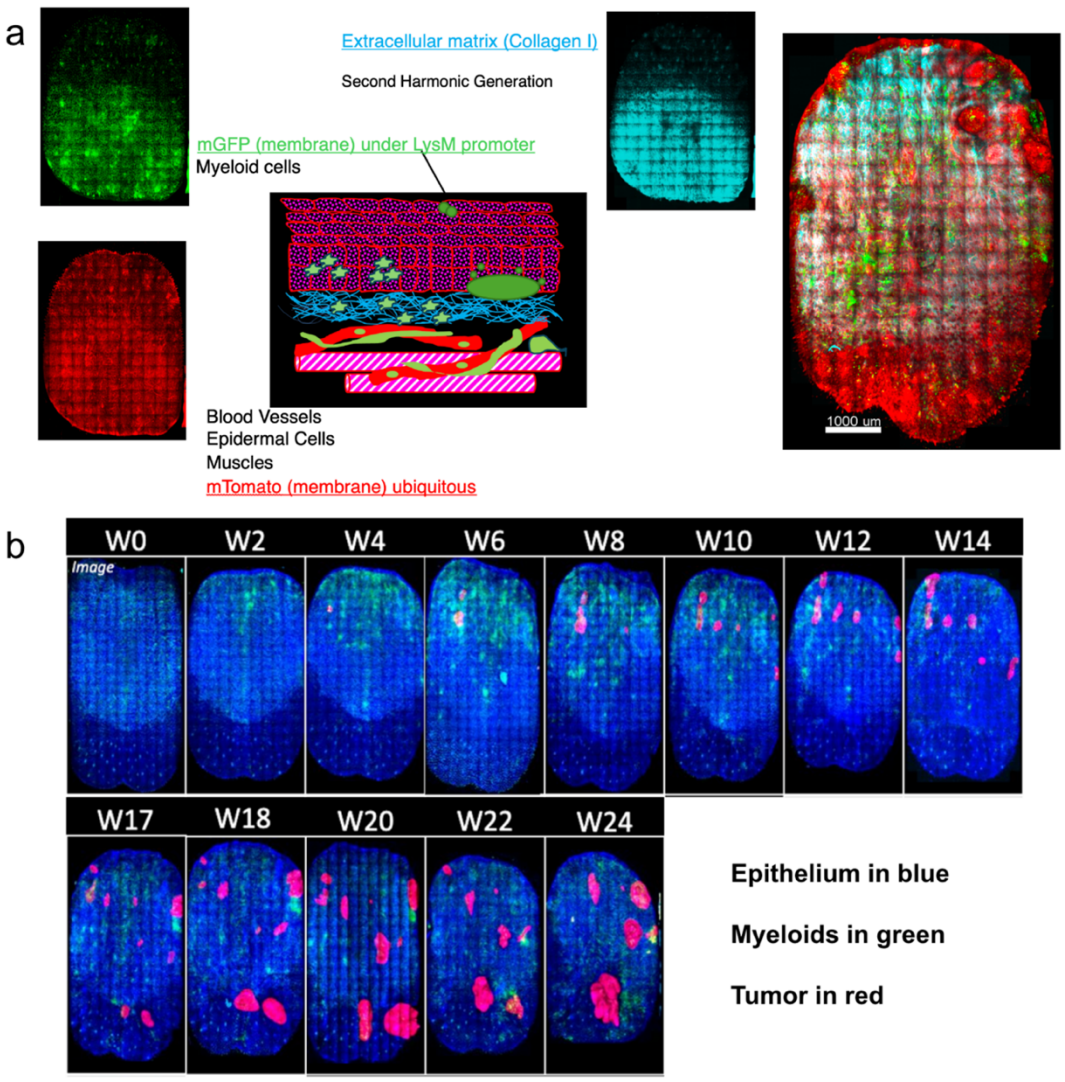


Figure 4.2: Transgenic Mouse Models and the time course of lesion development: (a) Diagram and representative images. The mouse model expresses mGFP (membrane-bound) under the LysM promoter to label myeloid cells (green), and mTomato (membrane-bound) ubiquitously to label all other cell types (red). The extracellular matrix (mainly collagen I) is visualized using second harmonic generation (cyan). The schematic illustrates how these different components are layered in the tissue. (b) Longitudinal 3D imaging from week 0 to 24 shows epithelial tissue (blue), myeloid cell accumulation (green), and lesion emergence

(red). Myeloid cell recruitment precedes visible lesion formation and persists throughout tumor progression. Dr. Weigert and Dr. Madsen provide this figure.

Imaging was performed using two-photon microscopy, which is well-suited for intravital imaging of thick tissues due to its ability to excite fluorophores only at the focal plane using near-infrared light. This approach enables deeper tissue imaging and minimizes photodamage in out-of-focus regions, making it ideal for repeated imaging over extended periods in live animals [136]. In this study, we utilized these features to obtain high-resolution, longitudinal imaging of the tongue, especially the lesion regions, in the same animals over multiple weeks (Figure 4.2).

This imaging and analysis pipeline was designed with the specific goal of exploring an open question in the lab: whether the fate of lesions (progression, regression, or stability) is determined by early-stage dynamics, particularly around week 4 from the administration of the 4NQO. By capturing 3D motion of myeloid cells in the local microenvironment, we aimed to identify features of immune cell behavior, such clustering, or directional migration, that may provide indications of the activity of the cells and correlate with lesion outcomes. The combination of high-resolution imaging and quantitative motion analysis provides a tool to quantify early microenvironmental changes that are otherwise difficult to observe. Figure 4.3 illustrates this approach, showing how regions imaged at early time points can be re-imaged at later time points. Areas where myeloid cells accumulated forming dense cluster were imaged at week 5, in 4D modality. At week 16 the same areas where imaged to determine whether a cancerous lesions formed and the presence of the

cluster. The motion features extracted from the week 5 time-lapse sequences could be used to predict the outcome. This framework provides a way to detect subtle, dynamic changes in the microenvironment that are not evident from morphology alone.

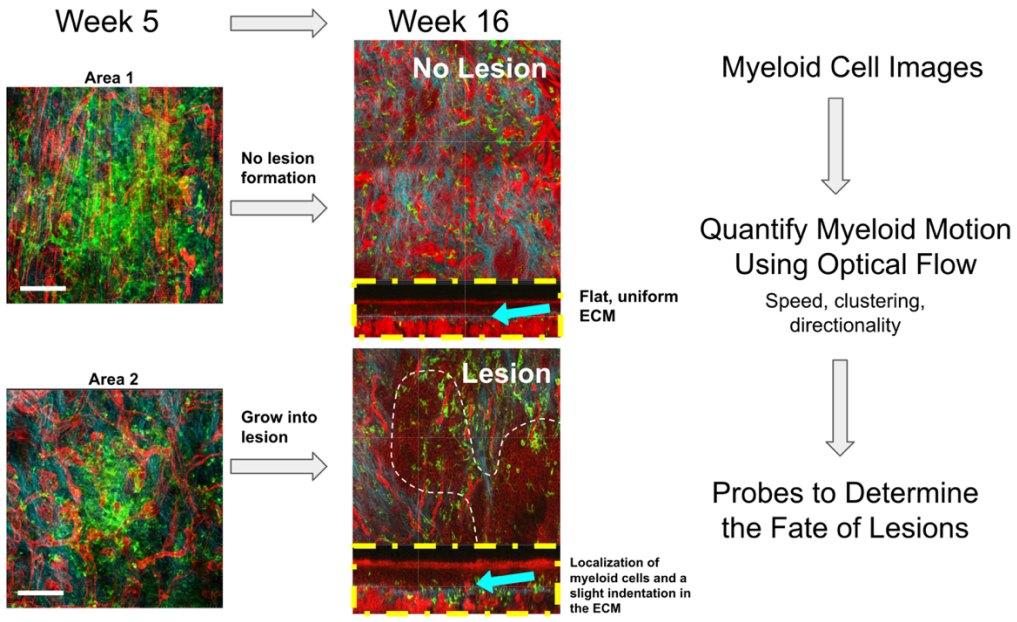


Figure 4.3: Early-stage myeloid cell motion can be used to predict the lesion outcomes. Representative images from two myeloid cluster regions of the mouse tongue are shown. Each row shows a region imaged at week 5 (left), with its corresponding outcome at week 16 (middle). Myeloid cells (green), tissue structures (red), and collagen signals (cyan) are displayed. The top region remained lesion-free, while the bottom developed a visible lesion by week 16. The XZ view at the bottom (in yellow boxes) highlights the differences: flat, uniform ECM for the no lesion area, versus z localization of myeloid cells and a slight indentation in the ECM for lesion. The goal of this chapter (right) is to use 3D optical flow to capture myeloid cell motion at early timepoints and extract features

such as speed, clustering, and directionality. These motion patterns are then used as probes to determine whether a lesion will later progress or regress. Scale bar = 50 μm.

4.3.2 3D Optical Flow Captures Cell Motion in Live Tissues

To quantify myeloid cell motion, we applied a 3D implementation of the Lucas-Kanade optical flow algorithm to the temporally smoothed image volumes. The smoothing step used a five-point kernel across time points centered at each frame, which helped reduce noise while preserving motion dynamics. Optical flow was computed between adjacent smoothed timepoints, generating voxel-level velocity vectors. These flow vectors represent the apparent motion of local image features, particularly myeloid cell clusters. They are helpful in tissue environments where direct tracking of individual cells is not achievable due to high cell density or limitations in resolution. Figure 4.4 shows a representative zoom-in region: the GFP channel (left), in-plane XY velocity vectors overlaid on the GFP image (middle), and a color-coded quiver plot of the same vectors with arrow color indicating Z-direction motion (right). Together, these visualizations demonstrate that our optical flow captures the spatial complexity and 3D nature of myeloid cell dynamics within the tissue.

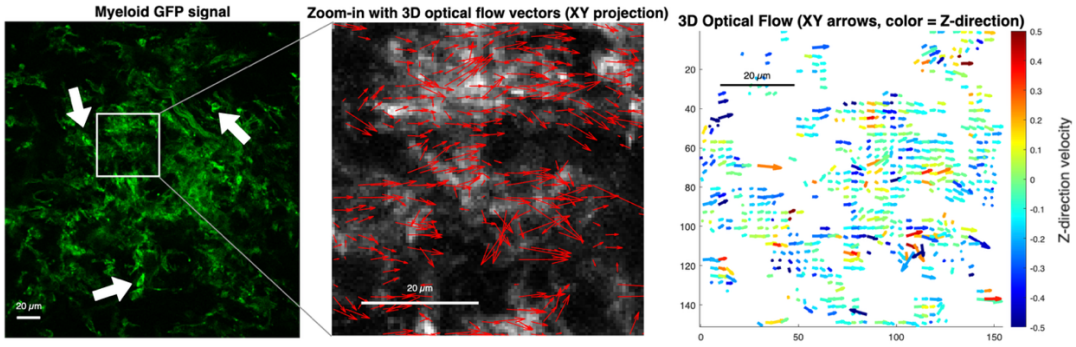


Figure 4.4: 3D optical flow captures myeloid cell dynamics: Left: Myeloid GFP signal of a imaging region (single time, single z slice). Arrowheads point to some sample myeloid cells. Middle: XY optical flow vectors overlaid on the grayscale image of the zoomed in area, visualizing local in-plane motion. Arrows indicate lateral movement between consecutive frames and are scaled up 100 times for visualization purpose. Right: Same region shown without image background, with arrows color-coded by the Z-direction velocity. Blue indicates upward motion (toward lower z), while red suggests downward motion (toward higher z). Arrows are scaled up 50 times. Scale bar = 20 µm.

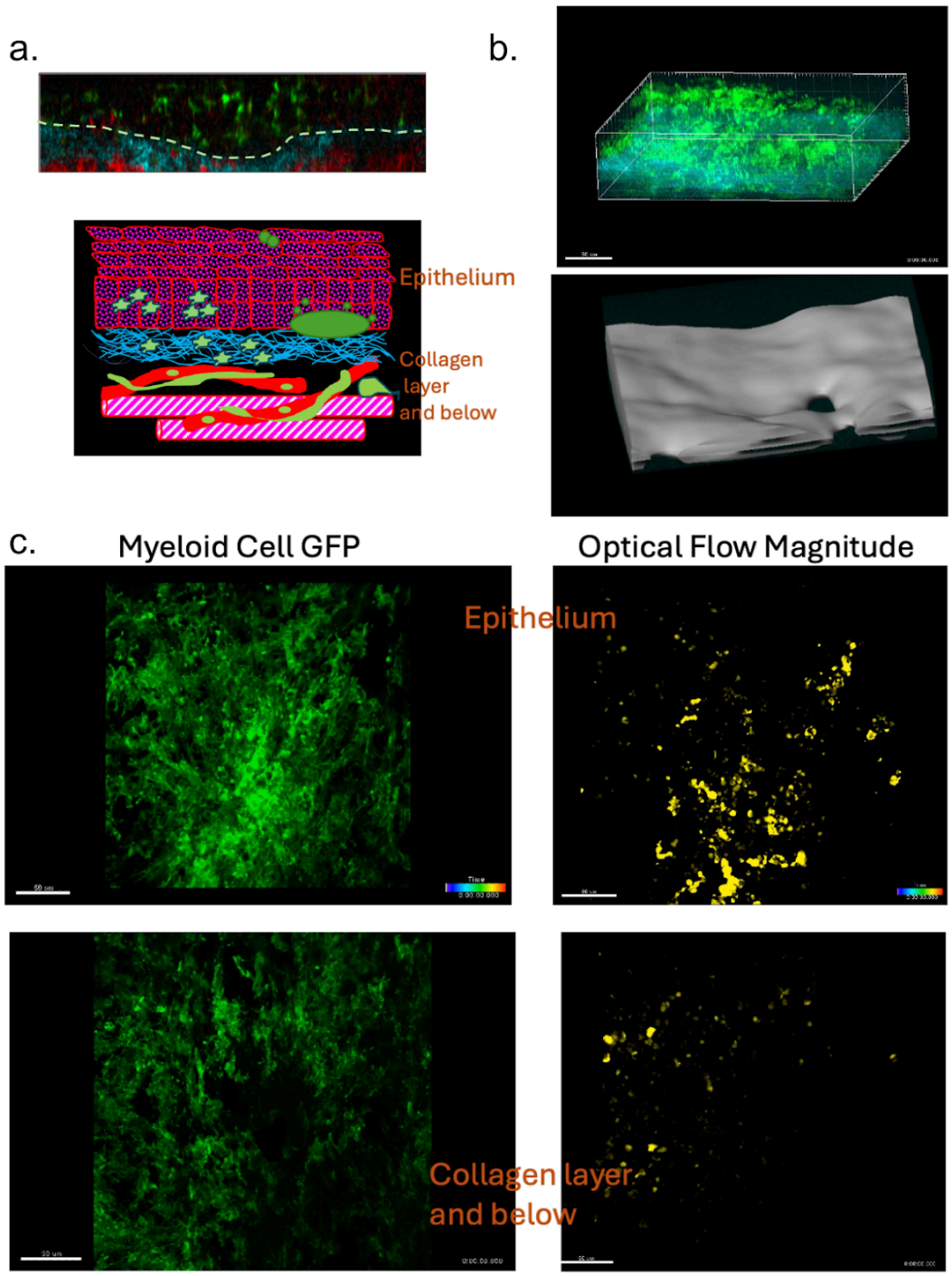


Figure 4.5: Comparison of myeloid cell motion across epithelial and subepithelial tissue layers: (a) top: Cross-sectional (x-z) view showing tissue architecture. GFP-labeled myeloid cells (green) and second harmonic signal (cyan) reveal the

boundary between the epithelium and collagen layer (white dashed line). Bottom: Corresponding cartoon schematic illustrating tissue organization, including epithelial layer, collagen interface, and underlying stroma. (b) top: 3D view of myeloid cells (green) and collagen (cyan) shows distribution across depth. Bottom: Surface reconstruction using collagen signal (cyan) shows structural curvature at the lesion formation site. This surface is used to divide the whole volume into epithelium and collagen layer, and below. (c) Left: Maximum intensity projections of GFP signal and corresponding 3D optical flow magnitude (right) for two regions. The top row corresponds to the epithelial layer, the bottom row to the collagen layer, and below. Motion magnitude is more spatially clustered and elevated in the epithelial region, while cells in deeper layers show lower and more scattered motility. This shows the differences in myeloid cell dynamics. Scale bar = 50 μm.

To better understand how myeloid cell motion is distributed across different tissue regions, we divided the imaging volume into layers based on tissue structure (Figure 4.5). Specifically, we used the second harmonic generation (SHG) signal from collagen to segment each field of view into the epithelial layer that contains the lesion and the deeper collagen-rich region. Lesion areas were segmented based on the presence of a visible indentation in the collagen layer, as seen in the second harmonic generation signal. These structural deformations correspond to the expansion of the basal epithelial layer into the underlying tissue, often accompanied by increased myeloid cell accumulation. We manually annotated these regions in 3D using the

collagen channel in Imaris and used them to define lesion-associated volumes for downstream motion analysis.

Based on this segmentation, we performed optical flow analysis separately within the epithelial part and within the collagen layer and below. This approach enabled us to compare motion behavior in lesion areas with that of the surrounding regions. As shown in Figure 4.5, this comparison highlights the distinct dynamics in different layers. The epithelial layer often displayed more spatially clustered and higher-magnitude flow, suggesting localized myeloid activity near the lesion. In contrast, the collagen-rich regions exhibited slower, more scattered motion. These observations indicate that myeloid cell dynamics are shaped by local tissue architecture and lesion-associated changes in the microenvironment.

In order to further capture regions of particularly elevated myeloid cell activity, we developed a hotspot tracking approach based on local maxima in the magnitude of optical flow. After applying a Gaussian smoothing filter to the 3D flow field, we thresholded the data to identify voxels exceeding a defined motion intensity. These high-magnitude regions were then spatially grouped using connected component labeling, resulting in a set of 3D hotspots at each time point. We tracked these hotspots over time by linking them based on centroid proximity and overlap, allowing us to observe their temporal evolution and persistence. To visualize the results, we generated a series of maximum intensity projections across Z at individual timepoints, allowing us to summarize the spatial distribution and dynamics of high-speed regions in 2D (Figure 4.6).

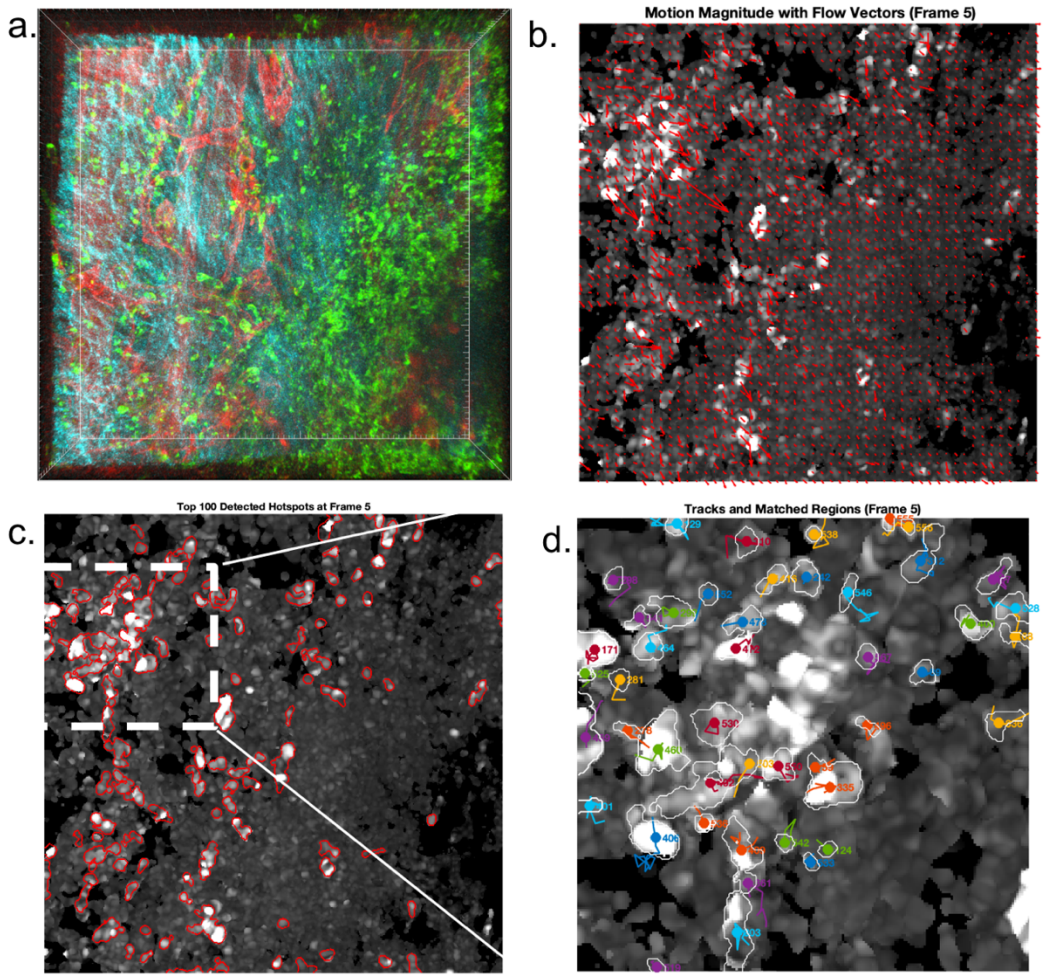


Figure 4.6: Detection and tracking of high-speed myeloid clusters from 3D optical flow (z-projected views): (a) Overview of the imaged region showing a combination of signals: tissue structure (red), myeloid cells (green), and extracellular matrix (cyan). The visualization is a maximum intensity projection across z slices. (b) Optical flow magnitude at frame 5, shown as a Z-max projection in grayscale. The brightness of the white color corresponds to the magnitude of optical flow vectors. Red arrows indicate flow direction and strength, based on the projection of 3D flow vectors onto the XY plane. (c) Hotspot detection highlights the top 100 motion clusters in red at frame 5. The background white signal

corresponds to the magnitude of optical flow vectors. The dashed box indicates the region shown in (d). (d) Zoom-in showing selected tracked hotspots with trajectories (color-coded by track ID) and corresponding hotspot regions outlined in white.

This projection-based visualization helped resolve spatial relationships between hotspots, tissue structure, and flow direction. For example, we overlaid projected optical flow vectors on the motion magnitude field to illustrate local flow orientations. Detected hotspot masks were displayed as red contours overlaid on the flow magnitude projection to highlight spatial clustering. To assess dynamics, we selected a zoomed-in region and plotted XY trajectories of tracked hotspots, color-coded by track ID, with their current positions marked and linked to their corresponding motion regions. All panels shown in Figure 4.6 are Z-projections taken at a representative time point (frame 5), allowing for consistent comparison across imaging channels and analysis outputs. This method enabled us to identify localized bursts of collective myeloid motion and monitor how they travel, shift, or fade with lesion progression. Hotspots were often found at the boundary of lesion regions or near sites of collagen disruption, suggesting that they may reflect focal immune responses or areas of active microenvironmental remodeling.

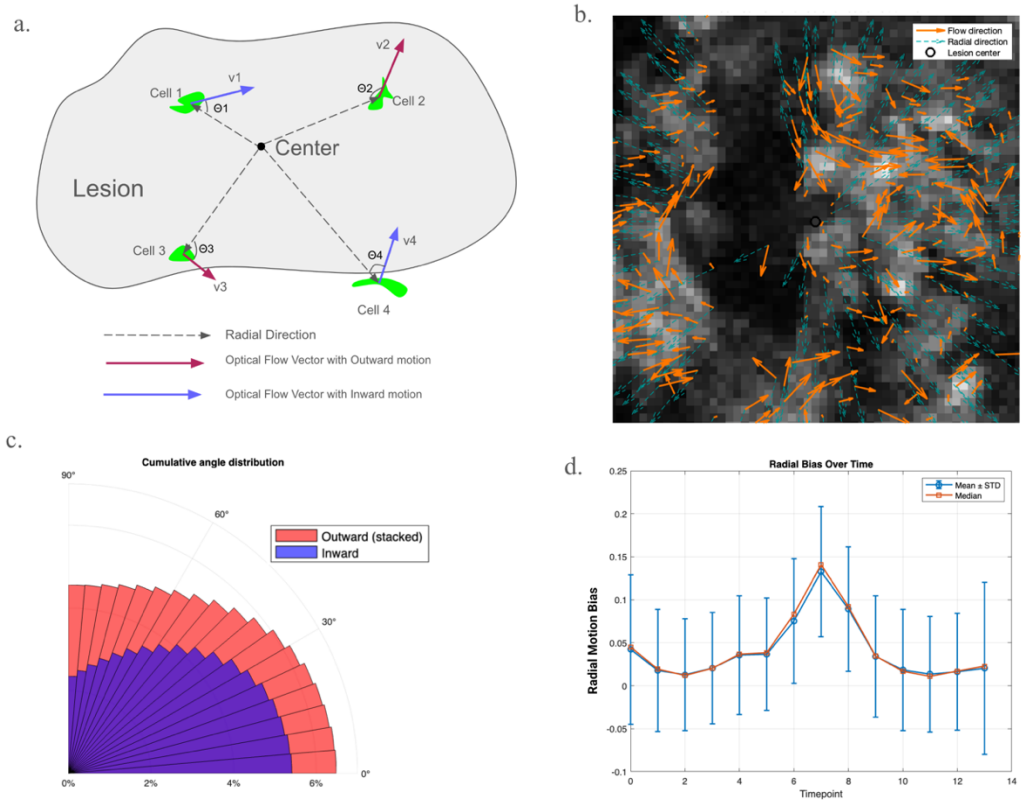


Figure 4.7: Radial motion analysis of myeloid cell dynamics around lesions. (a) Schematic illustrating how radial motion is computed. The angle θ between each voxel-level velocity vector (v) and the radial direction from the lesion center is used to determine motion orientation. Vectors in red are outward, and those in blue inward. (b) Example flow field visualization from one z-slice of a week 5 dataset. Orange arrows represent local optical flow direction, cyan arrows show radial directions from the lesion center (black circle), overlaid on a grayscale image of myeloid signal intensity. (c) Cumulative polar histogram of angular distributions, pooled across timepoints. Inward motion (blue) dominates across most angles, with outward motion (red) stacked on top. (d) Radial motion bias over time, quantified as the average radial component of flow vectors per frame.

A consistent positive bias is observed, suggesting active inward recruitment of myeloid cells during this phase.

To demonstrate the ability of our optical flow pipeline to resolve spatially organized cell motion in live tissues, we developed a radial motion analysis framework (Figure 4.7). This approach quantifies how flow vectors relate to lesion-centered geometry by comparing each voxel-level velocity vector $\vec{v}$ to a radial direction vector $\hat{r}$ pointing toward the lesion center. A dot product between $\vec{v}$ and the unit radial vector $\hat{r}$ yields the signed radial component, which determines whether the motion is directed inward or outward. Using the GFP-labeled myeloid signal, we created maximum intensity projections at early timepoints to help manual selection of lesion centers. These user-defined centers enable radial referencing for all subsequent motion analysis. From the 3D optical flow output, voxel-level velocity vectors (vx,vy,vz) were extracted, and 2D slices were selected for visualization. We overlaid flow vectors onto the original myeloid fluorescence image to illustrate spatial patterns in local motion (Figure 4.7b). To quantify directionality, we computed the radial direction vector from each voxel to the lesion center and classified vectors as inward or outward based on the sign of their radial component. These classified angular values were pooled across time and visualized using stacked polar histograms, normalized by total vector count, to summarize directional bias (Figure 4.7c). In the example shown for a week 5 cluster, we observed an inward bias. We also tracked the radial motion bias over 4 minutes (Figure 4.7d), defined as the mean radial component of motion across all vectors at each timepoint. This metric remained mostly positive, indicating a consistent inward-

directed motion trend, with a pronounced peak at mid-timepoints. Together, these plots highlight our ability to extract detailed, sub-cellular motion dynamics from complex intravital datasets. Further work applying this workflow across all early timepoints may help identify which myeloid clusters are more likely to develop into regression or progressing lesions.

This combined approach of flow quantification, region-based segmentation, and hotspot tracking provided a spatial and temporal view of myeloid cell dynamics during lesion formation and progression.

4.3.3 Spatiotemporal Dynamics of Myeloid Cell Motion in Tumor Microenvironment

Previously, the Weigert lab has found that not all lesions in the 4NQO tongue model progress to a malignant state. While 25% of the lesions progress and continue to grow, others remain relatively stable for extended periods (30%), and some even regress in size (45%). This difference in lesion fate highlights the need to understand the local immune microenvironment that may influence outcomes. In our experiments, we tracked lesions longitudinally and categorized them based on their volume changes over time. Lesions were grouped into three main types: progressing, regressing, and stable. Progressing lesions showed sustained growth, often expanding and displacing surrounding collagen. Regressing lesions shrink in size over time, sometimes becoming undetectable. Stable lesions maintained their general size and structure across the imaging window without significant progression or regression in the late weeks. These

fate types were assigned manually based on 3D visualization and quantification of the collagen channel and myeloid cell images. Representative growth curves for each lesion type are shown in Figure 4.5. In prior experiments, the frequency of each lesion type varied, with non-progressing (regressing and stable) lesions being the most common ones.

To examine how myeloid cell behavior changes around lesions with different fates, we compared the motion dynamics and signal patterns of lesions that progressed, regressed, or remained stable over time. For regressing lesions, we often observed that myeloid cell signals and activity remained present while the lesion was in the growing stage. However, as the lesion began to shrink, myeloid motion within the lesion area became less prominent. Once the lesion regressed substantially or disappeared, the myeloid signal dropped and eventually cleared from that region entirely.

In contrast, progressing lesions typically retained or expanded both their myeloid presence and lesion volume over time. The GFP signal often increased or stayed high, and while motion magnitude varied, many progressing lesions show a dense myeloid population. For stable lesions, both lesion size and myeloid signal remained roughly unchanged throughout the imaging period. Motion activity in these areas was present but steady, without significant increases or reductions. These lesions neither expanded nor shrank, and the surrounding immune environment also appeared stable over time.

Altogether, these observations suggest that regression is associated with both the physical shrinkage of the lesion and a gradual decline in local myeloid cell activity. This might reflect successful resolution of inflammation or clearance of immune-

involved tissue. On the other hand, persistent lesions maintain myeloid presence and often accumulate immune cells. These distinctions in both structural and immune dynamics may reflect fundamentally different tissue states or signaling environments that influence lesion fate.

4.3.4 Motion Behavior May Relate to Lesion Fate

We investigated whether local immune cell motion patterns, particularly those of myeloid cells, are associated with the outcome of a lesion. Previous work in the lab proposed that lesion fate might be determined mainly during early stages, particularly around week 4. With longitudinal imaging, we were able to revisit the same lesion sites over many weeks, allowing us to track changes in cellular behavior and their spatial context across time.

The optical flow framework not only provides qualitative visualizations of myeloid cell activity but also enables quantitative measurements that may inform lesion fate. From the 3D motion fields, we can extract metrics such as overall motion magnitude, radial versus tangential components, and the proportion of inward versus outward motion relative to lesion centers. Moreover, we also deployed hotspot tracking analysis that provided a probe into cellular or sub-cellular motion, providing information on whether those myeloid cells are surveilling or traveling. These behaviors can be tracked over time to identify dynamic signatures associated with lesion progression or regression. These motion-based measurements offer a noninvasive and high-resolution way to characterize the immune microenvironment in situ and could provide early indicators of lesion outcome.

In this experiment, we took images of mice at week 5 and week 16, with the goal of mapping the early stage myeloid activities with the regression or progression outcome of lesions, aiming to find quantitative metrics that may help predict lesion fate based on myeloid cell dynamics observed during the early phase of lesion development. Using the 3D optical flow-based velocity maps, we examined how myeloid cell motion patterns differ across 30 different areas of the tongue occupied by myeloid clusters. After removing one outlier from the non-lesion group, we found that lesion-associated regions had a slightly higher average speed. The mean speed near lesions was 0.28 ± 0.09 μm per minute, compared to 0.24 ± 0.05 μm per minute in regions without lesions (Figure 4.8). This difference was not statistically significant, with a p-value of 0.11; however, it suggests a trend where myeloid cells tend to move faster in areas associated with lesion development. These values were based on local median flow magnitudes averaged across time points.

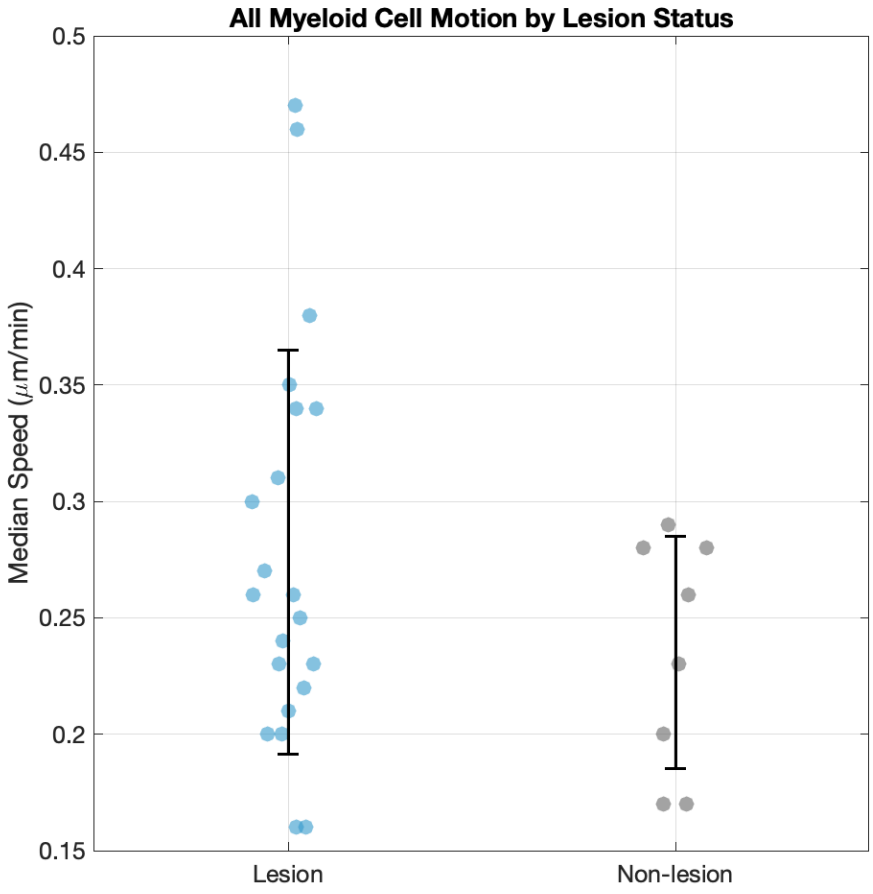


Figure 4.8: Comparison of myeloid cell median speed in lesion-associated versus non-lesion regions across all animals. Each point represents a single region, with random horizontal jitter added for visualization purposes. Regions near lesions show slightly higher speeds on average (0.28 ± 0.09 µm/min) compared to the non-lesion areas (0.24± 0.05 µm/min), though the difference is not statistically significant (p = 0.11). This trend suggests increased immune cell activity near lesion sites.

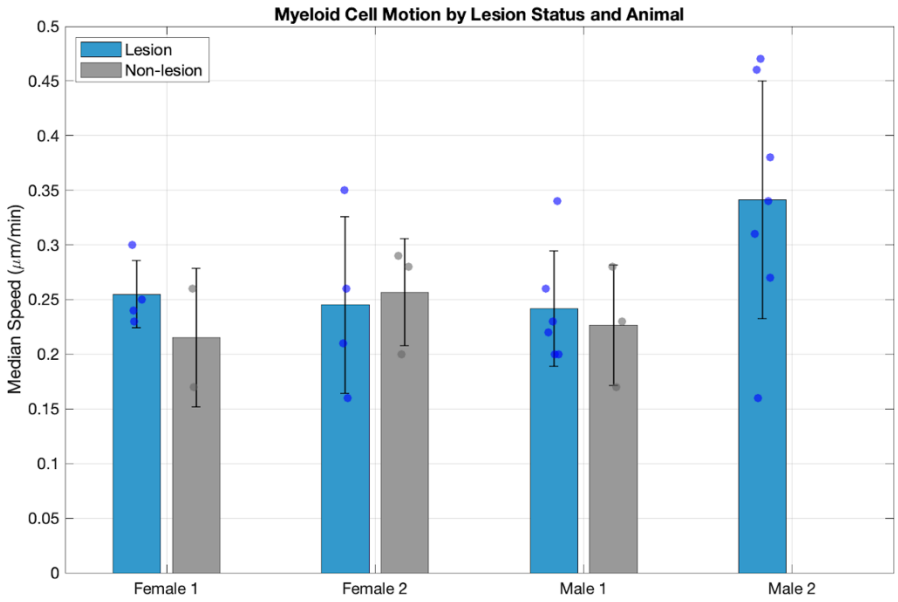


Figure 4.9: Median myeloid cell motion speed in cluster regions that led to lesions vs non-lesions, grouped by individual animals. Each point represents one region.

Examining individual animals revealed some notable differences (Figure 4.9). In particular, Male 2 showed the highest speed near lesions, with an average of 0.34 ± 0.11 µm per minute across seven measurements. The other three animals, which included Female 1, Female 2, and Male 1, had speeds in a narrower range between 0.24 and 0.26 µm per minute. On the non-lesion side, all animals showed lower motion levels. Female 1 had the slowest speed at 0.22 µm per minute, while Female 2 had the highest at 0.26 µm per minute. This consistent difference within each animal supports the idea that motion tends to be higher in regions associated with lesions. Note the observed variability across animals also reflects the underlying heterogeneity in lesion behavior and state. At a given time point, different lesions may represent varying stages of progression or regression, which could contribute to the differences in local dynamics. These results suggest that optical flow–based motion analysis may offer a

noninvasive tool to classify lesions by activity level or biological state. In future work, it may be useful to correlate these motion features with histological scores to better understand how myeloid activity relates to lesion state or fate.

One observation is that most of the regions we imaged eventually developed lesions. This means that the "non-lesion" regions were not permanently lesion-free, but more likely represent earlier or pre-lesion states. As a result, the difference in motion between lesion and non-lesion areas might reflect early microenvironmental changes that occur before a lesion becomes visible.

In summary, while the difference in speed between lesion and non-lesion regions was relatively modest and did not reach statistical significance, it was consistent across animals and fits with the idea that immune cell behavior changes during lesion development. These results support the potential use of motion-based metrics to monitor or even predict lesion progression, especially if combined with other features such as directionality, hotspot density, or persistence over time.

4.4 Discussion

The optical flow framework not only provides qualitative measurements of myeloid cell activity but also enables downstream analysis that might reveal signs that impact lesion fate. From the 3D optical flow fields, we can extract metrics such as motion magnitude, radial versus tangential components, the proportion of inward versus outward motion relative to lesion centers, and tracks of local hotspots of motion that are indicative of different myeloid activities. These parameters can be tracked over

time to identify myeloid dynamic signatures associated with lesion progression or regression. For instance, a sustained inward motion of myeloid cells toward the lesion may reflect recruitment, and the lowered level of motion of myeloid cells might be associated with lesion regression. Such motion-based readouts offer a noninvasive and high-resolution way to characterize the immune microenvironment and could provide early indicators of lesion outcome.

One of the advantages of using optical flow in this work is that it allows for capturing motion in all three spatial dimensions. Many methods only track cells in 2D planes, but in real tissue cells also move in z direction. Measuring z-directional motion is important because it tells whether cells are entering or leaving a lesion. Having quantitative values for motion in x, y, and z also makes the analysis more rigorous and less dependent on visual impressions. These quantitative measurements in 3D allows us to move beyond describing motion patterns and further build a framework that links them to mechanisms and eventually to predictive models.

Looking forward, this motion-based framework could be extended to support lesion fate prediction by leveraging the rich temporal patterns embedded in the optical flow data. The ability to quantify directional biases, hotspot persistence, and local motion magnitude opens the door for future approaches that associate specific motion phenotypes with lesion outcomes. Furthermore, combining this analysis with spatial proteomics, multiplexed immunostaining, or single-cell RNA-seq could provide deeper insight into the molecular programs associated with different motion signatures. Integration with segmentation-based methods may also help distinguish between motion driven by different subtypes of myeloid cells and enable cell-type specific

modeling. As intravital imaging continues to scale in both resolution and duration, the combination of computational motion analysis and longitudinal data will be crucial for identifying early markers of tumor immune interactions.

Translationally, the same principles could be explored in patient contexts. One possible method is to use antibody-based probes with fluorescent or contrast agents, which are already under clinical investigation for visualizing immune cell subsets in vivo. Another option is to use FDA-approved dyes such as acridine orange, which has been safely used to label different organelles and cellular structures. These tools provide sufficient contrast to capture cell density and dynamics in tissues using high-resolution clinical imaging tools. Importantly, the optical flow framework itself is label-free: it requires only sequential images data to compute motion fields. So once appropriate labeling or contrast methods is used, the same motion-based lesion prediction strategy can be translated to human studies and diagnostics.

4.5 Materials and Methods

4.5.1 Animal models and carcinogens

All experiments were approved by the National Cancer Institute (National Institutes of Health, Bethesda, MD, USA) Animal Care and Use Committee and were compliant with all relevant ethical regulations regarding animal research. LysMcre (B6.129P2-Lyz2tm1(cre)Ifo/J) and mT/mG (B6.129(Cg)-Gt(ROSA)26Sortm4(ACTB-tdTomato,-EGFP)Luo/J were purchased from Jackson Laboratory and backcrossed at least 6 generations into C57Bl6/NJ background before

crossed to homozygosity for both gene elements. All mice used in this study were between 8-14 weeks of age at the start of treatment. Mice were anaesthetized by isoflurane inhalation (3%) followed by an initial intraperitoneal injection of a mixture of ketamine (100 mg per kg) and xylazine (20 mg per kg) in lactated Ringer's solution before imaging sessions and maintained as necessary during imaging. Two cohorts of mice were used to generate images for this project, where cohort 1 was imaged biweekly and cohort 2 was only imaged at weeks 5 and 16.

Premalignant lesions and tumors were induced as previously described [123]. In brief, 4-Nitroquinoline 1-oxide was administered at a concentration of 50µg/mL in the drinking water for 16 weeks (week 1-16), followed by a recovery period with regular water for 8 weeks (week 17-24). To maintain weight, the mouse diet was supplemented with a soft transgenic dough-diet (Bio-serv, S3472) once a week starting at the fifth week of treatment.

4.5.2 Imaging Setup and Preprocessing

Two-photon microscopy was performed using an inverted laser-scanning two-photon microscope (MPE-RS; Olympus, Center Valley, PA) equipped with a tunable laser (Insight DSþ; Spectra Physics, Santa Clara, CA). The tongue of the anesthetized animal was gently placed in a 3D-printed tongue holder device (Wang et al. Weigert lab unpublished) with the ventral side facing the objective. The entire ventral area was scanned using an Olympus UPlanSApo IR 30x (numerical aperture, 1.05, Evident) silicone oil objective, and images were acquired using a resonance scanner set to 3 line

repetitions. The most superficial 150μm was acquired in each stack at a 2μm distance between optical slices (z-resolution). Excitation was performed at 900 and 740 nm, and the emitted light was collected by an appropriate set of mirrors and filters on three detectors (bandpass filters: blue for collagen or NADH: Z 410 to 460 nm; green for GFP: Z 495 to 540 nm; and red for TdTomato: Z 575 to 645 nm). The resulting stacks were tiled using the Fluoview software (Evident) after each imaging session. The same imaging setup was used for timelapse imaging, except a 1.5x digital zoom and 6 line repetitions were used for an imaging depth of 72μm (49 optical sections at a z-resolution of 1.5μm per optical slice). 5-10 min of timelapse was acquired at a framerate of 19.4 3D stacks per second.

Raw 4D imaging data (XYZT) with three color channels were first acquired from intravital two-photon microscopy and converted to .ims files using Imaris File Converter. The images were then imported into Imaris to perform layer separation based on collagen signals. We also imported them into MATLAB using Bio-Formats. To ensure consistency across timepoints, rigid drift correction was applied to compensate for possible animal motion. In particular, a custom jitter correction routine was used to align each time point to the preceding one baked on the mTomato fluorescence channel, which labels the tissue membrane. This step ensured pixel level correspondence over time.

4.5.3 3D Optical flow analysis

3D optical flow analysis to quantify tissue-level motion of myeloid cells in the intravital imaging datasets. The input consisted of 3D image stacks collected at regular

time intervals, with 0.57 μm axial step size in x, y, and 1.5 μm in z, and a frame rate of 1 frame per minute.

Optical flow was computed per voxel using Lucas–Kanade method extended to 3D volume [108, 137]. This approach estimates motion by solving for the local displacement vector that minimizes the difference in intensity between two consecutive image volumes within a fixed neighborhood. A 3D Gaussian smoothing kernel was applied to reduce noise sensitivity, and flow vectors were calculated in all three spatial directions (x, y, z).

To minimize the effects of photobleaching and tissue drift, flow estimation was limited to voxels with signal intensities above a specified threshold, and frames exhibiting excessive z-displacement or unstable registration were excluded. The green channel, typically corresponding to genetically labeled myeloid cells, was used for motion estimation after spatial alignment of all channels.

The use of dense optical flow allowed us to assess collective cell behavior without requiring segmentation or single-cell tracking, making it particularly suitable for highly dynamic, crowded in vivo environments [121, 138, 139]. In addition, flow-based quantification enabled consistent comparison across animals and time points, revealing spatiotemporal patterns associated with lesion outcome.

4.5.4 Quantification and Data Analysis

To access motion directionality relative to lesion centers, lesion positions were manually selected at early timepoints. For each voxel in the flow field, a radial vector from the lesion center to the voxel location was computed. Directionality was

determined by the sign of the dot product between the flow vector and radial vectors. A positive dot product indicated outward motion, while a negative one indicated inward motion. The angle between the two vectors was also computed for visualization, but the sign of the dot product determines the flow direction.

Hotspot motion analysis was performed by thresholding the motion magnitude field to identify the regions of locally high activity. Connected components above a fixed percentile threshold were labeled as hotspots, and their spatial position and temporal persistence were tracked across the time series. Summary metrics such as hotspot counts, area, centroid distance to lesion, and directionality bias were extracted to support comparative analysis between lesion types.

To evaluate whether cells moved inward or outward relative to lesions, we calculated the radial motion bias using a 2D formulation on selected Z-slices of the velocity field. Let $\vec{r}_i$ be the 2D radial unit vector pointing from the lesion center to voxel i, and let $\vec{v}_i = (v_x, v_y)$ be the 2D optical flow vector at voxel i on the selected Z-slice. The radial motion component is computed as the dot product:

$$R_i = \vec{v}_i \cdot \vec{r}_i = |\vec{v}_i| \cos\theta_i$$

where θ_i is the angle between the velocity and radial direction. If $R_i > 0$, motion is directed outward; $R_i < 0$ meaning inward. We define the radial motion bias as the average cosine similarity between motion and radial direction across all voxels:

$$Radial\ Motion\ Bias = \frac{1}{N}\sum_{i=1}^{N}\frac{\vec{v}_i \cdot \vec{r}_i}{|\vec{v}_i|}$$

where N is the total number of voxels. Angular distributions $\theta_i \in \left[0, \frac{\pi}{2}\right]$ were visualized using polar histograms, and the percentage of inward motion ($R_i < 0$) was also calculated to access directional preference.

All downstream quantification, statistical analysis, and figure generation were performed in Python and MATLAB.

Chapter 5: Discussion and Future Directions

5.1 Summary of Key Findings

This thesis integrates computational image analysis and cancer biology to investigate collective cell behavior across a variety of systems. In Chapter 2, we demonstrated the power of AI-based label-free tracking in epithelial monolayers. By extracting metrics such as D^2_{min} and affine deformation, we quantified subtle rearrangement behaviors and distinguished between non-tumorigenic, tumorigenic, and metastatic cell lines. These metrics enabled a deeper understanding of how cell populations organize and move collectively.

Chapter 3 built on this framework by introducing environmental cues, nanoscale topography. We found that while topographical features like ridges significantly affected migration speed and directionality, they did not alter spatial mixing patterns. Importantly, cell identity and mutation status, particularly the KRas/PTEN double mutation, played a dominant role in overriding environmental influence.

In Chapter 4, we transitioned to in vivo models and used 3D optical flow to analyze the motion of myeloid cells in live animals. This allowed us to track collective immune behavior near tumor lesions. Our analysis revealed spatiotemporal patterns of motion, with increased activity often occurring near lesion boundaries. Preliminary observations also suggest that early immune behavior may relate to lesion progression or regression.

Several unifying themes emerge from the work presented in this thesis. First, quantitative motion metrics, ranging from D^2_{min} to affine deformation and 3D optical flow, provide powerful tools for dissecting complex cellular dynamics. These methods not only enable precise measurements but also allow comparisons across experimental systems.

Second, the results consistently highlight that collective behavior is both context and cell type dependent. Whether in epithelial sheets responding to substrate topography or immune cells navigating through tissue, the microenvironment and genetic background jointly shape how cells migrate and interact.

Lastly, label-free approaches have proven to be broadly applicable. The same tracking framework developed for in vitro epithelial systems was successfully applied to 3D immune contexts, illustrating its versatility.

5.2 Limitation and Technical Challenges

Aside from the advances we made, several limitations remain. Label-free tracking is challenged by high cell density or overlapping features, particularly in crowded tissues. While optical flow captures large-scale motion in 3D, it may miss the dynamics of individual cells or rare events. A recent breakthrough by Dr. Desu Chen in the Weigert Lab offers promising improvements in this area and could be integrated into the analysis workflow in future studies.

Additionally, D^2_{min} and affine motion analysis are local. While powerful for assessing neighborhood-level coordination, they may not fully capture global patterns or long-range interactions.

Finally, optical flow methods rely on detecting changes in image gradients between frames, which makes them sensitive to the quality of the input images. In conditions with low signal-to-noise ratios or weak contrast, accuracy can suffer. Subtle cell movements may fall below the detection threshold or become smoothed out by noise filtering. In 3D datasets, these challenges are further amplified. The performance of 3D optical flow is particularly dependent on axial resolution and the spacing between z-slices. Poor z-resolution or coarse axial sampling can reduce the fidelity of motion vectors, especially in the z direction, and may bias motion quantification toward the xy-plane.

5.3 Future Directions

There are several promising directions for future work. One of them is the continued refinement of segmentation and tracking tools. Enhancing performance in 3D, improving robustness to imaging noise, and expanding to additional cell types would broaden applicability. Another exciting opportunity lies in bridging molecular and behavioral data. For example, integrating single-cell RNA-seq or proteomic data with motion phenotypes could reveal regulatory networks underlying migration behavior. There is also potential in developing predictive models. Using motion-derived features to anticipate lesion fate or therapy response could have diagnostic or prognostic value. Real-time analysis tools would enable adaptive experiments, such as altering treatment based on observed immune behavior. Ultimately, translating these findings to samples from patients could increase clinical relevance.

Beyond computational and translational advances, the quantitative readouts developed in this work also suggest concrete experimental directions for biologists. Perturbing adhesion pathways, such as blocking cadherin or integrin mediated signaling, could test whether altered mixing and motion coherence arise directly from changes in cell-cell or cell-matrix adhesion. Controlling microenvironment mechanics through changes in ridge geometry or substrate stiffness would reveal the physical scales at which coordination is maximized. Chemical cues, for example gradients in CXCL12 (also known as stromal cell-derived factor 1, a chemokine that directs cell migration), can be combined with nanotopography to determine whether biochemical and physical guidance act synergistically or in competition.

To sum up, this work presents a multiscale framework for quantifying collective behavior in cancer-related contexts. By developing and applying novel computational tools, we gained insight into how cell motion is shaped by genetics, environment, and tissue organization. The use of label-free imaging along with other approaches highlights the accessibility and broad applicability of these methods. The concepts and tools developed in this thesis provide a foundation for future investigation into collective cell behavior, with potential applications in both basic biology and translational cancer research.

Appendix A: Excitable Systems: A new perspective on the cellular impact of Elongate Mineral Particles

This chapter is adapted from the manuscript by Gu, Bull, Perry, Huang, Hourwitz, Abostate, Fourkas, Korchevskiy, Wylie and Losert, originally published in *Environmental Research* on Aug 1, 2023. Shuyao Gu served as the lead graduate researcher on this study, developed and performed the experiments and analysis, and wrote a first draft of the manuscript.

A.1 Overview

We investigate how the geometry of elongate mineral particles (EMPs) in contact with cells influences esotaxis, a recently discovered mechanism of texture sensing. Esotaxis is based on cytoskeletal waves and oscillations that are nucleated, shaped, and steered by the texture of the surroundings. We find that all EMPs trigger an esotactic response in macrophages, and that this response impact cytoskeletal activity in these immune cells. In contrast, epithelial cells show little to no esotactic response to all EMPs. These results are consistent with the distinct interactions of these both cell types with ridged nanotopographies of dimensions comparable to those of asbestiform EMPs. Our findings raise the question of whether narrow asbestiform EMPs may also dominate cytoskeletal activity in other types of immune cells that exhibit similar esotactic effects. These findings, together with prior studies of esotaxis, lead us to the hypothesis that asbestiform EMPs suppress the migration of immune cells

and activate immune signaling, thereby outcompeting signals that would normally activate the immune system in nearby tissue.

A.2 background

Recent studies on elongate mineral particles (EMPs) strongly suggest that the geometry of amphibole EMPs is more important than the mineral composition in causing adverse health effects, in particular when the fibers have diameters less than 250 nm, lengths greater than 5 μm, and an aspect ratio of at least 3:1 [140]. The diameters of crocidolite, the most carcinogenic category of fibers, although roughly two orders of magnitude smaller than a cell diameter, are still larger than the 5 nm size of typical proteins in cells. Thus, it is unlikely that any single protein could distinguish, say, a particle with a 200 nm diameter from a particle with a diameter of 1 μm or more, but rather a larger scale system that allows cells to sense the particles.

There has been a significant focus in toxicological studies on understanding how EMPs are transported through the human respiratory system, in the attempt to explain the carcinogenic potential of thin fibers as being due to the lower probability that such thin fibers can be cleared by the lungs before interacting with sensible tissues, such as the mesothelial layer. Some studies in which asbestiform and nonasbestiform EMPs were implanted directly into animals have shown that thin fibers have a greater adverse impact on health [141-143]. Similarly, it is well established that both the average width and the potency of amphibole asbestos vary with geological source [140,

144]. It is therefore important to understand how cells differentiate the diameters of EMPs.

In this study, we focus on the recently discovered phenomenon of esotaxis, which allows cells to sense the physical properties of their surroundings, including textures on a submicron scale [60]. Esotaxis is based on the dynamics of polymerization and depolymerization of actin, which create micron-scale, wave-like structures in cells. These dynamic structures are capable of sensing aspects of the microenvironment such as texture [145] and electric fields [146]. Actin has long been known to be an essential element in cytoskeletal structure and cellular movement [147]. In most previous studies, actin polymerization has been considered to be an output of cellular sensing and decision-making [148-150]. Recent work has shown that actin polymerization has intrinsic excitable dynamics, with self-sustaining waves [145] that can be observed in many cell types [151, 152]. Our prior work showed that in both epithelial cells and neutrophils, actin-polymerization waves can be guided by ridges with submicron widths and micron-scale spacings [153]. Esotaxis can also affect downstream signaling, for instance by modulating the activation of B cells [154] and T cells [155].

In this study, we consider the role of esotaxis in the interaction of cells with rigid amphibole asbestiform EMPs. We introduce a systematic data analysis approach that allows us to compare the esotactic response of cells to asbestiform and nonasbestiform EMPs. We further contrast the behavior of two of the major cell types known to be affected by EMPs, epithelial cells (MCF10A in this work) and macrophages (THP-1 in this work).

A.3 Results

Immune cells, such as macrophages, neutrophils, and others, act as the first line of defense against pathogens in the body, including aberrant cells. As a part of the innate immune system, macrophages are recruited to local tissue sites by chemical, electrical, and physical signaling cues. Actin polymerization waves modulate the mechanical scaffolding of cells and help to direct migration to wound sites [60, 153]. THP-1 cells exhibit highly active actin dynamics at the cell boundary. These dynamics do not result in protrusions or movement but rather cause the locations of high actin polymerization activity to vary over time. Additionally, the cells display actin-rich puncta when plated on flat glass substrates, indicating that there is adhesion to such surfaces. When plated on ridged nanotopograhpies, the macrophages align with, and extend along, the nanoridges (Figure A1a). The macrophages do not display actin waves in the valleys of the ridges. Instead, the cells exhibit a heightened level of actin fluorescence at the ridge locations. In contrast, epithelial cells plated on nanoridges exhibit actin signals in the valleys between the ridges, in the form of either straight strips or wiggly lines in the gaps [153].

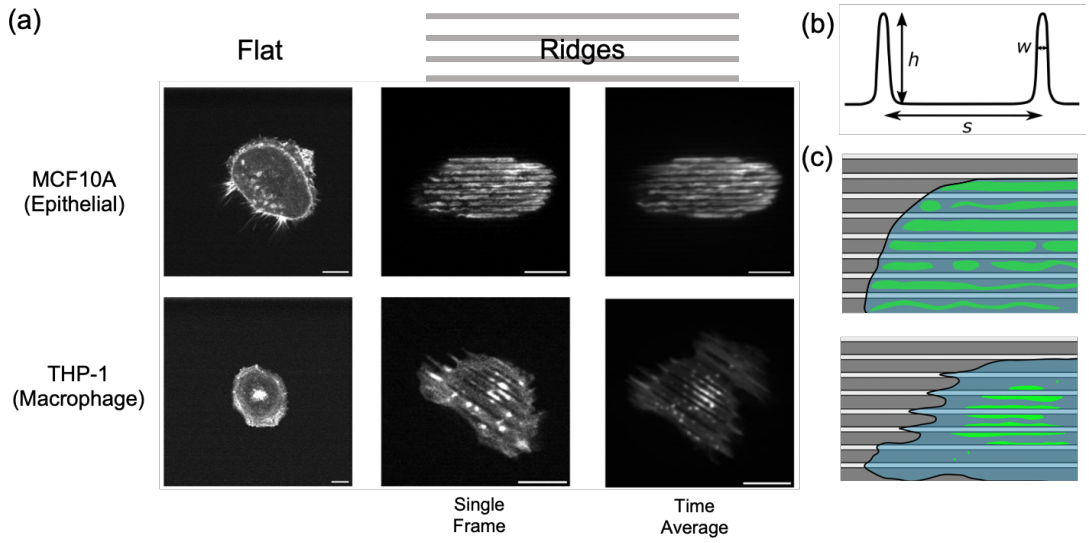


Figure A1: Macrophages and epithelial cells have different esotactic responses. (a) Fluorescence images of epithelial cells (top) and macrophages (bottom) on different topographies, with the columns displaying images of both cell lines on flat surfaces, on ridged surfaces, and time-averaged images to emphasize the actin dynamics, respectively. The scale bars are 10 µm. (b) A cross-section schematic of the ridges. The ridge spacing *s* is 1.5 µm, the ridge width *w* is 250 nm, and the ridge height *h* is 1 µm [58]. (c) Cartoons of epithelial cells (top) and macrophages (bottom) on ridges, with blue denoting cell regions and green highlighting the locations of actin activity.

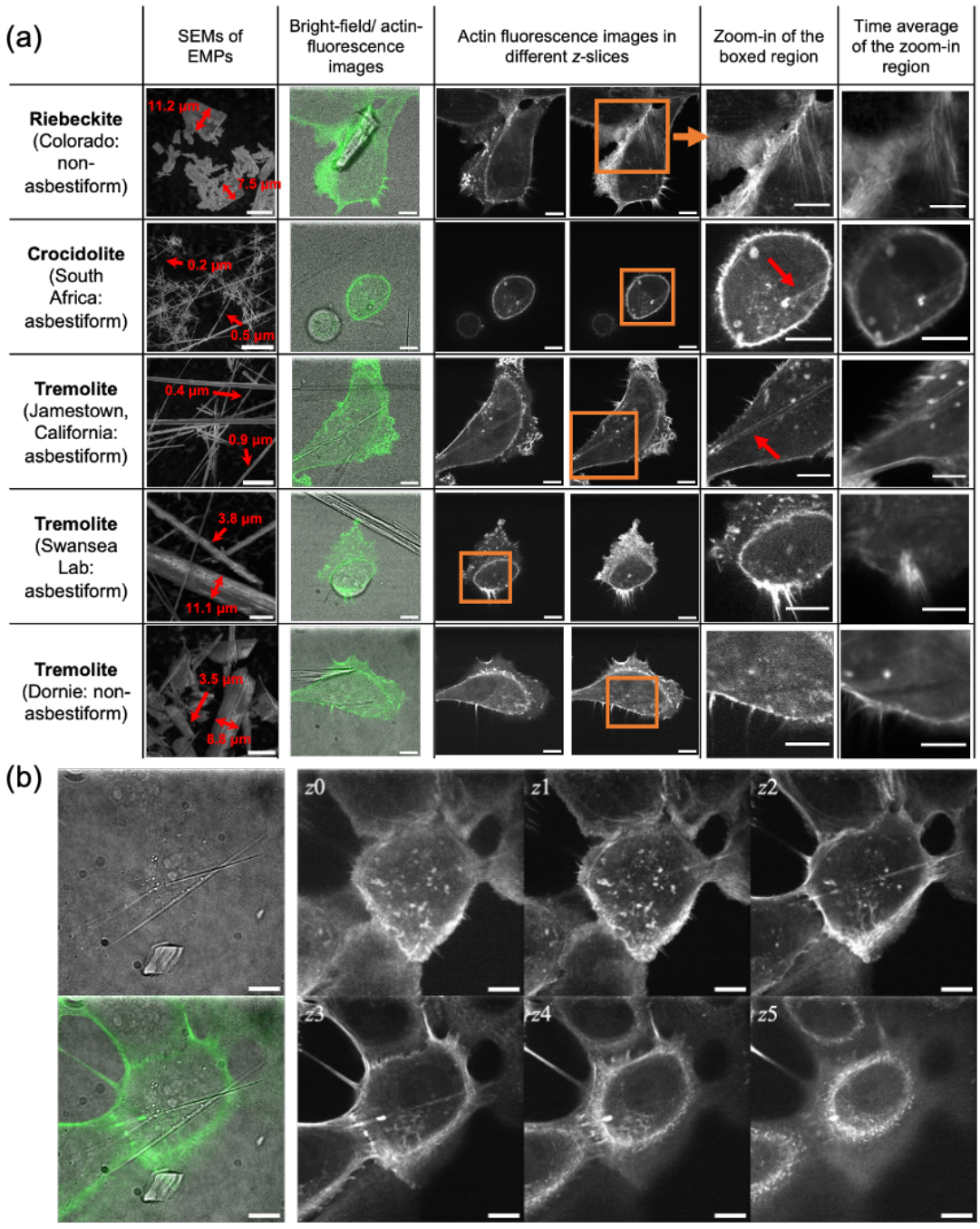


Figure A2: Epithelial cells exhibit little to no response to all EMPs. (a) A table of all the EMPs used in the experiments: Riebeckite, Crocidolite, Jamestown Tremolite, Swansea Lab Tremolite, and Dornie Tremolite. For each type of EMP, a sample SEM is provided, with width measurements of two of the particles labeled in red. Overlays of bright-field (grey) and actin-fluorescence (green)

images in the second column show the actin activity relative to the locations of the EMPs. A zoomed-in image of the marked orange box is provided in the next column. Actin-fluorescence images at a single time point are shown for two different heights (0.75 μm apart). The final two columns show single-time-point and time-averaged images of the zoomed-in, orange-boxed region, respectively. (b) Representative bright-field (top left), a bright-field/actin-fluorescence composite images (bottom left), and actin images (*z*0-*z*6) at different heights (with a 0.75 μm step) are shown for Jamestown tremolite interacting with epithelial cells. *z*0 is near the bottom of the cell and subsequent images approach the top. The scale bars are 10 μm.

For the qualitative characterization of the different kinds of EMPs used in the experiments, we obtained scanning electron micrographs (SEMs) of each sample (Figure A2a). Non-asbestiform riebeckite and Dornie tremolite are composed of fragments with small aspect ratios. Crocidolite, Jamestown tremolite, and Swansea Lab tremolite particles, which are all asbestiform, have high aspect ratios. Crocidolite fibers are the thinnest and Swansea Lab tremolite fibers are the thickest among these three.

To study how epithelial cells interact with all EMPs, we obtained bright-field and fluorescence images (Figure A2a). Fluorescence images of epithelial cells showed little to no actin response to contact with EMPs of any size. The two thinnest asbestiform EMPs, crocidolite and Jamestown tremolite, induced weak actin signals at the fibers. We did not observe any actin response for cells in contact with the other three EMPs, even upon scanning different *z*-planes of the cells. A representative *z*-stack of images

in which Jamestown tremolite fibers are interacting with cells is shown in Figure A2b. Six *z*-slice images (*z*0 to *z*5) were taken at heights from near the bottom of the cells to near the top, in 0.75-μm increments. Multiple fibers appear in the bright-field image, but the fluorescence image shows actin responding only to a single fiber. Moreover, this actin response occurs at multiple *z*-planes within the cell, and is most prominent in the *z*2 and *z*3 planes. All of the images in Figure A2 indicate that epithelial cells have weak to no actin response to all EMPs, and only for thinner asbestiform EMPs (crocidolite and Jamestown tremolite) is there some actin activity at the sites of some fibers.

We also obtained bright-field and fluorescence images of macrophages during EMP exposure (Figure A3). We captured 15-min movies at 2 frames/second in one single *z*-slice. We analyzed still frames of these movies at 0:00, 5:00, 10:00, and 15:00 min following exposure to visualize how interactions with EMPs influence THP-1 actin dynamics. We observed that macrophages have strong interactions with all EMPs, as is indicated by the regions of enhanced actin polymerization located along the EMPs in Figure A3. In contrast to the epithelial cells, macrophages exhibit a similar response to all five of the EMP samples tested here.

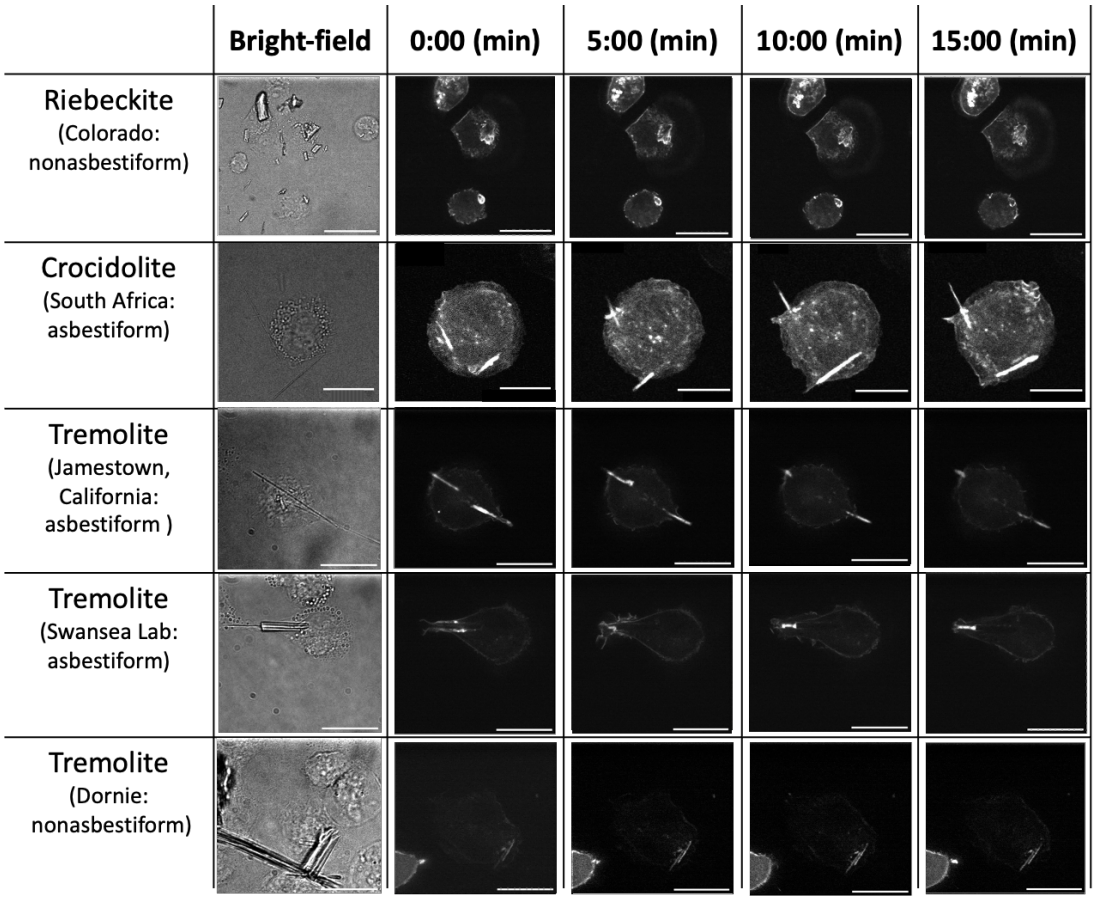


Figure A3: EMPs trigger esotatic response in macrophages. Actin-fluorescence images obtained at different time delays following exposure to asbestiform (Crocidolite, Tremolite: Jamestown and Swansea Lab) and non-asbestiform (riebeckite and tremolite: Dornie) EMPs. The bright-field images indicate the locations of the particles relative to the macrophages. The scale bars are 30 μm.

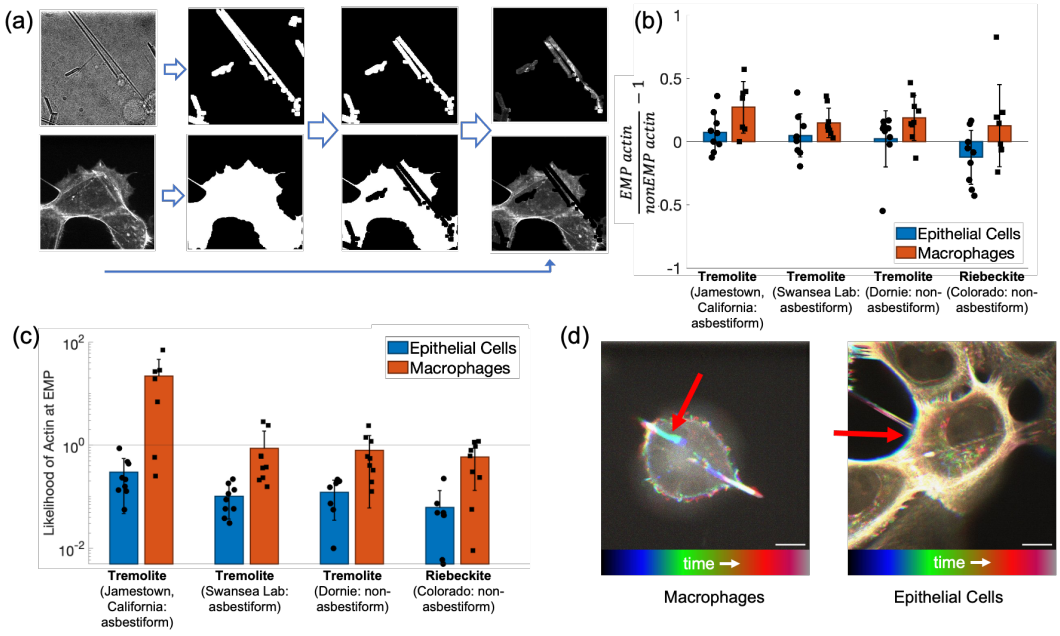


Figure A4: Narrow Asbestiform EMPs dominate cytoskeletal activity in macrophages. (a) Segmentation workflow for image analysis. A bright-field image is used to create a mask for EMP segmentation. The corresponding fluorescence image is used to create a mask to segment cell regions (left half). The EMP-segmentation and cell-segmentation masks are added/subtracted to generate masks for the cell regions with EMPs (top) and without EMPs in cells (bottom). By combining these masks with the original actin images, we can obtain actin images at the sites in cells with EMPs (top) and without EMPs in cells (bottom). This workflow has limitations when applied to asbestiform crocidolite samples due to the image resolution, so asbestiform crocidolite data were excluded in the following quantification analysis. (b) The average actin intensity in regions without EMPs was subtracted from the intensity in regions with EMPs frame-wise over the length of the movies to calculate the excess average actin intensity for epithelial cells (blue) and macrophages (orange). Each marker represents one

movie of cells interacting with EMPs. (c) We identified the pixels with the 5% highest fluorescence intensity and calculated what fraction of these pixels is located near EMPs. (d). Time-evolution image of a macrophage (left) and epithelial cells (right) interacting with Jamestown tremolite. Both images were generated from image sequences covering 800 s. The scale bars are 10 μm. The error bars in (b) and (c) represent plus or minus one standard deviation across independent replicates. In (c), the negative ends of the error bars are not shown in cases in which they are outside of the range of ratios shown.

To quantify the actin response of different cells to various EMPs, we created an image-segmentation workflow to identify the EMP regions of interest (ROIs). Using morphological operations, we generate a binary mask of the ROIs with EMPs from the bright-field image (Figure A4a). The corresponding fluorescence image is used to generate a binary mask of the cell regions. By adding or subtracting these two masks, we created masks for ROIs with and without EMPs. Applying these masks to the fluorescence images, we obtain fluorescence images for ROIs in cells with and without EMPs. The resultant images were used to analyze the difference in the actin activity between the two types of ROI. (Figure A4b). Note that this segmentation method can be limited by the resolution and magnification of bright-field images. For most EMP samples used here, this method can extract the locations of most mineral fragment samples. However, some fibers from asbestiform crocidolite are too small and too thin to discern in 512×512 pixels images and are difficult to separate from cells in the bright-field images under 100× magnification. The fact that these narrow and light-weight

fibers reside at different heights in the cells, combined with the greater number of fibers interacting with individual cells, lead to imprecise masking (Figure A5) and prevents quantification. Therefore, only three kinds of tremolites and one non-asbestiform Riebeckite samples are used for the following quantification analysis. After generating the segmentation masks, we first compared the time average of the actin fluorescence intensity of ROIs with and without EMPs for four EMP samples used. The excess average actin intensity is the difference in the average actin intensities in ROIs with and without EMPs divided by the average actin intensity in ROIs without EMPs. Values above zero correspond to cell movies in which the actin in EMP regions is brighter than in other areas of the cells. Epithelial cells have excess actin intensity values close to zero, indicating that the actin intensity in regions of the cells with EMPs is similar to that in regions without EMPs. In other words, epithelial cells do not have a significant actin response to the EMPs investigated here. In contrast, macrophages exhibit higher excess average actin intensity for EMPs from the asbestiform Jamestown sample. This observation indicates that macrophages have a stronger actin response to some asbestiform EMPs as compared to epithelial cells.

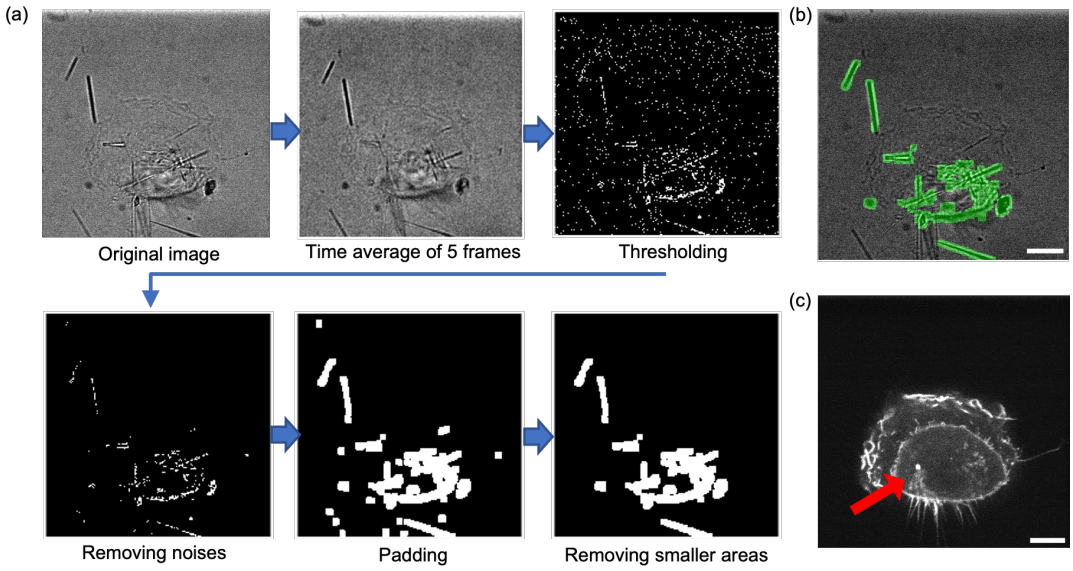


Figure A5: Sample crocidolite segmentation. (a) One sample crocidolite bright-filed movie first went through moving-frame-average of 5 frames to remove some background noises. The smoothed movie is then thresholded to find darker regions that are usually from the fibers. The result is then cleaned up and padded to keep only sizable regions that potentially represent EMP fibers. (b) The EMP fiber mask (in green) overlay the original bright-field image. (c) The corresponding actin-fluorescence image.

We also investigated the brighter parts of the regions of cells with and without EMPs by finding the highest 5% of actin intensity values (Figure A4c). We calculated the ratio of the probabilities that the brightest pixels are in ROIs with EMPs compared to elsewhere in the cell. This measure describes how likely it is that the brightest pixels lie near EMPs: A value of 1 means that both are equally likely, and higher values represent a greater likelihood of the brightest actin fluorescence pixels being near EMPs. For both cell lines and all EMP samples, only macrophages interacting with

Jamestown tremolite showed a higher percentage of brighter actin signals near EMP as compared to the rest of the cell. Figures 4b and 4c indicate that the thinner EMP sample, Jamestown tremolite, triggers the strongest actin polymerization response by both measures for the EMPs tested.

We also created representative time-evolution images of both cell lines interacting with Jamestown tremolite to visualize the dynamics of actin (Figure A4d). The image sequence is spectrally time coded; the initial frames are coded in blue, and the final frames are coded in red. The white regions in the composite images indicate regions in which the actin dynamics is stationary, whereas the regions with different colors are locations of transient actin dynamics. Macrophages exhibit a higher degree of actin dynamics at the locations of EMPs, as indicated by the arrows in the figure. The actin dynamics at EMP locations in epithelial cells are subtle, with the majority of actin occurring at the cell boundaries.

A.4 Discussion

In this study, we showed that EMPs can trigger actin waves in cells (Figures A2 and A3), indicating a cell's capability of detecting the change in local topography caused by the presence of EMPs. This actin response to EMPs is dependent on both the cell type and the mineral sample. Figures A2-A4 indicate that, in general, epithelial cells have a weaker (or no) response to all types of EMPs than do the macrophages, the latter of which respond strongly to the presence of all the EMPs tested here.

The different types of EMPs tested here triggered different amounts of actin polymerization. The thinner asbestiform tremolite samples elicited the strongest

response. Among the three types of tremolites used in this study, Jamestown tremolite, which has the thinnest fibers, led to the most heightened actin signals. Crocidolite, another EMP sample with very thin fibers, also triggered relatively strong actin response in both epithelial cells and macrophages compared to EMP samples with bigger widths. These observations are consistent with the width of the fibers playing an important role in triggering actin responses in cells.

Interestingly, the macrophages studied here exhibited enhanced actin activity upon interaction with all of the EMPs studied here. The actin fluorescence signals are brighter at the location of EMPs than along the cell boundary. These results are suggestive of substantial cellular interaction with EMPs, which may impact boundary-shape changes and cell migration. As is the case for epithelial cells, macrophages tend to have a stronger response to longer, thinner fibers than to shorter, wider particles. In particular, the highly asbestiform Jamestown tremolite have higher excess average actin intensity and higher likelihood of brightest actin fluorescence pixels in regions of EMPs (Figure A4). These observations indicate that EMPs may ultimately influence the innate overall migration patterns of macrophages in a manner that depends on EMP morphology.

The strong dependence of the actin response on EMP geometry width and cell type is consistent with our prior observation of the responses of both macrophages (unpublished) and epithelial cells [153] to surface textures (Figure A1). Macrophages have actin signals at the location of individual substrate ridges, whereas epithelial cells respond to the valleys formed between adjacent ridges. For cells sensing local topography, asbestiform EMP fibers appear analogous to individual ridges. The widths

of the ridges that have been studied in this context [58] are similar to the widths of Jamestown tremolite fibers (Figures A1 and A2). The heightened actin activity in at the locations of EMPs interacting with macrophages is consistent with the actin polymerization phenotype of these cells on nanoridges. Because epithelial cells sense "valleys," such as the concave structure between adjacent ridges, individual EMP fibers triggers little to no actin response. The slight response of the epithelial cells to the Jamestown tremolite and crocidolite samples two of the highly asbestiform samples may be a response to valleys that form between the narrower fibrils that make up the fiber. These findings suggest that esotaxis, the process of sensing the environment through internal waves [60], is a means of predicting how strongly different cell types are affected by the presence of EMPs.

This similarity between the responses of actin dynamics to EMPs and nanotextured surfaces suggests that the response of immune cell to textured surfaces is relevant to understanding the effects of EMPs on the immune system. Recent work has demonstrated that textures of size comparable to asbestiform EMPs drives cytoskeletal waves and activates both B cells and T cells even when molecular immune signals are absent [154, 155]. Thus, this mechanism may allow EMPs may to not only inhibit the immune-cell migratory machinery, but may also trigger immune signaling, guiding other immune cells to the same site. Thus, nearby regions in the mesothelium could experience a weakened immune response, depriving the tissue of the healing power of the immune system. Indeed, severe immunodeficiency was implicated as one of the factors associated with an increased risk of malignant mesothelioma, even in the absence of known exposure to asbestos [156]. Thus, we propose that the esotactic

response of immune cells to EMPs, which results in suppression of cell migration and immune-cell activation, may divert the body's own defenses against malignancies. This mechanism of indirect carcinogenic action is not predicated on the mineral nature of EMPs, and thus potentially also applies to other elongate particles of comparable geometry. It will therefore be important to characterize the esotactic immune response further and to identify novel approaches that may suppress this immune activation pathway

A.5 Materials and Methods

Elongate Mineral Particles

Multiple asbestiform and non-asbestiform amphibole particle samples were used in this study. Asbestiform minerals naturally crystallize into bundles of long, thin, flexible, and durable fibers. Non-asbestiform amphiboles produce EMPs upon fragmentation via mechanical forces. Non-asbestiform particles are rigid, and lack the tensile strength of asbestiform varieties [157]. In general, for any given length, asbestiform particles are narrower (i.e., have a higher aspect ratio). No correlation between lung cancer or malignant mesothelioma risk and exposure to non-asbestiform amphiboles has been demonstrated, in contrast to the well-established, high incidence of these diseases upon exposure to amphibole asbestos [158, 159].

Our experiments used Jamestown, California tremolite, Swansea Lab tremolite, Dornie, Scotland nonasbestiform tremolite, nonasbestiform riebeckite Colorado, and

crocidolite asbestos from South Africa. The Jamestown tremolite, Swansea tremolite, and Dornie tremolite samples were those reported by Davis et al. (1991) [142] in a study of peritoneal mesothelioma in rats induced by the implantation of EMPs. Jamestown tremolite, Swansea tremolite, and crocidolite are characterized as asbestiform. The nonasbestiform minerals were ground, and particles with dimensions of less than 25 μm were obtained by sieving. The asbestiform materials were used as received. The materials were dispersed in distilled water to a concentration of 300 μg/mL. Note that samples with thinner or shorter individual fragments or fibers have a correspondingly higher count of particles/ml than do non-asbestiform particles because non-asbestiform particles have on average a larger volume compared to asbestiform particles. Some of the Dornie tremolite samples and Swansea tremolite suspensions were found to be contaminated with microorganisms which led to massive cell deaths after plating. To sterilize these samples, we autoclaved Dornie tremolite samples and Swansea tremolite suspensions at 121 °C for 25 min (Panasonic MLS-3751L) under the programmed liquid sterilization procedure and cell deaths were avoided after the sterilization.

Cell Lines and Cell Culture

Human THP-1 cells, a leukemia monocytic cell line, were a gift from the laboratory of Iqbal Hamza (University of Maryland, College Park). These cells were maintained at 37 °C in a humid, 95% air/5% CO_2 atmosphere in RPMI-1640 medium (ThermoFisher Scientific) containing 10% fetal bovine serum (Gemini Bio-Products) and 55 mM beta-mercaptoethanol (EMD Millipore). The cells were transfected with

the green fluorescent protein LifeAct-GFP, which is a biomarker that selectively binds to F-actin, enabling real-time intercellular observations of actin dynamics.

To observe THP-1 macrophages interacting with EMPs, cells were plated at a 2×10^5 cells/ml density, and phorbol-12-myristate 13-acetate (Sigma-Aldrich) was added to the cell medium, for a final concentration of 100 nM, to trigger differentiation from monocytes to M0 macrophages. After 3 days, the cells became adherent and lost their ability to replicate, displaying the desired macrophage-like morphology. Subsequently, 100 μL of EMP solution was added, and images were obtained 1-2 h after exposure for both EMP-exposed cells and positive controls.

MCF10A LifeAct cells (ATCC), a non-tumorigenic human mammary epithelial cell line, were a gift from the laboratory of Stuart. S. Martin (University of Maryland School of Medicine, Baltimore, MD). These cells were cultured in a medium based on DMEM/F12 with 5% horse serum (both ThermoFisher Scientific), 10 μg/mL insulin (ThermoFisher Scientific), 20 ng/mL EGF (Peprotech, Rocky Hill, NJ), 0.5 μg/mL hydrocortisone, and 100 ng/mL cholera toxin (both Sigma, St. Louis, MO) as additives. The medium was additionally supplemented with 50 ng/ml puromycin (A.G Scientific, San Diego, CA) for LifeAct GFP selection. The MCF10A LifeAct cell line was incubated at 37 °C in a 95% air/5% CO2 atmosphere and was passaged every 3-4 days.

Before imaging, a 2 mL solution of MCF10A cells was plated in 35-mm-diameter glass-bottom plates at a density of 10^4 cells/mL. 24 h later, the medium in each well was replaced with fresh, warm medium and 100 μL of EMP solution. Because epithelial cells did not show a notable response after 1-2 hours in preliminary studies,

we imaged both EMP-exposed cells and the cellspositive controls after 24 h to allow sufficient time for interactions between the minerals and the cells.

Time-lapse microscopy

Both cell types were imaged by using a PerkinElmer spinning-disk confocal microscope with a 100× objective (0.14 μm/pixel) with 512×512 pixels camera resolution. Time-lapse images of actin dynamics were obtained in confocal fluorescence and bright-field modes. For MCF10A experiments, imaging was performed for 20 m at a frame rate of 3/min. Z-stack data with a z-step of 0.75 μm were obtained for some MCF10A samples to capture more details regarding how EMPs influence actin dynamics. Z-step of 0.75 μm is at the limit of confocal microscope we were using. For THP-1 experiments, fluorescence and bright-field movies were captured at 30 frames/min and 2 frames/min, respectively, for 15 m. Images were captured with a 16-bit Hamamatsu ImagEM X2 EM-CCD camera (C9100-23B) controlled by PerkinElmer's Quorum's Volocity software (version 6.4.0).

Image analysis

The images collected in this paper were all processed and analyzed using ImageJ and/or MATLAB. Feature extraction of EMPs and actin regions was performed in MATLAB by using morphological operations. Asbestiform EMPs usually appear as darker regions in bright-field images, so rescaling and thresholding were used to extract EMP regions. Note that in some cases, it was necessary to go to a different z-plane to improve contrast, as asbestiform EMPs can be difficult to discern when completely in focus. For cases in which z-plane images were not available, EMP regions were manually segmented using ImageJ.

Appendix B: 3D Optical Flow Calculation

This appendix shows the mathematical formulation of the 3D optical flow method used to extract local motion information from intravital imaging data. A 3D extension of the Lucas-Kanade optical flow method was used to estimate voxel-wise velocity vectors between successive timepoints in temporally smoothed image stacks. The resulting velocity field quantifies local motion in three spatial dimensions.

B.1 Temporal Smoothing

Prior to computing optical flow, image volumes were temporally smoothed using a symmetric 5-frame kernel centered at each timepoint to reduce noise and improve numerical stability. The smoothed intensity $\tilde{I}(x, y, z, t)$ is given by:

$$\tilde{I}(x, y, z, t) = \sum_{\tau=-2}^{2} w(\tau) \cdot I(x, y, z, t + \tau)$$

where $w(\tau)$ is the smoothing kernel, with $\sum w(\tau) = 1$ normalization. In our implementation, we used the following weights:

$$w = \left[\frac{1}{16}, \frac{1}{4}, \frac{3}{8}, \frac{1}{4}, \frac{1}{16}\right] \; for \; \tau = [-2, -1, 0, 1, 2]$$

This step reduces temporal fluctuations while preserving motion dynamics.

B.2 3D Optical Flow Formulation

Let $I(x, y, z, t)$ represent the image intensity at position (x, y, z) and time t. The optical flow assumptions states that the intensity of moving objects remains constant over time:

$$I(x, y, z, t) = \mathrm{I}(\mathrm{x} + v_x\Delta t, \mathrm{y} + v_y\Delta t, \mathrm{z} + v_z\Delta t, \mathrm{t} + \Delta \mathrm{t})$$

Applying first-order Taylor expansion and omitting higher order terms:

$$I(x, y, z, t) = \mathrm{I}\big(\mathrm{x} + v_x\Delta t, \mathrm{y} + v_y\Delta t, \mathrm{z} + v_z\Delta t, \mathrm{t} + \Delta \mathrm{t}\big)$$

$$\approx\ I(x, y, z, t) + I_x v_x\Delta t + I_y v_y\Delta t + I_z v_z\Delta t + I_t\Delta t$$

Removing $I(x, y, z, t)$ on both sides and dividing by Δt, we got the 3D optical flow constraint equation:

$$I_x v_x + I_y v_y + I_z v_z + I_t = 0$$

where I_x, I_y, I_z are spatial image gradients, I_t is the temporal image gradient, and (v_x, v_y, v_z) are the components of the local velocity vector.

Because this equation is underdetermined at each voxel, the Lucas-Kanade method also assumes the motion is approximately constant within a neighborhood, solves for a single velocity vector per neighborhood Ω by minimizing the weighted least-square error:

$$\min_{\vec{v}} \sum_{i\in\Omega} \omega(i)\big[I_x(i)v_x + I_y(i)v_y + I_z(i)v_z + I_t(i)\big]^2$$

where $\omega(i)$ is a spatial Gaussian kernel centered in the local neighborhood.

Bibliography

1. Marchetti MC, Joanny JF, Ramaswamy S, Liverpool TB, Prost J, Rao M, et al. Hydrodynamics of soft active matter. Rev Mod Phys. 2013;85.
2. Ramaswamy S. The Mechanics and Statistics of Active Matter. Annual Review of Condensed Matter Physics. 2010;1(1):323-45. doi: 10.1146/annurev-conmatphys-070909-104101.
3. Vicsek T, Zafeiris A. Collective Motion. Physics Reports. 2012;517(3-4):71-140.
4. Alert R, Trepat X. Physical Models of Collective Cell Migration. Annual Review of Condensed Matter Physics. 2020;11(1):77-101. doi: 10.1146/annurev-conmatphys-031218-013516.
5. Camley BA, Rappel W-J. Physical models of collective cell motility: from cell to tissue. Journal of Physics D: Applied Physics. 2017;50(11):113002. doi: 10.1088/1361-6463/aa56fe.
6. Friedl P, Gilmour D. Collective cell migration in morphogenesis, regeneration and cancer. Nature Reviews Molecular Cell Biology. 2009;10(7):445-57. doi: 10.1038/nrm2720.
7. Keller R. Shaping the vertebrate body plan by polarized embryonic cell movements. Science. 2002;298:5600.
8. Poujade M, Grasland-Mongrain E, Hertzog A, Jouanneau J, Chavrier P, Ladoux B, et al. Collective migration of an epithelial monolayer in response to a model wound. Proceedings of the National Academy of Sciences. 2007;104(41):15988-93. doi: 10.1073/pnas.0705062104.
9. Rørth P. Collective cell migration. Annual review of cell and developmental biology. 2009;25.
10. Clark AG, Vignjevic DM. Modes of cancer cell invasion and the role of the microenvironment. Current opinion in cell biology. 2015;36:13-22.
11. Friedl P, Locker J, Sahai E, Segall JE. Classifying collective cancer cell invasion. Nature Cell Biology. 2012;14(8):777-83. doi: 10.1038/ncb2548.
12. Krummel MF, Bartumeus F, Gérard A. T cell migration, search strategies and mechanisms. Nature Reviews Immunology. 2016;16(3):193-201. doi: 10.1038/nri.2015.16.
13. Lämmermann T, Germain RN. The multiple faces of leukocyte interstitial migration. Seminars in Immunopathology. 2014;36(2):227-51. doi: 10.1007/s00281-014-0418-8.
14. Uderhardt S, Martins AJ, Tsang JS, Lämmermann T, Germain RN. Resident Macrophages Cloak Tissue Microlesions to Prevent Neutrophil-Driven Inflammatory Damage. Cell. 2019;177(3):541-55.e17. doi: 10.1016/j.cell.2019.02.028.
15. Mayor R, Etienne-Manneville S. The front and rear of collective cell migration. Nature Reviews Molecular Cell Biology. 2016;17(2):97-109. doi: 10.1038/nrm.2015.14.
16. Haeger A, et al. Collective cell migration: guidance principles and hierarchies. Trends in cell biology. 2015;25:9.

17. Vedula SRK, Leong MC, Lai TL, Hersen P, Kabla AJ, Lim CT, et al. Emerging modes of collective cell migration induced by geometrical constraints. Proceedings of the National Academy of Sciences. 2012;109(32):12974-9. doi: 10.1073/pnas.1119313109.
18. Angelini TE, Hannezo E, Trepat X, Marquez M, Fredberg JJ, Weitz DA. Glass-like dynamics of collective cell migration. Proceedings of the National Academy of Sciences. 2011;108(12):4714-9. doi: 10.1073/pnas.1010059108.
19. Sepúlveda N, Petitjean L, Cochet O, Grasland-Mongrain E, Silberzan P, Hakim V. Collective Cell Motion in an Epithelial Sheet Can Be Quantitatively Described by a Stochastic Interacting Particle Model. PLoS Computational Biology. 2013;9(3):e1002944. doi: 10.1371/journal.pcbi.1002944.
20. Sanchez-Vega F, Mina M, Armenia J, Chatila WK, Luna A, La KC, et al. Oncogenic Signaling Pathways in The Cancer Genome Atlas. Cell. 2018;173(2):321-37.e10. doi: 10.1016/j.cell.2018.03.035.
21. Szabó B, Szöllösi GJ, Gönci B, Jurányi Z, Selmeczi D, Vicsek T. Phase transition in the collective migration of tissue cells: Experiment and model. Physical Review E. 2006;74(6). doi: 10.1103/physreve.74.061908.
22. Park J-A, Kim JH, Bi D, Mitchel JA, Qazvini NT, Tantisira K, et al. Unjamming and cell shape in the asthmatic airway epithelium. Nature Materials. 2015;14(10):1040-8. doi: 10.1038/nmat4357.
23. Garcia S, Hannezo E, Elgeti J, Joanny J-F, Silberzan P, Gov NS. Physics of active jamming during collective cellular motion in a monolayer. Proceedings of the National Academy of Sciences. 2015;112(50):15314-9. doi: 10.1073/pnas.1510973112.
24. Prost J, Jülicher F, Joanny J-F. Active gel physics. Nature Physics. 2015;11(2):111-7. doi: 10.1038/nphys3224.
25. Doostmohammadi A, Ignés-Mullol J, Yeomans JM, Sagués F. Active nematics. Nature Communications. 2018;9(1). doi: 10.1038/s41467-018-05666-8.
26. Trepat X, Wasserman MR, Angelini TE, Millet E, Weitz DA, Butler JP, et al. Physical forces during collective cell migration. Nature Physics. 2009;5(6):426-30. doi: 10.1038/nphys1269.
27. Petridou NI, Corominas-Murtra B, Heisenberg C-P, Hannezo E. Rigidity percolation uncovers a structural basis for embryonic tissue phase transitions. Cell. 2021;184(7):1914-28.e19. doi: 10.1016/j.cell.2021.02.017.
28. Vicsek T, Czirók A, Ben-Jacob E, Cohen I, Shochet O. Novel Type of Phase Transition in a System of Self-Driven Particles. Physical Review Letters. 1995;75(6):1226-9. doi: 10.1103/physrevlett.75.1226.
29. Petitjean L, Reffay M, Grasland-Mongrain E, Poujade M, Ladoux B, Buguin A, et al. Velocity Fields in a Collectively Migrating Epithelium. Biophysical Journal. 2010;98(9):1790-800. doi: 10.1016/j.bpj.2010.01.030.
30. Falk ML, Langer JS. Dynamics of viscoplastic deformation in amorphous solids. Physical Review E. 1998;57(6):7192-205. doi: 10.1103/physreve.57.7192.
31. Gu S, Lee RM, Benson Z, Ling C, Vitolo MI, Martin SS, et al. Label-free cell tracking enables collective motion phenotyping in epithelial monolayers. iScience. 2022;25(7):104678. doi: 10.1016/j.isci.2022.104678.

32. Klauschen F, Ishii M, Qi H, Bajénoff M, Egen JG, Germain RN, et al. Quantifying cellular interaction dynamics in 3D fluorescence microscopy data. Nature Protocols. 2009;4(9):1305-11. doi: 10.1038/nprot.2009.129.
33. Etournay R, et al. Interplay of cell dynamics and epithelial tension during morphogenesis of the Drosophila pupal wing. eLife. 2015;(4):e07090.
34. Takeichi M. Dynamic contacts: rearranging adherens junctions to drive epithelial remodelling. Nature Reviews Molecular Cell Biology. 2014;15(6):397-410. doi: 10.1038/nrm3802.
35. Hynes RO. Integrins: Bidirectional, Allosteric Signaling Machines. Cell. 2002;110(6):673-87.
36. Johnston EK, Abbott RD. Adipose Tissue Paracrine-, Autocrine-, and Matrix-Dependent Signaling during the Development and Progression of Obesity. Cells. 2023;12(3):407. doi: 10.3390/cells12030407.
37. Lázár-Molnár E, Hegyesi H, Tóth S, Falus A. Autocrine and paracrine regulation by cytokines and growth factors in melanoma. Cytokine. 2000;12.
38. Alberts B, Johnson A, Lewis J, al e. Molecular Biology of the Cell. Garland Science. 2015.
39. Hanahan D, Weinberg A, Robert. Hallmarks of Cancer: The Next Generation. Cell. 2011;144(5):646-74. doi: 10.1016/j.cell.2011.02.013.
40. Discher DE, Janmey P, Wang Y-L. Tissue Cells Feel and Respond to the Stiffness of Their Substrate. Science. 2005;310(5751):1139-43. doi: 10.1126/science.1116995.
41. Trepat X, Sahai E. Mesoscale physical principles of collective cell organization. Nature Physics. 2018;14(7):671-82. doi: 10.1038/s41567-018-0194-9.
42. Zhao M, Song B, Pu J, Wada T, Reid B, Tai G, et al. Electrical signals control wound healing through phosphatidylinositol-3-OH kinase-γ and PTEN. Nature. 2006;442(7101):457-60. doi: 10.1038/nature04925.
43. Sun Y, Do H, Gao J, Zhao R, Zhao M, Mogilner A. Keratocyte Fragments and Cells Utilize Competing Pathways to Move in Opposite Directions in an Electric Field. Current Biology. 2013;23(7):569-74. doi: 10.1016/j.cub.2013.02.026.
44. Kienle K, Tim L. Neutrophil swarming: an essential process of the neutrophil tissue response. Immunological reviews. 2016;273(1).
45. Lämmermann T, Afonso PV, Angermann BR, Wang JM, Kastenmüller W, Parent CA, et al. Neutrophil swarms require LTB4 and integrins at sites of cell death in vivo. Nature. 2013;498(7454):371-5. doi: 10.1038/nature12175.
46. Theveneau E, Mayor R. Collective cell migration of epithelial and mesenchymal cells. Cellular and Molecular Life Sciences. 2013;70(19):3481-92. doi: 10.1007/s00018-012-1251-7.
47. Sarris M, Masson J-B, Maurin D, Aa D, Van, M., Lieke, Boudinot P, Lortat-Jacob H, et al. Inflammatory Chemokines Direct and Restrict Leukocyte Migration within Live Tissues as Glycan-Bound Gradients. Current Biology. 2012;22(24):2375-82. doi: 10.1016/j.cub.2012.11.018.
48. Germain RN, Robey EA, Cahalan MD. A Decade of Imaging Cellular Motility and Interaction Dynamics in the Immune System. Science. 2012;336(6089):1676-81. doi: 10.1126/science.1221063.

49. Casanova-Acebes Mea. Tissue-resident macrophages provide a pro-tumorigenic niche to early NSCLC cells. Nature. 2021;595.
50. Friedl P, Wolf K. Tumour-cell invasion and migration: diversity and escape mechanisms. Nature Reviews Cancer. 2003;3(5):362-74. doi: 10.1038/nrc1075.
51. Wolf K, Wu YI, Liu Y, Geiger J, Tam E, Overall C, et al. Multi-step pericellular proteolysis controls the transition from individual to collective cancer cell invasion. Nature Cell Biology. 2007;9(8):893-904. doi: 10.1038/ncb1616.
52. Cheung KJ, Andrew E. A collective route to metastasis: Seeding by tumor cell clusters. Science. 2016;352(6283).
53. De Visser KE, Joyce JA. The evolving tumor microenvironment: From cancer initiation to metastatic outgrowth. Cancer Cell. 2023;41(3):374-403. doi: 10.1016/j.ccell.2023.02.016.
54. Egeblad M, Nakasone ES, Werb Z. Tumors as Organs: Complex Tissues that Interface with the Entire Organism. Developmental Cell. 2010;18(6):884-901. doi: 10.1016/j.devcel.2010.05.012.
55. Yamaguchi H, Wyckoff J, Condeelis J. Cell migration in tumors. Current opinion in cell biology. 2005;17.
56. Lee RM, Vitolo MI, Losert W, Martin SS. Distinct roles of tumor associated mutations in collective cell migration. Scientific Reports. 2021;11(1). doi: 10.1038/s41598-021-89130-6.
57. Gu S, Bull A, Perry JK, Huang A, Hourwitz MJ, Abostate M, et al. Excitable systems: A new perspective on the cellular impact of elongate mineral particles. Environmental Research. 2023;230:115353. doi: https://doi.org/10.1016/j.envres.2023.115353.
58. Chen S, Hourwitz MJ, Campanello L, Fourkas JT, Losert W, Parent CA. Actin Cytoskeleton and Focal Adhesions Regulate the Biased Migration of Breast Cancer Cells on Nanoscale Asymmetric Sawteeth. ACS Nano. 2019. doi: 10.1021/acsnano.8b07140.
59. Lo C-M, Wang H-B, Dembo M, Wang Y-L. Cell Movement Is Guided by the Rigidity of the Substrate. Biophysical Journal. 2000;79(1):144-52. doi: 10.1016/s0006-3495(00)76279-5.
60. Sun X, Driscoll MK, Guven C, Das S, Parent CA, Fourkas JT, et al. Asymmetric nanotopography biases cytoskeletal dynamics and promotes unidirectional cell guidance. Proceedings of the National Academy of Sciences. 2015;112(41):12557-62. doi: 10.1073/pnas.1502970112.
61. Ferlay J, Soerjomataram I, Dikshit R, Eser S, Mathers C, Rebelo M, et al. Cancer incidence and mortality worldwide: Sources, methods and major patterns in GLOBOCAN 2012. International Journal of Cancer. 2015;136(5):E359-E86. doi: 10.1002/ijc.29210.
62. Hagemeister FB, Buzdar AU, Luna MA, Blumenschein GR. Causes of death in breast cancer a clinicopathologic study. Cancer. 1980;46(1):162-7. doi: 10.1002/1097-0142(19800701)46:1<162::aid-cncr2820460127>3.0.co;2-b.
63. Klein CA. Parallel progression of primary tumours and metastases. Nature Reviews Cancer. 2009;9(4):302-12. doi: 10.1038/nrc2627.
64. Aceto N, Bardia A, Miyamoto T, David, Donaldson C, Maria, Wittner S, Ben, Spencer A, Joel, et al. Circulating Tumor Cell Clusters Are Oligoclonal Precursors of

Breast Cancer Metastasis. Cell. 2014;158(5):1110-22. doi: 10.1016/j.cell.2014.07.013.
65. Cheung KJ, Padmanaban V, Silvestri V, Schipper K, Cohen JD, Fairchild AN, et al. Polyclonal breast cancer metastases arise from collective dissemination of keratin 14-expressing tumor cell clusters. Proceedings of the National Academy of Sciences. 2016;113(7):E854-E63. doi: 10.1073/pnas.1508541113.
66. Wrenn ED, Yamamoto A, Moore BM, Huang Y, Mcbirney M, Thomas AJ, et al. Regulation of Collective Metastasis by Nanolumenal Signaling. Cell. 2020;183(2):395-410.e19. doi: 10.1016/j.cell.2020.08.045.
67. López-Knowles E, O'Toole SA, Mcneil CM, Millar EKA, Qiu MR, Crea P, et al. PI3K pathway activation in breast cancer is associated with the basal-like phenotype and cancer-specific mortality. International Journal of Cancer. 2010;126(5):1121-31. doi: 10.1002/ijc.24831.
68. Wang X, Cao X, Sun R, Tang C, Tzankov A, Zhang J, et al. Clinical Significance of PTEN Deletion, Mutation, and Loss of PTEN Expression in De Novo Diffuse Large B-Cell Lymphoma. Neoplasia. 2018;20(6):574-93. doi: 10.1016/j.neo.2018.03.002.
69. Herbst RS, Schlessinger J. Small molecule combats cancer-causing KRAS protein at last. Nature. 2019;575(7782):294-5. doi: 10.1038/d41586-019-03242-8.
70. Thompson KN, Whipple RA, Yoon JR, Lipsky M, Charpentier MS, Boggs AE, et al. The combinatorial activation of the PI3K and Ras/MAPK pathways is sufficient for aggressive tumor formation, while individual pathway activation supports cell persistence. Oncotarget. 2015;6(34):35231-46. doi: 10.18632/oncotarget.6159.
71. Yankaskas CL, Thompson KN, Paul CD, Vitolo MI, Mistriotis P, Mahendra A, et al. A microfluidic assay for the quantification of the metastatic propensity of breast cancer specimens. Nature Biomedical Engineering. 2019;3(6):452-65. doi: 10.1038/s41551-019-0400-9.
72. Lee RM, Kelley DH, Nordstrom KN, Ouellette NT, Losert W. Quantifying stretching and rearrangement in epithelial sheet migration. New Journal of Physics. 2013;15(2):025036. doi: 10.1088/1367-2630/15/2/025036.
73. Weiger MC, Vedham V, Stuelten CH, Shou K, Herrera M, Sato M, et al. Real-Time Motion Analysis Reveals Cell Directionality as an Indicator of Breast Cancer Progression. PLoS ONE. 2013;8(3):e58859. doi: 10.1371/journal.pone.0058859.
74. Renkawitz J, Kopf A, Stopp J, De Vries I, Driscoll MK, Merrin J, et al. Nuclear positioning facilitates amoeboid migration along the path of least resistance. Nature. 2019;568(7753):546-50. doi: 10.1038/s41586-019-1087-5.
75. Desai RA, Gao L, Raghavan S, Liu WF, Chen CS. Cell polarity triggered by cell-cell adhesion via E-cadherin. Journal of Cell Science. 2009;122(7):905-11. doi: 10.1242/jcs.028183.
76. Ling C, Halter M, Plant A, Majurski M, Stinson J, Chalfoun J, editors. Analyzing U-Net Robustness for Single Cell Nucleus Segmentation from Phase Contrast Images. 2020 IEEE/CVF Conference on Computer Vision and Pattern Recognition Workshops (CVPRW); 2020 2020-06-01: IEEE.

77. Crocker JC, Grier DG. Methods of Digital Video Microscopy for Colloidal Studies. Journal of Colloid and Interface Science. 1996;179(1):298-310. doi: 10.1006/jcis.1996.0217.
78. Utter B, Behringer RP. Experimental Measures of Affine and Nonaffine Deformation in Granular Shear. Physical Review Letters. 2008;100(20). doi: 10.1103/physrevlett.100.208302.
79. Chen D, Semwogerere D, Sato J, Breedveld V, Weeks ER. Microscopic structural relaxation in a sheared supercooled colloidal liquid. Physical Review E. 2010;81(1). doi: 10.1103/physreve.81.011403.
80. Cavallaro U, Christofori G. Multitasking in Tumor Progression: Signaling Functions of Cell Adhesion Molecules. Annals of the New York Academy of Sciences. 2004;1014(1):58-66. doi: 10.1196/annals.1294.006.
81. Method of the Year 2024: spatial proteomics. Nature Methods. 2024;21(12):2195-6. doi: 10.1038/s41592-024-02565-3.
82. Goltsev Y, Samusik N, Kennedy-Darling J, Bhate S, Hale M, Vazquez G, et al. Deep Profiling of Mouse Splenic Architecture with CODEX Multiplexed Imaging. Cell. 2018;174(4):968-81.e15. doi: 10.1016/j.cell.2018.07.010.
83. Ramón Y Cajal S, Sesé M, Capdevila C, Aasen T, De Mattos-Arruda L, Diaz-Cano SJ, et al. Clinical implications of intratumor heterogeneity: challenges and opportunities. Journal of Molecular Medicine. 2020;98(2):161-77. doi: 10.1007/s00109-020-01874-2.
84. Lomakin A, Svedlund J, Strell C, Gataric M, Shmatko A, Rukhovich G, et al. Spatial genomics maps the structure, nature and evolution of cancer clones. Nature. 2022;611(7936):594-602. doi: 10.1038/s41586-022-05425-2.
85. Fernandez-Mateos J, Cresswell GD, Trahearn N, Webb K, Sakr C, Lampis A, et al. Tumor evolution metrics predict recurrence beyond 10 years in locally advanced prostate cancer. Nature Cancer. 2024;5(9):1334-51. doi: 10.1038/s43018-024-00787-0.
86. Provenzano PP, Eliceiri KW, Campbell JM, Inman DR, White JG, Keely PJ. Collagen reorganization at the tumor-stromal interface facilitates local invasion. BMC Medicine. 2006;4(1). doi: 10.1186/1741-7015-4-38.
87. Nam K-H, Kim P, Wood DK, Kwon S, Provenzano PP, Kim D-H. Multiscale Cues Drive Collective Cell Migration. Scientific Reports. 2016;6(1):29749. doi: 10.1038/srep29749.
88. Lichtenberg JY, Ramamurthy E, Young AD, Redman TP, Leonard CE, Das SK, et al. Leader cells mechanically respond to aligned collagen architecture to direct collective migration. PLOS ONE. 2024;19(1):e0296153. doi: 10.1371/journal.pone.0296153.
89. Weigelin B, Bakker G-J, Friedl P. Intravital third harmonic generation microscopy of collective melanoma cell invasion. IntraVital. 2012;1(1):32-43. doi: 10.4161/intv.21223.
90. Tsai TY-C, Garner RM, Megason SG. Adhesion-Based Self-Organization in Tissue Patterning. Annual Review of Cell and Developmental Biology. 2022;38(1):349-74. doi: 10.1146/annurev-cellbio-120420-100215.

91. al SPe. Testing the differential adhesion hypothesis across the epithelial−mesenchymal transition. New J Phys. 2015;17(083049). doi: DOI 10.1088/1367-2630/17/8/083049.
92. Park J, Kim D-H, Kim H-N, Wang CJ, Kwak MK, Hur E, et al. Directed migration of cancer cells guided by the graded texture of the underlying matrix. Nature Materials. 2016;15(7):792-801. doi: 10.1038/nmat4586.
93. Loesel KE, Hiraki HL, Baker BM, Parent CA. An adaptive and versatile method to quantitate and characterize collective cell migration behaviors on complex surfaces. Frontiers in Cell and Developmental Biology. 2023;11. doi: 10.3389/fcell.2023.1106653.
94. M. Pachitariu CS. Cellpose 2.0: how to train your own model. Nature Methods. 2022.
95. Cross SE, Jin Y-S, Rao J, Gimzewski JK. Nanomechanical analysis of cells from cancer patients. Nature Nanotechnology. 2007;2(12):780-3. doi: 10.1038/nnano.2007.388.
96. Xu W, Mezencev R, Kim B, Wang L, Mcdonald J, Sulchek T. Cell Stiffness Is a Biomarker of the Metastatic Potential of Ovarian Cancer Cells. PLoS ONE. 2012;7(10):e46609. doi: 10.1371/journal.pone.0046609.
97. Sahai E, Marshall CJ. RHO–GTPases and cancer. Nature Reviews Cancer. 2002;2(2):133-42. doi: 10.1038/nrc725.
98. Cain RJ, Ridley AJ. Phosphoinositide 3-kinases in cell migration. Biol Cell. 2009.
99. Berx G, Van Roy F. Involvement of Members of the Cadherin Superfamily in Cancer. Cold Spring Harbor Perspectives in Biology. 2009;1(6):a003129-a. doi: 10.1101/cshperspect.a003129.
100. Sun X, Hourwitz MJ, Baker EM, Schmidt BUS, Losert W, Fourkas JT. Replication of biocompatible, nanotopographic surfaces. Scientific Reports. 2018;8(1). doi: 10.1038/s41598-017-19008-z.
101. Vitolo MI, Weiss MB, Szmacinski M, Tahir K, Waldman T, Park BH, et al. Deletion of PTEN Promotes Tumorigenic Signaling, Resistance to Anoikis, and Altered Response to Chemotherapeutic Agents in Human Mammary Epithelial Cells. Cancer Research. 2009;69(21):8275-83. doi: 10.1158/0008-5472.can-09-1067.
102. Bishop C. Pattern Recognition and Machine Learning. Journal of Electronic Imaging. 2006;16.
103. Shlens J. A Tutorial on Principal Component Analysis. arXiv. 2014;1404.1100.
104. Wynn TA, Chawla A, Pollard JW. Macrophage biology in development, homeostasis and disease. Nature. 2013;496(7446):445-55. doi: 10.1038/nature12034.
105. Ginhoux F, Guilliams M. Tissue-Resident Macrophage Ontogeny and Homeostasis. Immunity. 2016;44(3):439-49. doi: 10.1016/j.immuni.2016.02.024.
106. Franklin RA, Liao W, Sarkar A, Kim MV, Bivona MR, Liu K, et al. The cellular and molecular origin of tumor-associated macrophages. Science. 2014;344(6186):921-5. doi: 10.1126/science.1252510.
107. Horn B, Schunck B. Determining Optical Flow. Artificial Intelligence. 1981;17:185-203.

108. Lucas B, Kanade T. An iterative image registration technique with an application to stereo vision. Proceedings of the International Joint Conference on Artificial Intelligence. 1981;674–679.
109. Institute NC. Head and neck cancers [Internet]. Accessed 2025 Jul 17. doi: https://www.cancer.gov/types/head-and-neck/head-neck-fact-sheet.
110. Leemans CR, Snijders PJF, Brakenhoff RH. The molecular landscape of head and neck cancer. Nature Reviews Cancer. 2018;18(5):269-82. doi: 10.1038/nrc.2018.11.
111. Sung H, Ferlay J, Siegel RL, Laversanne M, Soerjomataram I, Jemal A, et al. Global Cancer Statistics 2020: GLOBOCAN Estimates of Incidence and Mortality Worldwide for 36 Cancers in 185 Countries. CA: A Cancer Journal for Clinicians. 2021;71(3):209-49. doi: 10.3322/caac.21660.
112. Gillison ML, Chaturvedi AK, Anderson WF, Fakhry C. Epidemiology of Human Papillomavirus–Positive Head and Neck Squamous Cell Carcinoma. Journal of Clinical Oncology. 2015;33(29):3235-42. doi: 10.1200/jco.2015.61.6995.
113. Ferris RL, Blumenschein G, Fayette J, Guigay J, Colevas AD, Licitra L, et al. Nivolumab for Recurrent Squamous-Cell Carcinoma of the Head and Neck. New England Journal of Medicine. 2016;375(19):1856-67. doi: 10.1056/nejmoa1602252.
114. Chakraborty R, Darido C, Liu F, Maselko M, Ranganathan S. Head and Neck Cancer Immunotherapy: Molecular Biological Aspects of Preclinical and Clinical Research. Cancers. 2023;15(3):852. doi: 10.3390/cancers15030852.
115. Deenadhayalan S, Edwin E, Elumalai K. Immunotherapy for head and neck cancer: mechanisms, challenges, and future perspectives. Journal of Bio-X Research. 2024;7(Jan 2024).
116. Binnewies M, Roberts EW, Kersten K, Chan V, Fearon DF, Merad M, et al. Understanding the tumor immune microenvironment (TIME) for effective therapy. Nature Medicine. 2018;24(5):541-50. doi: 10.1038/s41591-018-0014-x.
117. Gabrilovich DI. Myeloid-Derived Suppressor Cells. Cancer Immunology Research. 2017;5(1):3-8. doi: 10.1158/2326-6066.cir-16-0297.
118. Cassetta L, Pollard JW. Targeting macrophages: therapeutic approaches in cancer. Nature Reviews Drug Discovery. 2018;17(12):887-904. doi: 10.1038/nrd.2018.169.
119. Weigert R, Sramkova M, Parente Lea. Intravital microscopy: a novel tool to study cell biology in living animals. Histochem Cell Biol. 2010;133:481–91.
120. Pittet J, Mikael, Weissleder R. Intravital Imaging. Cell. 2011;147(5):983-91. doi: 10.1016/j.cell.2011.11.004.
121. Masedunskas A, Milberg O, Porat-Shliom N, Sramkova M, Wigand T, Amornphimoltham P, et al. Intravital microscopy: a practical guide on imaging intracellular structures in live animals. BioArchitecture. 2012;2(5):143-57. doi: 10.4161/bioa.21758.
122. Ritsma L, Steller EJA, Ellenbroek SIJ, Kranenburg O, Borel Rinkes IHM, Van Rheenen J. Surgical implantation of an abdominal imaging window for intravital microscopy. Nature Protocols. 2013;8(3):583-94. doi: 10.1038/nprot.2013.026.
123. Amornphimoltham P, Thompson J, Melis N, Weigert R. Non-invasive intravital imaging of head and neck squamous cell carcinomas in live mice. Methods. 2017;128:3-11. doi: 10.1016/j.ymeth.2017.07.026.

124. Mantovani A, Marchesi F, Malesci Aea. Tumour-associated macrophages as treatment targets in oncology. Nat Rev Clin Oncol. 2017;14:399-416.
125. Qian B-Z, Pollard JW. Macrophage Diversity Enhances Tumor Progression and Metastasis. Cell. 2010;141(1):39-51. doi: 10.1016/j.cell.2010.03.014.
126. Veglia F, Sanseviero E, Gabrilovich DI. Myeloid-derived suppressor cells in the era of increasing myeloid cell diversity. Nature Reviews Immunology. 2021;21(8):485-98. doi: 10.1038/s41577-020-00490-y.
127. Maier B, Leader AM, Chen ST, Tung N, Chang C, Leberichel J, et al. A conserved dendritic-cell regulatory program limits antitumour immunity. Nature. 2020;580(7802):257-62. doi: 10.1038/s41586-020-2134-y.
128. Shaul ME, Fridlender ZG. Tumour-associated neutrophils in patients with cancer. Nat Rev Clin Oncol. 2019;16:601-20.
129. Lavin Y, Kobayashi S, Leader A, Amir E-AD, Elefant N, Bigenwald C, et al. Innate Immune Landscape in Early Lung Adenocarcinoma by Paired Single-Cell Analyses. Cell. 2017;169(4):750-65.e17. doi: 10.1016/j.cell.2017.04.014.
130. Hughes R, Qian B-Z, Rowan C, Muthana M, Keklikoglou I, Olson OC, et al. Perivascular M2 Macrophages Stimulate Tumor Relapse after Chemotherapy. Cancer Research. 2015;75(17):3479-91. doi: 10.1158/0008-5472.can-14-3587.
131. Peranzoni E, Lemoine J, Vimeux L, Feuillet V, Barrin S, Kantari-Mimoun C, et al. Macrophages impede CD8 T cells from reaching tumor cells and limit the efficacy of anti–PD-1 treatment. Proceedings of the National Academy of Sciences. 2018;115(17):E4041-E50. doi: 10.1073/pnas.1720948115.
132. Ries H, Carola, Cannarile A, Michael, Hoves S, Benz J, Wartha K, Runza V, et al. Targeting Tumor-Associated Macrophages with Anti-CSF-1R Antibody Reveals a Strategy for Cancer Therapy. Cancer Cell. 2014;25(6):846-59. doi: 10.1016/j.ccr.2014.05.016.
133. Moody AS, Dayton PA, Zamboni WC. Imaging methods to evaluate tumor microenvironment factors affecting nanoparticle drug delivery and antitumor response. Cancer Drug Resistance. 2021. doi: 10.20517/cdr.2020.94.
134. Naumenko V, Jenne C, Mahoney DJ. Intravital Microscopy for Imaging the Tumor Microenvironment in Live Mice. Methods in Molecular Biology: Springer New York; 2016. p. 217-30.
135. Porat-Shliom N, Chen Y, Tora M, Shitara A, Masedunskas A, Weigert R. In Vivo Tissue-wide Synchronization of Mitochondrial Metabolic Oscillations. Cell Reports. 2014;9(2):514-21. doi: 10.1016/j.celrep.2014.09.022.
136. Denk W, Strickler JH, Webb WW. Two-photon laser scanning fluorescence microscopy. Science. 1990;vol. 248.
137. Li L, Yang Y. Optical Flow Estimation for a Periodic Image Sequence. IEEE Transactions on Image Processing. 2010;19(1):1-10. doi: 10.1109/tip.2009.2032341.
138. Li W, Goldstein DR, Kreisel D. Intravital 2-photon imaging, leukocyte trafficking, and the beating heart. Trends in Cardiovascular Medicine. 2013;23(8):287-93. doi: 10.1016/j.tcm.2013.04.002.
139. Wee S, Jagani Z, Xiang KX, Loo A, Dorsch M, Yao Y-M, et al. PI3K Pathway Activation Mediates Resistance to MEK Inhibitors in KRAS Mutant Cancers. Cancer Research. 2009;69(10):4286-93. doi: 10.1158/0008-5472.can-08-4765.

140. Wylie AG, Korchevskiy A, Segrave AM, Duane A. Modeling mesothelioma risk factors from amphibole fiber dimensionality: mineralogical and epidemiological perspective. J Appl Toxicol. 2020;40(4):515-24. Epub 20200210. doi: 10.1002/jat.3923. PubMed PMID: 32040984.
141. Stanton MF, Layard M, Tegeris A, Miller E, May M, Morgan E, et al. Relation of particle dimension to carcinogenicity in amphibole asbestoses and other fibrous minerals. J Natl Cancer Inst. 1981;67(5):965-75. PubMed PMID: 6946253.
142. Davis JM, Addison J, McIntosh C, Miller BG, Niven K. Variations in the carcinogenicity of tremolite dust samples of differing morphology. Ann N Y Acad Sci. 1991;643:473-90. doi: 10.1111/j.1749-6632.1991.tb24497.x. PubMed PMID: 1809161.
143. Pott F. Some aspects on the dosimetry of the carcinogenic potency of asbestos and other fibrous dusts. Scopus. 1978.
144. Hodgson JT, Darnton A. The quantitative risks of mesothelioma and lung cancer in relation to asbestos exposure. The Annals of Occupational Hygiene. 2000;44(8).
145. Yang Q, Miao Y, Banerjee P, Hourwitz MJ, Hu M, Qing Q, et al. Nanotopography modulates intracellular excitable systems through cytoskeleton actuation. 2022.
146. Yang Q, Miao Y, Campanello LJ, Hourwitz MJ, Abubaker-Sharif B, Bull AL, et al. Cortical waves mediate the cellular response to electric fields. eLife. 2022;11. doi: 10.7554/elife.73198.
147. Horwitz R, Webb D. Cell migration. Current Biology. 2003;13(19):R756-R9. doi: 10.1016/j.cub.2003.09.014.
148. Pollard TD, Cooper JA. Actin, a Central Player in Cell Shape and Movement. Science. 2009;326(5957):1208-12. doi: 10.1126/science.1175862.
149. Romero S, Le Clainche C, Gautreau AM. Actin polymerization downstream of integrins: signaling pathways and mechanotransduction. Biochemical Journal. 2020;477(1):1-21. doi: 10.1042/bcj20170719.
150. Svitkina T. The Actin Cytoskeleton and Actin-Based Motility. Cold Spring Harbor Perspectives in Biology. 2018;10(1):a018267. doi: 10.1101/cshperspect.a018267.
151. Fujiwara I, Takeda S, Oda T, Honda H, Narita A, Maéda Y. Polymerization and depolymerization of actin with nucleotide states at filament ends. Biophysical Reviews. 2018;10(6):1513-9. doi: 10.1007/s12551-018-0483-7.
152. Waizumi T, Sakuta H, Hayashi M, Tsumoto K, Takiguchi K, Yoshikawa K. Polymerization/depolymerization of actin cooperates with the morphology and stability of cell-sized droplets generated in a polymer solution under a depletion effect. The Journal of Chemical Physics. 2021;155(7):075101. doi: 10.1063/5.0055460.
153. Lee RM, Campanello L, Hourwitz MJ, Alvarez P, Omidvar A, Fourkas JT, et al. Quantifying topography-guided actin dynamics across scales using optical flow. Mol Biol Cell. 2020;31(16):1753-64. Epub 20200205. doi: 10.1091/mbc.E19-11-0614. PubMed PMID: 32023172; PubMed Central PMCID: PMCPMC7521856.

154. Ketchum CM, Sun X, Suberi A, Fourkas JT, Song W, Upadhyaya A. Subcellular topography modulates actin dynamics and signaling in B-cells. Molecular Biology of the Cell. 2018;29(14):1732-42. doi: 10.1091/mbc.e17-06-0422.
155. Wheatley BA, Rey-Suarez I, Hourwitz MJ, Kerr S, Shroff H, Fourkas JT, et al. Nanotopography modulates cytoskeletal organization and dynamics during T cell activation. Molecular Biology of the Cell. 2022;33(10). doi: 10.1091/mbc.e21-12-0601.
156. Bianchi C, Bianchi T. Susceptibility and resistance in the genesis of asbestos-related mesothelioma. Indian J Occup Environ Med. 2008;12(2):57-60. doi: 10.4103/0019-5278.43261. PubMed PMID: 20040979; PubMed Central PMCID: PMCPMC2796755.
157. Wylie A. Asbestos and Fibrous Erionite. 2017. p. 11-41.
158. Korchevskiy AA, Wylie AG. Dimensional determinants for the carcinogenic potency of elongate amphibole particles. Inhal Toxicol. 2021;33(6-8):244-59. Epub 20211006. doi: 10.1080/08958378.2021.1971340. PubMed PMID: 34612763.
159. Korchevskiy AA, Wylie AG. Dimensional characteristics of the major types of amphibole mineral particles and the implications for carcinogenic risk assessment. Inhal Toxicol. 2022;34(1-2):24-38. Epub 20220110. doi: 10.1080/08958378.2021.2024304. PubMed PMID: 35001771.